Computer Methods in Applied Mechanics and Engineering 448 (2026) 118349

Contents lists available at ScienceDirect

Comput. Methods Appl. Mech. Engrg.

journal homepage: www.elsevier.com/locate/cma

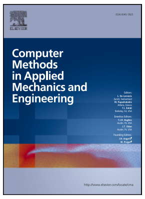

Stretch-based hyperelastic electromechanical constitutive metamodels via gradient enhanced Gaussian predictors using hierarchical structure discovery

Nathan Ellmer [a,*], Rogelio Ortigosa [b,*], Jesús Martínez-Frutos [b,*], Roman Poya [c], Johann Sienz [a], Antonio J. Gil [a,*]

[a] *Zienkiewicz Institute for Modelling, Data and AI, Faculty of Science and Engineering, Swansea University, Bay Campus, SA1 8EN, United Kingdom*
[b] *Technical University of Cartagena, Campus Muralla del Mar, Cartagena, Murcia, 30202, Spain*
[c] *Meshing & Abstraction, Simulation and Test Solutions, Siemens Digital Industries Software, Cambridge, United Kingdom*

ARTICLE INFO

Keywords:
Gradient Kriging
Constitutive modelling
Principal stretches
Electromechanics
Anisotropy

ABSTRACT

This paper introduces a new approach to developing electromechanical constitutive metamodels via the use of Gradient Enhanced Gaussian Predictors (Kriging). The formulation uses principal stretches for the isotropic mechanics, invariants for the electrostatics and coupling terms, and accounts for anisotropy through the relevant inclusion of anisotropic invariants associated with a respective symmetry integrity basis. Three novelties are presented in this paper. The first is the use of orthogonal projections to identify the most appropriate set of inputs - related to material anisotropy - for use in the metamodel. By projecting the stress and electric field data into several derivative bases - defined for each anisotropic class - and then reconstructing the quantities, the errors in reconstruction can be assessed thus inferring the most appropriate class of anisotropy. Furthermore, the procedure forms a pre-processing stage and is particularly useful when an underlying model is completely unknown as seen when modelling Relative Volume Elements. The second novelty arises from the use of a hybrid formulation, namely the principal stretches for isotropic mechanics and the electromechanical anisotropic invariants. This is beneficial during the projection procedure in reducing the cases where the projection matrix becomes singular but requires careful development of the correlation function to maintain physical symmetry conditions. Thirdly, the electromechanical metamodels are calibrated upon the concentric styled data before being integrated within a Finite Element framework and tested upon a range of challenging simulations including bending actuators with induced torsion, frilling due to bending with selected electrode placement, as well as buckling plates tested with three rank-one laminate materials with increasing levels of anisotropy due to physical contrasts. The successful calibration and implementation of the metamodels can be witnessed amongst the wide range of presented numerical examples.

1. Introduction

Soft robotics is a rapidly advancing field which aims to exploit the properties of soft active materials to improve several aspects such as biomimetic actuation [1], or an improved human-machine interface via self-sensing capabilities [2]. To realise this capability,

---

[*] Corresponding authors.
E-mail addresses: n.s.ellmer@swansea.ac.uk (N. Ellmer), rogelio.ortigosa@upct.es (R. Ortigosa), jesus.martinez@upct.es (J. Martínez-Frutos), a.j.gil@swansea.ac.uk (A.J. Gil).

https://doi.org/10.1016/j.cma.2025.118349
Received 29 May 2025; Received in revised form 29 July 2025; Accepted 25 August 2025

there is significant interest in soft smart materials which are electrically stimulated referred to as electroactive polymers (EAPs), and more specifically their subclass - dielectric elastomers (DEs) - which consist of a soft dielectric layer sandwiched between two flexible conductive electrode layers [3]. Maximising the potential of these material systems has propelled research into complex composites to harness the advantageous properties from multiple materials whilst limiting the compromising impacts [4–6].

These composites tend to be fabricated using two distinct methods leading to either laminates or inclusions. Capturing the highly nonlinear behaviour of these materials requires the development of intense analytical constitutive models which produce the macroscopic homogenised response of the material. This is achieved through employing rank-n homogenisation theory which yields the effective material response by delving and computing the response of each material constituent within the composite [7]. Since the lamination or inclusions exist at the micro-scale this introduces a multi-scale problem which necessitates the use of a Newton-Raphson type procedure to solve the micro-fluctuations [8,9]. The intricacy involved in such analytical models clearly demonstrates that as these composites continue to develop in complexity, the traditional model fitting techniques - homogenisation via fitting experimental data directly to pre-existing frameworks - will be unable to maintain the adequate level of accuracy.

In search of model fitting techniques which are not restricted by rigid frameworks, an increasing number of researchers are turning to leverage the capabilities of Machine Learning (ML). The most commonly applied ML technique is that of Neural Networks (NNs) which come in a variety of forms. In the context of constitutive modelling, Constitutive Artificial Neural Networks (CANNs) were introduced with the aim of assisting the satisfaction of physical constraints such as objectivity and material symmetry. Kuhl et al. [10] applied CANNs to develop models for rubber materials validated via uniaxial, biaxial and shear experimental data. Moreover, Linka et al. [11] compared the performance of CANNs to standard Artificial Neural Networks (ANNs) demonstrating that for isotropic constitutive models, CANNs required less data for calibration. Outside of ML, development of constitutive models often considers the notion of convexity to ensure stability and robustness [12–15]. The same can be achieved within ML as comprehensively studied by Klein et al. showcasing the ability to train convex NNs. These NNs use inputs based on invariants or the deformation gradient tensor, its cofactor and its determinant - quantities which are understood to develop polyconvex constitutive models [16]. Klein's work has additionally been extended to incorporate electromechanically coupled systems [17,18]. In addition, Ortigosa et al. [19] has developed Physics-Augmented Neural Networks capable of calibrating thermo-electro-mechanically coupled systems. The generalised approach ensures flexibility in calibrating on a variety of thermodynamic potentials given by different combinations of the physical inputs as obtained via the appropriate Legendre transforms.

Furthermore, Laura De Lorenzis et al. [20] has developed the EUCLID scheme – unsupervised automated discovery of material laws (EUCLID). Using a developed catalogue of constitutive material frameworks, the scheme is capable of handling a vast range of data and fitting it to the appropriate frameworks. The model fitting aspect has been investigated in the context of NN's [21] and a Bayesian implementation [22] with the aim of learning elastic and viscoelastic models with varying amounts of anisotropy. This scheme has also more recently been extended to handle data from biological tissue [23] which is hyperelastic in nature as well as a framework for pressure-sensitive plasticity models [24].

Gaussian Process Regression (GPR) is an alternative ML approach which has advantageous characteristics due to its probabilistic roots. The technique exploits properties of Gaussian distributions to formulate a joint distribution of known and predictive data sites over the variables of interest. The resultant predictive distribution is then sampled yielding a solution accompanied with an uncertainty - a useful quantity to indicate the accuracy of the prediction. Providing the uncertainty is essential for error estimation and capitalising on infill strategies [25–27]. The heart of GPR lies with the correlation function which comes in a variety of forms. For this work the authors have selected the Radial Basis Function (RBF) to correlate the observed data in the parametric space revealing a weighting used to indicate the importance of specific variables. Kriging is a variation of GPR developed by Matheron upon theory from mining engineer, Krige, in the field of geostatistics in the 1960's [28]. Moreover, gradient data can be used to enhance Kriging's calibration - a process referred to as Gradient Enhanced Kriging [29]. The advantages of the enhancement have been investigated by the authors in previous work, and include requiring fewer data points to achieve the same level of performance as employing the Ordinary Kriging counterpart [30].

Re-aligning to the context of constitutive modelling, Frankel et al. [31] details two different approaches for the use of GPR. The first models the stress-strain relationship directly, which requires additional measures to ensure satisfaction of physical constraints such as data augmentation. The second is an energy-invariant relationship which naturally satisfies constraints such as thermodynamics and objectivity – invariance to rigid body rotations. As illuded to, GPR can be enhanced by utilising gradient data during calibration. Aggarwal et al. [32] demonstrated the significance of gradient data, thus requiring only limited functional data to achieve an accurate constitutive model. This is particularly beneficial when considering experimental data, since the strain energy is not available on demand, whereas stress information is experimentally obtainable. Exploiting Kriging's probabilistic roots, Rocha [33] has used an adaptive infill strategy based upon Kriging's uncertainty to improve the accuracy of model results when simulating the elastoplastic response of fibre reinforced composites. Moreover, previous work by the authors showcased the exceptional capability of Gradient Enhanced Kriging to develop a variety of stretch-based hyperelastic mechanical constitutive metamodels. Examples were presented with metamodels from a range of anisotropic classes with high accuracy calibrated on as few as 16 datapoints [34].

This manuscript focuses on two main aspects of work, the first of which is showcasing a procedure for identifying classes of anisotropy from stress and electric field data directly. In current ML techniques, to obtain information regarding the material anisotropy group Fuhg et al. [35] and Kalina et al. [36] have introduced parameters into the NN which weights the contributions from anisotropic invariants thus tailoring the model towards the required anisotropic formulation. In this work, a procedure which exploits linear algebra - specifically orthogonal projections - is proposed to ascertain the anisotropic information prior to initiating the metamodel calibration. As a result, this anisotropic identification forms a pre-processing stage on the data independent of the

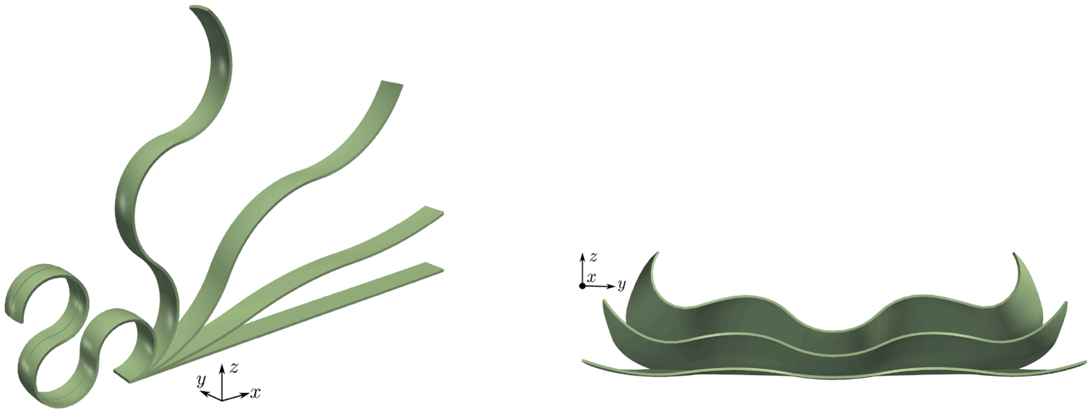

(a) Isotropic bending

(b) Isotropic frilling

Fig. 1. Displays the progression of two DE inspired actuator devices both configured to apply an inhomogeneous electric field. Note that both devices are split in half in the y-direction such that the left side is modelled using the ground truth constitutive model, and the right side using the Kriging constitutive metamodel: (a) uses an isotropic Mooney-Rivlin model for the mechanical contribution; (b) uses an isotropic Ogden model for the mechanical contribution, whilst in both an Ideal Dielectric is applied for the electro contribution.

metamodel calibration process thus enabling one to use this procedure to learn about the material data regardless of intentions to use ML.

The second aspect involves developing a variety of coupled electromechanical constitutive metamodels which can be integrated into the in-house 3D FEM framework to produce a range of complex deformations (see examples in Fig. 1). The formulations developed in the following work are based on a mixed approach incorporating principal stretches for the isotropic mechanics and invariants for the anisotropy and electromechanically coupled variables. Doing so enables advantageous properties to be utilised such as the ability to project all purely mechanical and isotropic stresses without the need for perturbations which would be required with the invariant based counterparts (as carried out in [30]). As a result, accurate projections can be taken in scenarios such as when principal stretches take the same value - a necessity for employing Gradient Enhanced Kriging [34].

The layout of this paper is as follows: Section 2 initially introduces the reader to the core concepts of nonlinear continuum electromechanics with specific emphasis on the formulation of constitutive models in finite strain hyperelasticity. Section 3 then transitions to a description of the procedure for identifying the anisotropic group from data directly via a hierarchical approach. Next, Section 4 provides an overview of the Kriging approach which is employed to develop the constitutive metamodels. The numerical examples are then split into two parts, the first in Section 5 provides information regarding the data generation for Kriging and then the results for the wide range of constitutive models that have been calibrated upon. Subsequently, Section 6 presents the equally varied set of the FE numerical examples ranging from isotropic bending to anisotropic buckling. Concluding remarks then bring this work to a close in Section 7.

Notation: Throughout the paper, $\boldsymbol{A} : \boldsymbol{B} = A_{IJ} B_{IJ}$, $\forall \boldsymbol{A}, \boldsymbol{B} \in \mathbb{R}^{3\times3}$, and the use of repeated indices implies summation. The tensor product is denoted by $\otimes$ and the second order identity tensor by $\boldsymbol{I}$. The tensor cross product operation $\times$ between two artibrary second order tensor $\boldsymbol{A}$ and $\boldsymbol{B}$ entails $[\boldsymbol{A} \times \boldsymbol{B}]_{IJ} = \mathcal{E}_{IPQ}\mathcal{E}_{JRS}A_{PR}B_{QS}$ [37]. Furthermore, $\boldsymbol{\mathcal{E}}$ represents the third-order alternating tensor. The full and special orthogonal groups in $\mathbb{R}^3$ are represented as $\mathrm{O}(3) = \{\boldsymbol{A} \in \mathbb{R}^{3\times3} |\, \boldsymbol{A}^T\boldsymbol{A} = \boldsymbol{I}\}$ and $\mathrm{SO}(3) = \{\boldsymbol{A} \in \mathbb{R}^{3\times3} |\, \boldsymbol{A}^T\boldsymbol{A} = \boldsymbol{I},\ \det\boldsymbol{A} = 1\}$, respectively and the set of invertible second order tensors with positive determinant is denoted by $\mathrm{GL}^+(3) = \{\boldsymbol{A} \in \mathbb{R}^{3\times3} |\, \det\boldsymbol{A} > 0\}$.

2. Finite strain electromechanics

2.1. Kinematics

A solid electroactive polymer (EAP) body undergoing a deformation can be described via two configurations, as illustrated in Fig. 2. The first is the material (undeformed) configuration given by $\mathcal{B}_0 \subset \mathbb{R}^3$ and the second, a spatial (deformed) configuration given by $\mathcal{B} \subset \mathbb{R}^3$. To transform between the configurations, a mapping exists for each material particle $\boldsymbol{\phi} : \mathcal{B}_0 \to \mathbb{R}^3$ thus translating from material coordinates $\boldsymbol{X} \in \mathcal{B}_0$ to spatial coordinates $\boldsymbol{x} \in \mathcal{B}$ through the relationship $\boldsymbol{x} = \boldsymbol{\phi}(\boldsymbol{X})$. Moreover, this relationship is employed to define the material deformation gradient $\boldsymbol{F} \in \mathrm{GL}^+(3)$ also referred to as the fibre map, which leads to definitions for the volume map J, and the area map $\boldsymbol{H}$ as

$$\boldsymbol{F} = \partial_{\boldsymbol{X}}\boldsymbol{\phi}, \qquad J = \det\boldsymbol{F} = \frac{1}{6}\boldsymbol{F} : (\boldsymbol{F} \times \boldsymbol{F}), \qquad \boldsymbol{H} = \mathrm{Cof}\boldsymbol{F} = J\boldsymbol{F}^{-T} = \frac{1}{2}\boldsymbol{F} \times \boldsymbol{F}. \tag{1}$$

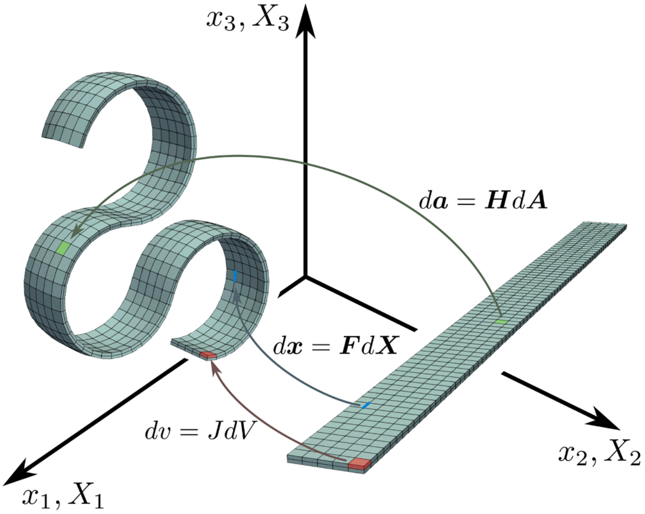

Fig. 2. Demonstrates the mappings of material coordinates to spatial coordinates (fibre map $\boldsymbol{F}$ in blue, area map $\boldsymbol{H}$ in green, and volume map J in red).(For interpretation of the references to color in this figure legend, the reader is referred to the web version of this article.)

2.2. Governing equations in finite electromechanics

The response of an EAP body is governed by the following coupled boundary value problem

$$\underbrace{\begin{aligned} \boldsymbol{F} &= \partial_{\boldsymbol{X}} \boldsymbol{\phi}, && \text{in } \mathcal{B}_0 \\ \text{DIV}\boldsymbol{P} &= -\boldsymbol{f}_0, && \text{in } \mathcal{B}_0 \\ \boldsymbol{\phi} &= \boldsymbol{\phi}^*, && \text{on } \partial_{\boldsymbol{\phi}} \mathcal{B}_0 \\ \boldsymbol{P}\boldsymbol{N} &= \boldsymbol{t}_0, && \text{on } \partial_{\boldsymbol{t}} \mathcal{B}_0 \end{aligned}}_{\text{Conservation of linear momentum and kinematics}} \qquad \underbrace{\begin{aligned} \boldsymbol{E}_0 &= -\partial_{\boldsymbol{X}} \varphi, && \text{in } \mathcal{B}_0 \\ \text{DIV}\boldsymbol{D}_0 &= \rho_0, && \text{in } \mathcal{B}_0 \\ \varphi &= \varphi^*, && \text{on } \partial_{\varphi} \mathcal{B}_0 \\ \boldsymbol{D}_0 \cdot \boldsymbol{N} &= -\omega_0, && \text{on } \partial_{\omega} \mathcal{B}_0 \end{aligned}}_{\text{Gauss' and Faraday's Law}} \tag{2}$$

where the equations on the left represent the purely mechanical response whilst those on the right constitute the electrostatic response. In (2), the DIV(■) operator denotes the divergence with respect to the material coordinates $\boldsymbol{X} \in \mathcal{B}_0$ whilst $\boldsymbol{N}$ represents the material outward unit vector. On the left hand side of (2), the mechanical quantities $\boldsymbol{f}_0$ and $\boldsymbol{t}_0$ are the body and traction forces acting on the undeformed body $\mathcal{B}_0$ and surface area $\partial\mathcal{B}_0$, respectively. The electrostatic quantities on the right hand side of (2) include the electric potential scalar field denoted φ as well as the electric charge acting on the undeformed body $\mathcal{B}_0$ and surface area $\partial\mathcal{B}_0$ denoted by ρ_0 and ω_0, respectively. The boundary of the undeformed body, $\partial\mathcal{B}_0$, is described by two non-overlapping regions for imposing Dirichlet $\partial_{\boldsymbol{\phi}}\mathcal{B}_0$ and Neumann $\partial_{\boldsymbol{t}}\mathcal{B}_0$ boundary conditions such that

$$\underbrace{\begin{aligned} \partial\mathcal{B}_0 &= \partial_{\boldsymbol{\phi}}\mathcal{B}_0 \cup \partial_{\boldsymbol{t}}\mathcal{B}_0, \\ \emptyset &= \partial_{\boldsymbol{\phi}}\mathcal{B}_0 \cap \partial_{\boldsymbol{t}}\mathcal{B}_0, \end{aligned}}_{\text{Mechanical boundary regions}} \qquad \underbrace{\begin{aligned} \partial\mathcal{B}_0 &= \partial_{\varphi}\mathcal{B}_0 \cup \partial_{\omega}\mathcal{B}_0, \\ \emptyset &= \partial_{\varphi}\mathcal{B}_0 \cap \partial_{\omega}\mathcal{B}_0. \end{aligned}}_{\text{Electrostatic boundary regions}} \tag{3}$$

Finally, note the two pairs of work conjugates in (2), the deformation gradient tensor $\boldsymbol{F}$ and first Piola-Kirchhoff stress tensor $\boldsymbol{P}$, as well as the electric field vector $\boldsymbol{E}_0$ and material electric displacement vector $\boldsymbol{D}_0$. Through the application of an appropriate constitutive model, definitions for $\boldsymbol{P}$ and $\boldsymbol{D}_0$ will be obtained consisting of contributions from mechanics and electrostatics thus demonstrating the coupling of physics.

2.3. Internal energy density requirements in electromechanics

To close the system of governing equations outlined in (2) a constitutive relationship needs to be defined, often in the form of an internal energy density. Moreover, this relationship can be seen to couple the physics as the internal energy density e is dependent on the deformation gradient tensor $\boldsymbol{F}$ and the material electric displacement $\boldsymbol{D}_0$ as

$$e : GL^+(3) \times \mathbb{R}^3 \to \mathbb{R}, \qquad \left(\boldsymbol{F}, \boldsymbol{D}_0\right) \to e\left(\boldsymbol{F}, \boldsymbol{D}_0\right). \tag{4}$$

Taking partial derivatives of $e\left(\boldsymbol{F}, \boldsymbol{D}_0\right)$ with respect to both $\boldsymbol{F}$ and $\boldsymbol{D}_0$ yields the first Piola-Kirchhoff stress tensor $\boldsymbol{P}$ and the material electric field $\boldsymbol{E}_0$ respectively, as described below

$$\boldsymbol{P} = \partial_{\boldsymbol{F}} e\left(\boldsymbol{F}, \boldsymbol{D}_0\right), \qquad \boldsymbol{E}_0 = \partial_{\boldsymbol{D}_0} e\left(\boldsymbol{F}, \boldsymbol{D}_0\right). \tag{5}$$

Additionally, taking the second partial derivatives yields three more quantities: the fourth order elasticity tensor $\boldsymbol{C}$, the third order coupled piezoelectric tensor $\boldsymbol{Q}$, and the second order dielectric tensor $\boldsymbol{\theta}$ as

$$\boldsymbol{C} = \partial^2_{\boldsymbol{F}\boldsymbol{F}} e\big(\boldsymbol{F}, \boldsymbol{D}_0\big), \qquad \boldsymbol{Q} = \partial^2_{\boldsymbol{D}_0\boldsymbol{F}} e\big(\boldsymbol{F}, \boldsymbol{D}_0\big), \qquad \boldsymbol{\theta} = \partial^2_{\boldsymbol{D}_0\boldsymbol{D}_0} e\big(\boldsymbol{F}, \boldsymbol{D}_0\big). \tag{6}$$

The internal energy density $e\big(\boldsymbol{F}, \boldsymbol{D}_0\big)$ is required to conform to physical principles including that of objectivity, also referred to as material frame indifference, namely

$$e\big(\boldsymbol{Q}\boldsymbol{F}, \boldsymbol{D}_0\big) = e\big(\boldsymbol{F}, \boldsymbol{D}_0\big), \qquad \forall \boldsymbol{F} \in GL^+(3), \quad \boldsymbol{Q} \in SO(3), \quad \boldsymbol{D}_0 \in \mathbb{R}^3. \tag{7}$$

Furthermore, critical when considering anisotropy is that $e\big(\boldsymbol{F}, \boldsymbol{D}_0\big)$ must adhere to the specific material symmetry group $\mathcal{G}$ through

$$e\big(\boldsymbol{F}\boldsymbol{Q}, \boldsymbol{D}_0\big) = e\big(\boldsymbol{F}, \boldsymbol{D}_0\big), \qquad \forall \boldsymbol{F} \in GL^+(3), \quad \boldsymbol{Q} \in \mathcal{G} \subseteq O(3), \quad \boldsymbol{D}_0 \in \mathbb{R}^3. \tag{8}$$

It is also important to state that the internal energy $e\big(\boldsymbol{F}, \boldsymbol{D}_0\big)$, first Piola-Kirchhoff stress tensor $\boldsymbol{P}$, and material electric field vector $\boldsymbol{E}_0$ must all vanish in the absence of deformation and electric displacement. This can be mathematically described by

$$e\big(\boldsymbol{F}, \boldsymbol{D}_0\big)|_{\boldsymbol{F}=\boldsymbol{I}, \boldsymbol{D}_0=\boldsymbol{0}} = 0, \qquad \boldsymbol{P}\big(\boldsymbol{F}, \boldsymbol{D}_0\big)|_{\boldsymbol{F}=\boldsymbol{I}, \boldsymbol{D}_0=\boldsymbol{0}} = \boldsymbol{0}, \qquad \boldsymbol{E}_0\big(\boldsymbol{F}, \boldsymbol{D}_0\big)|_{\boldsymbol{F}=\boldsymbol{I}, \boldsymbol{D}_0=\boldsymbol{0}} = \boldsymbol{0}. \tag{9}$$

The conditions presented in (7)–(9) are the essential physical principles. Additionally, it is customary to apply the notions of polyconvexity to the internal energy density thereby ensuring the propagation of real wave speeds, guarantees the existence of minimisers, thus providing numerical stability [38]. Whilst outside the scope of this work, Poya et al. has outlined the steps to satisfy polyconvexity via a principal stretch approach which involves monitoring the Hessian matrix - formed of the second derivatives given in (6) - and setting any subsequent subzero eigenvalues to zero [39,40]. Upon assessment of the numerical examples presented in this work, all conducted examples converged without unphysical instabilities thus rendering the implementation of such steps unnecessary.

Remark 1. Note that there are several forms of free energies available such as the internal energy, $e\big(\boldsymbol{F}, \boldsymbol{D}_0\big)$, Helmholtz's energy, $\Psi\big(\boldsymbol{F}, \boldsymbol{E}_0\big)$, enthalpy $H\big(\boldsymbol{P}, \boldsymbol{D}_0\big)$. The definitions can be transitioned between using the appropriate Legendre transforms - for more information the reader is referred to [19,41].

2.4. Principal stretch-based electromechanics

To embed objectivity into the internal energy density $e\big(\boldsymbol{F}, \boldsymbol{D}_0\big)$ and simultaneously satisfy material symmetry conditions it is common to formulate in terms of invariants of the right Cauchy-Green strain tensor [38,42] or in terms of principal stretches [39,43]

$$e\big(\boldsymbol{F}, \boldsymbol{D}_0\big) = U(\mathbf{I}), \tag{10}$$

where $\mathbf{I}$[1] denotes an input set that could consist of invariants, or principal stretches, or a mixture of both as will become evident. Furthermore, recall (5) where the first Piola-Kirchhoff stress tensor $\boldsymbol{P}$ and material electric field $\boldsymbol{E}_0$ were defined as partial derivatives of $e\big(\boldsymbol{F}, \boldsymbol{D}_0\big)$ with respect to the deformation gradient tensor $\boldsymbol{F}$ and the electric displacement vector $\boldsymbol{D}_0$. Application of the chain rule and convenient decomposition into isotropic and anisotropic contributions enables them to be re-expressed as

$$\begin{aligned} \boldsymbol{P} &= \underbrace{\sum_{i=1}^{m_{iso}} \Big(\partial_{\mathrm{I}_i} U\Big) \partial_{\boldsymbol{F}} \mathrm{I}_i}_{\text{Isotropic contribution}} + \underbrace{\sum_{i=m_{iso}+1}^{m} \Big(\partial_{\mathrm{I}_i} U\Big) \partial_{\boldsymbol{F}} \mathrm{I}_i}_{\text{Anisotropic contribution}}, \\ \boldsymbol{E}_0 &= \underbrace{\sum_{i=1}^{m_{iso}} \Big(\partial_{\mathrm{I}_i} U\Big) \partial_{\boldsymbol{D}_0} \mathrm{I}_i}_{\text{Isotropic contribution}} + \underbrace{\sum_{i=m_{iso}+1}^{m} \Big(\partial_{\mathrm{I}_i} U\Big) \partial_{\boldsymbol{D}_0} \mathrm{I}_i}_{\text{Anisotropic contribution}}, \end{aligned} \tag{11}$$

where m_{iso} and m signify the number of isotropic inputs and the total number of inputs including the additional anisotropic invariants, respectively. Similarly, a generic definition for the second derivatives can also be expressed as

$$\begin{aligned} \boldsymbol{C} &= \sum_{i=1}^{m} \Big(\partial_{\mathrm{I}_i} U\Big) \partial^2_{\boldsymbol{F}\boldsymbol{F}} \mathrm{I}_i + \sum_{i,j=1}^{m} \Big(\partial^2_{\mathrm{I}_i \mathrm{I}_j} U\Big) \partial_{\boldsymbol{F}} \mathrm{I}_i \otimes \partial_{\boldsymbol{F}} \mathrm{I}_j, \\ \boldsymbol{Q} &= \sum_{i=1}^{m} \Big(\partial_{\mathrm{I}_i} U\Big) \partial^2_{\boldsymbol{D}_0\boldsymbol{F}} \mathrm{I}_i + \sum_{i,j=1}^{m} \Big(\partial^2_{\mathrm{I}_i \mathrm{I}_j} U\Big) \partial_{\boldsymbol{D}_0} \mathrm{I}_i \otimes \partial_{\boldsymbol{F}} \mathrm{I}_j, \\ \boldsymbol{\theta} &= \sum_{i=1}^{m} \Big(\partial_{\mathrm{I}_i} U\Big) \partial^2_{\boldsymbol{D}_0\boldsymbol{D}_0} \mathrm{I}_i + \sum_{i,j=1}^{m} \Big(\partial^2_{\mathrm{I}_i \mathrm{I}_j} U\Big) \partial_{\boldsymbol{D}_0} \mathrm{I}_i \otimes \partial_{\boldsymbol{D}_0} \mathrm{I}_j. \end{aligned} \tag{12}$$

Note that (12) has not been separated into isotropic and anisotropic contributions for readability, but the deconstruction would follow that of (11). Thus far, (11) and (12) have provided a generic formulation, and to provide the reader with specifics, the remainder of this section has been broken into the contributions for a variety of anisotropic classes.

---

[1] Notice that here $\mathbf{I}$ and $\boldsymbol{I}$ represent different quantities, namely the former is for the potential set of inputs consisting of either invariants or principal stretches and the latter is the second order identity tensor.

2.4.1. Isotropic contribution

Starting with isotropy, principal stretches will be used to describe the mechanics whilst invariants will be used for the electrostatics and coupling. Firstly then, the principal stretches can be obtained through the right polar decomposition of the deformation gradient tensor $\boldsymbol{F}$ as

$$\boldsymbol{F} = \boldsymbol{R}\boldsymbol{U}, \tag{13}$$

where $\boldsymbol{R} \in SO(3)$ is the rotation tensor and $\boldsymbol{U}$ is the symmetric positive definite stretch tensor. To retrieve these quantities from $\boldsymbol{F}$, singular value decomposition (SVD) can be employed

$$\boldsymbol{F} = \hat{\boldsymbol{U}}\boldsymbol{\Lambda}\hat{\boldsymbol{V}}^T, \qquad \boldsymbol{R} = \hat{\boldsymbol{U}}\hat{\boldsymbol{V}}^T, \qquad \boldsymbol{U} = \hat{\boldsymbol{V}}\boldsymbol{\Lambda}\hat{\boldsymbol{V}}^T. \tag{14}$$

Note that in (14), $\hat{\boldsymbol{U}}$ and $\hat{\boldsymbol{V}}^T$ are the left and right singular-matrices, respectively, and the tensor $\boldsymbol{\Lambda}$ encodes the singular-values of $\boldsymbol{F}$, i.e. the principal stretches $\lambda_1 \geq \lambda_2 \geq \lambda_3$ such that $\lambda_i = \Lambda_{ii}$. For the electromechanical invariants, the following definitions are utilised

$$I_4 = \boldsymbol{D}_0 \cdot \boldsymbol{D}_0, \qquad I_5 = \boldsymbol{F}\boldsymbol{D}_0 \cdot \boldsymbol{F}\boldsymbol{D}_0. \tag{15}$$

With the principal stretches and invariants for isotropy established, the set $\mathbf{I}$ used in (10) can be set to $\mathbf{I} = \left\{\lambda_1, \lambda_2, \lambda_3, I_4, I_5\right\}$. In the interest of being concise the definitions for the relevant partial derivatives required in (11) and (12) can be found in Appendix A.1.

2.4.2. Anisotropic contribution (transverse isotropy)

Introducing anisotropy will require additional invariants which are used to incorporate favoured anisotropic directions. For transverse isotropy, the anisotropic invariants are given by

$$I_6 = \boldsymbol{F}\boldsymbol{N} \cdot \boldsymbol{F}\boldsymbol{N}, \qquad I_7 = \boldsymbol{H}\boldsymbol{N} \cdot \boldsymbol{H}\boldsymbol{N}, \qquad I_8 = \left(\boldsymbol{D}_0 \cdot \boldsymbol{N}\right)^2, \tag{16}$$

where $\boldsymbol{N}$ is the preferred anisotropic direction, perpendicular to the plane of isotropy in the material. With these invariants it can be seen that in (10), $m = 8$ and $\mathbf{I} = \left\{\lambda_1, \lambda_2, \lambda_3, I_4, I_5, I_6, I_7, I_8\right\}$. The relevant partial derivatives for (11) and (12) can be found in Appendix A.2.

2.4.3. Anisotropic contribution (orthotropy)

Another common form of anisotropy is that of orthotropy which is characterised by three unitary and orthogonal preferential directions $\left\{\boldsymbol{N}_1, \boldsymbol{N}_2, \boldsymbol{N}_3\right\}$. Several invariants can be used to capture orthotropy and they are given by

$$\begin{aligned} &I_6 = \boldsymbol{F}\boldsymbol{N}_1 \cdot \boldsymbol{F}\boldsymbol{N}_1, \qquad I_7 = \boldsymbol{H}\boldsymbol{N}_1 \cdot \boldsymbol{H}\boldsymbol{N}_1, \qquad I_8 = \boldsymbol{F}\boldsymbol{N}_2 \cdot \boldsymbol{F}\boldsymbol{N}_2, \\ &I_9 = \left(\boldsymbol{D}_0 \cdot \boldsymbol{N}_1\right)^2, \qquad I_{10} = \left(\boldsymbol{D}_0 \cdot \boldsymbol{N}_2\right)^2. \end{aligned} \tag{17}$$

With these invariants it can be seen that in (10), $m = 10$ and $\mathbf{I} = \left\{\lambda_1, \lambda_2, \lambda_3, I_4, I_5, I_6, I_7, I_8, I_9, I_{10}\right\}$. The corresponding derivatives for (11) and (12) can be found in Appendix A.3.

Remark 2. The invariants which have been presented throughout Section 2.4 have been carefully chosen by the authors to ensure the sufficient characterisation of the constitutive models presented in the numerical examples. It must be noted however that this list is not exhaustive and other invariants (up to 13 in the most comprehensive case for orthotropy - see Table 16 of [44]) can be included and might be required for alternative constitutive models.

2.5. Application to composite materials

To model increasingly complex material microstructures it is critical to utilise composite related theory such as rank-n homogenisation theory [7,45]. This process enables a material's microstructure to be captured in homogenised macroscopic quantities which will then be used during the Finite Element Method (FEM). However, this process is not trivial and involves a nonlinear problem wrapped within the standard FEM process leading to what is commonly referred to as FEM2 [8,9]. Fig. 3 presents a side-by-side comparison of the electromechanical homogenisation process for the two most common composite types: rank-one laminates [4–6,9,46] and matrix-inclusions described through representative volume elements [17,18].

3. Hierarchical structure discovery

Material anisotropy is categorised into material symmetry groups which are characterised by a set of invariants - some of which can be found in Section 2.4. A primary aim of introducing GPR into constitutive model development is to reduce the analysis required to identify and fit the most appropriate pre-existing framework, however, this is only achievable if the most appropriate material symmetry group can be identified from the data directly without prior knowledge of a material sample. When the symmetry group is isotropy, then the preparation and use of ML is immediate due to the metamodel inputs being invariants which are only functions of the data itself - see Section 2.4.1. This is not the case when the material is anisotropic since the structural tensors and vectors associated with the symmetry group also need to be identified. As an example, consider transverse isotropy where the material symmetry group requires the structural rank-one tensor $\boldsymbol{N} \otimes \boldsymbol{N}$ - for full details see Section 2.4.2. Once transverse isotropy is found to be the most appropriate symmetry group, the best vector $\boldsymbol{N}$ also needs to be identified. Moreover, it must be noted that these material parameters need to be identified a priori in order to prepare the data for metamodel calibration, since the inputs are formed of invariants which are functions of these structural vectors or tensors.

Rank-one Laminate

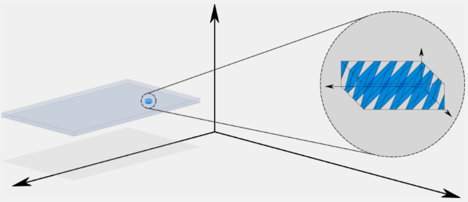

The macropscopic deformation gradient $\boldsymbol{F}$ and electric displacement $\boldsymbol{D}_0$ comprises of the microscale constituents as

$$\boldsymbol{F} = c^a \boldsymbol{F}^a + c^b \boldsymbol{F}^b, \quad \boldsymbol{D}_0 = c^a \boldsymbol{D}_0^a + c^b \boldsymbol{D}_0^b, \tag{18}$$

where c_a and c_b are the constituent volume fractions. Definitions for microscale components of $\boldsymbol{F}$ and $\boldsymbol{D}_0$ can be obtained in accordance with $[\![\boldsymbol{F}]\!] \times \boldsymbol{N} = \boldsymbol{0}$ as well as $[\![\boldsymbol{D}_0]\!] \cdot \boldsymbol{N} = 0$ by

$$\begin{aligned}
\boldsymbol{F}^a(\boldsymbol{F}, \boldsymbol{\alpha}) &= \boldsymbol{F} + c^b \boldsymbol{\alpha} \otimes \boldsymbol{N}, \\
\boldsymbol{F}^b(\boldsymbol{F}, \boldsymbol{\alpha}) &= \boldsymbol{F} - c^a \boldsymbol{\alpha} \otimes \boldsymbol{N}, \\
\boldsymbol{D}_0^a(\boldsymbol{D}_0, \boldsymbol{\beta}) &= \boldsymbol{D}_0 + c^b \mathcal{T}_{\boldsymbol{N}} \boldsymbol{\beta}, \\
\boldsymbol{D}_0^b(\boldsymbol{D}_0, \boldsymbol{\beta}) &= \boldsymbol{D}_0 - c^a \mathcal{T}_{\boldsymbol{N}} \boldsymbol{\beta},
\end{aligned} \tag{19}$$

where $\boldsymbol{\alpha}$ and $\boldsymbol{\beta}$ denote the mechanical and electrostatic microscale fluctuations respectively, $\boldsymbol{N}$ the direction of lamination perpendicular to the plane of isotropy, and $\mathcal{T}_{\boldsymbol{N}}$ a projection operator - for details see Appendix B. $\{\boldsymbol{\alpha}, \boldsymbol{\beta}\}$ can be obtained through minimisation of the energy

$$e(\boldsymbol{F}, \boldsymbol{D}_0) = \arg\min_{\boldsymbol{\alpha}, \boldsymbol{\beta}} \{\hat{e}(\boldsymbol{F}, \boldsymbol{D}_0, \boldsymbol{\alpha}, \boldsymbol{\beta})\}, \tag{20}$$

where the effective energy, $\hat{e}(\boldsymbol{F}, \boldsymbol{D}_0, \boldsymbol{\alpha}, \boldsymbol{\beta})$ is comprised of the energy for each constituent through

$$\begin{aligned}
\hat{e} = {} & c^a e^a (\boldsymbol{F}^a(\boldsymbol{F}, \boldsymbol{\alpha}), (\boldsymbol{D}_0^a, \boldsymbol{\beta})) \\
& + c^b e^b \left(\boldsymbol{F}^b(\boldsymbol{F}, \boldsymbol{\alpha}), \left(\boldsymbol{D}_0^b, \boldsymbol{\beta}\right)\right),
\end{aligned} \tag{21}$$

To obtain $\{\boldsymbol{\alpha}, \boldsymbol{\beta}\}$, the stationary conditions of $\hat{e}$ needs to be solved.

$$\begin{aligned}
D\hat{e}[\delta\boldsymbol{\alpha}] &= c^a c^b \left(\boldsymbol{P}^a - \boldsymbol{P}^b\right) : (\delta\boldsymbol{\alpha} \otimes \boldsymbol{N}) = 0, \\
D\hat{e}[\delta\boldsymbol{\beta}] &= c^a c^b \left(\boldsymbol{E}_0^a - \boldsymbol{E}_0^b\right) \cdot (\mathcal{T}_{\boldsymbol{N}} \delta\boldsymbol{\beta}) = 0,
\end{aligned} \tag{22}$$

in turn yielding the macroscopic first Piola-Kirchhoff stress $\boldsymbol{P}$ and material electric field $\boldsymbol{E}_0$ as

$$\begin{aligned}
\boldsymbol{P} &= c^a \boldsymbol{P}^a + c^b \boldsymbol{P}^b, \\
\boldsymbol{E}_0 &= c^a \boldsymbol{E}_0^a + c^b \boldsymbol{E}_0^b,
\end{aligned} \tag{23}$$

rendering the microscale components of $\boldsymbol{P}$ and $\boldsymbol{E}_0$ as

$$\begin{aligned}
\boldsymbol{P}^a &= \frac{\partial e^a (\boldsymbol{F}^a(\boldsymbol{F}, \boldsymbol{\alpha}), (\boldsymbol{D}_0^a, \boldsymbol{\beta}))}{\partial \boldsymbol{F}^a}, \\
\boldsymbol{E}_0^a &= \frac{\partial e^a (\boldsymbol{F}^a(\boldsymbol{F}, \boldsymbol{\alpha}), (\boldsymbol{D}_0^a, \boldsymbol{\beta}))}{\partial \boldsymbol{D}_0^a},
\end{aligned} \tag{24}$$

For more in-depth information the reader is referred to [4–6, 9, 46].

Representative Volume Element

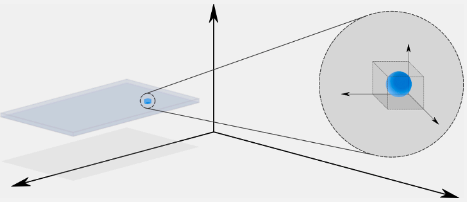

The macroscopic deformation gradient $\boldsymbol{F}$ and electric field $\boldsymbol{E}_0$ are related to their microscale counterparts as

$$\begin{aligned}
\boldsymbol{F} &= \frac{1}{V^\mu} \int_{\mathcal{B}_{0\mu}} \boldsymbol{F}^\mu (\boldsymbol{X}^\mu) \, dV^\mu, \\
\boldsymbol{E}_0 &= \frac{1}{V^\mu} \int_{\mathcal{B}_{0\mu}} \boldsymbol{E}_0^\mu (\boldsymbol{X}^\mu) \, dV^\mu,
\end{aligned} \tag{25}$$

where $\boldsymbol{F}^\mu$ and $\boldsymbol{E}_0^\mu$ represent fields across the elements volume, V^μ. Applying periodic boundary conditions, $[\![\boldsymbol{\alpha}]\!] = \boldsymbol{0}$ and $[\![\beta]\!] = 0$, enables $\boldsymbol{x}^\mu$ and φ^μ to be expressed by

$$\begin{aligned}
\boldsymbol{F}^\mu &= \frac{\partial \boldsymbol{x}^\mu}{\partial \boldsymbol{X}^\mu} \text{ where } \boldsymbol{x}^\mu = \boldsymbol{\alpha} + \boldsymbol{F}\boldsymbol{X}^\mu, \\
\boldsymbol{E}_0^\mu &= -\frac{\partial \varphi^\mu}{\partial \boldsymbol{X}^\mu} \text{ where } \varphi^\mu = \beta - \boldsymbol{E}_0 \cdot \boldsymbol{X}^\mu,
\end{aligned} \tag{26}$$

thus $\boldsymbol{F}^\mu$ and $\boldsymbol{E}_0^\mu$ can be expressed as

$$\boldsymbol{F}^\mu = \boldsymbol{\nabla}_0 \boldsymbol{\alpha} + \boldsymbol{F}, \quad \boldsymbol{E}_0^\mu = \boldsymbol{\nabla}_0 \beta - \boldsymbol{E}_0. \tag{27}$$

$\{\boldsymbol{\alpha}, \beta\}$, can be found via an energy minimisation

$$\Psi(\boldsymbol{F}, \boldsymbol{E}_0) = \inf_{\boldsymbol{\alpha} \in \mathbb{V}_{\boldsymbol{x}}} \sup_{\beta \in \mathbb{V}_\varphi} \left\{ \hat{\Psi}(\boldsymbol{F}, \boldsymbol{E}_0, \boldsymbol{\alpha}, \beta) \right\}, \tag{28}$$

where the effective energy $\hat{\Psi}(\boldsymbol{F}, \boldsymbol{E}_0, \boldsymbol{\alpha}, \beta)$ is evaluated according to

$$\hat{\Psi} = \frac{1}{V^\mu} \int_{\mathcal{B}_{0\mu}} \Psi^\mu (\boldsymbol{F}^\mu(\boldsymbol{F}, \boldsymbol{\alpha}), \boldsymbol{E}_0^\mu(\boldsymbol{E}_0, \beta)) \, dV^\mu. \tag{29}$$

The stationary conditions of $\Pi(\boldsymbol{\alpha}, \beta) = \hat{\Psi} V^\mu$ yielding $\{\boldsymbol{\alpha}, \beta\}$ are

$$\begin{aligned}
D\Pi(\boldsymbol{\alpha})[\delta\boldsymbol{\alpha}] &= \int_{\mathcal{B}_{0\mu}} \boldsymbol{P}^\mu : \frac{\partial \boldsymbol{\alpha}}{\partial \boldsymbol{X}^\mu} dV^\mu &&= 0, \\
D\Pi(\beta)[\delta\beta] &= -\int_{\mathcal{B}_{0\mu}} \boldsymbol{D}_0^\mu \cdot \frac{\partial \beta}{\partial \boldsymbol{X}^\mu} dV^\mu &&= 0,
\end{aligned} \tag{30}$$

which yields the macroscopic first Piola-Kirchhoff stress $\boldsymbol{P}$ and electric displacement $\boldsymbol{D}_0$ as

$$\begin{aligned}
\boldsymbol{P} &= \frac{1}{V^\mu} \int_{\mathcal{B}_{0\mu}} \boldsymbol{P}^\mu dV^\mu, \\
\boldsymbol{D}_0 &= \frac{1}{V^\mu} \int_{\mathcal{B}_{0\mu}} \boldsymbol{D}_0^\mu dV^\mu,
\end{aligned} \tag{31}$$

where the microscale components of $\boldsymbol{P}$ and $\boldsymbol{D}_0$ are

$$\begin{aligned}
\boldsymbol{P}^\mu &= \frac{\partial \Psi^\mu (\boldsymbol{F}^\mu(\boldsymbol{F}, \boldsymbol{\alpha}), \boldsymbol{E}_0^\mu(\boldsymbol{E}_0, \beta))}{\partial \boldsymbol{F}^\mu}, \\
\boldsymbol{D}_0^\mu &= -\frac{\partial \Psi^\mu (\boldsymbol{F}^\mu(\boldsymbol{F}, \boldsymbol{\alpha}), \boldsymbol{E}_0^\mu(\boldsymbol{E}_0, \beta))}{\partial \boldsymbol{E}_0^\mu}.
\end{aligned} \tag{32}$$

A Legendre transform can be used to yield $\boldsymbol{E}_0^\mu$ from $\boldsymbol{F}^\mu$ and $\boldsymbol{D}_0^\mu$. For more details see [17, 18].

Fig. 3. Presents a side by side comparison of the approach to evaluate the homogenised quantities for rank-one laminates and representative volume elements, with the aim of demonstrating their similarities.

3.1. Hierarchical structure discovery procedure

In this work, the authors propose a systematic and algebraically grounded procedure to identify the most appropriate material symmetry group and corresponding optimal structural tensors of the underlying data set. The approach relies on the tools of linear algebra, particularly orthogonal projections. Each candidate symmetry group is associated with a set of invariants, as comprehensively detailed by Zheng in [44]. The method centres on projecting constitutive quantities - specifically, the first Piola–Kirchhoff stress $\boldsymbol{P}$ and the material electric field $\boldsymbol{E}_0$ - onto subspaces defined by these symmetry groups. To facilitate this operation, $\boldsymbol{P}$ and $\boldsymbol{E}_0$ are vectorised and concatenated into a single 12-dimensional vector $\boldsymbol{a} \in \mathbb{R}^{12}$

$$\boldsymbol{a} = \begin{bmatrix} \widehat{\boldsymbol{P}} \\ \boldsymbol{E}_0 \end{bmatrix}, \tag{33}$$

where $\widehat{\blacksquare}$ denotes the vectorised form of the tensor. Each vector $\boldsymbol{a}$ corresponds to a data point associated with an (unknown) underlying material symmetry group $\mathcal{G}$. In principle, the data may originate either from numerical simulations or experimental observations and can be assumed to be derived from an unknown internal energy density function U, which depends on a set of invariants $\{I_1, \dots, I_m\} \in \mathcal{G}$

$$\boldsymbol{a} = \sum_{i=1}^{m} a_i \boldsymbol{v}_i, \qquad a_i = \partial_{I_i} U, \tag{34}$$

with

$$\boldsymbol{v}_i = \begin{bmatrix} \widehat{\partial_{\boldsymbol{F}} I_i} \\ \partial_{\boldsymbol{D}_0} I_i \end{bmatrix}, \qquad i = \{1, \dots, m\}. \tag{35}$$

Remark 3. Among the selected invariants $\{I_1^*, \dots, I_{m^*}^*\} \in \mathcal{G}^*$, some are isotropic, whilst others are anisotropic with respect to the material symmetry group $\mathcal{G}^*$. The anisotropic invariants depend on a set of structural vectors or tensors that characterise the material anisotropy. These structural quantities are, in general, unknown a priori. The procedure for identifying the optimal set of such vectors or tensors that best approximate $\boldsymbol{a}^*$ to $\boldsymbol{a}$ is detailed in Section 3.2. As a result, for the remainder of this Section, the structural vectors and tensors required to evaluate the selected invariants are assumed to be known.

This formulation enables a direct analogy with linear algebra: the vector $\boldsymbol{a}$ resides in a subspace $\mathcal{V} \subset \mathbb{R}^{12}$ determined by the material symmetry group $\mathcal{G}$. The vectors $\boldsymbol{v}_i$ span this subspace and form a generating set $B_{\mathcal{V}}$ which, if linearly independent, constitute a basis. The scalars a_i represent the components of $\boldsymbol{a}$ with respect to this basis. The goal is to determine the material symmetry group $\mathcal{G}^*$ whose associated subspace $\mathcal{V}^*$ is closest to the one inferred from the data. For this purpose, a new set of invariants $\{I_1^*, \dots, I_{m^*}^*\} \in \mathcal{G}^*$ are selected and used to construct a surrogate internal energy function U^* using Kriging interpolation. Differentiation with respect to these invariants yields an approximate field

$$\boldsymbol{a}^* = \sum_{i=1}^{m^*} a_i^* \boldsymbol{v}_i^*, \qquad a_i^* = \partial_{I_i^*} U^*, \tag{36}$$

where

$$\boldsymbol{v}_i^* = \begin{bmatrix} \widehat{\partial_{\boldsymbol{F}} I_i^*} \\ \partial_{\boldsymbol{D}_0} I_i^* \end{bmatrix}, \qquad i = \{1, \dots, m^*\}. \tag{37}$$

The selected invariants - more specifically their derivatives denoted by $\boldsymbol{v}_i^*$ - define a basis $B_{\mathcal{V}^*}$ for the subspace $\mathcal{V}^* \subset \mathbb{R}^{12}$, allowing the field $\boldsymbol{a}^*$ to be expressed explicitly in terms of basis vectors and corresponding coefficients. To identify the projection of the true response vector $\boldsymbol{a}$ onto the candidate subspace $\mathcal{V}^*$, the orthogonal projection of $\boldsymbol{a}$ onto $\mathcal{V}^*$ spanned by the known basis $\{\boldsymbol{v}_1^*, \dots, \boldsymbol{v}_{m^*}^*\}$ is computed. The coefficients a_i^* can be determined by solving the following linear system

$$\begin{bmatrix} \boldsymbol{a} \cdot \boldsymbol{v}_1^* \\ \vdots \\ \boldsymbol{a} \cdot \boldsymbol{v}_{m^*}^* \end{bmatrix} = \boldsymbol{M} \begin{bmatrix} a_1^* \\ \vdots \\ a_{m^*}^* \end{bmatrix}, \qquad \text{with} \quad [\boldsymbol{M}]_{ij} = \boldsymbol{v}_i^* \cdot \boldsymbol{v}_j^*, \quad i, j = \{1, \dots, m^*\}. \tag{38}$$

This projection framework allows for a rigorous and quantitative comparison between symmetry groups by measuring the proximity between the actual field $\boldsymbol{a}$ and its best approximation $\boldsymbol{a}^*$ within the subspace $\mathcal{V}^*$. A diagramatic view of this process can be seen in Fig. 4.

Following this construction, a *distance* can be evaluated between the reconstructed vector $\boldsymbol{a}^*$ and the true vector $\boldsymbol{a}$ via the standard L2 error

$$distance = \frac{\|\boldsymbol{a}^* - \boldsymbol{a}\|}{\|\boldsymbol{a}\|}, \tag{39}$$

which enables the assessment of the suitability of the chosen vector subspace $\mathcal{V}^*$ and thus the chosen material symmetry group. If the chosen $\mathcal{V}^*$ is capable of fully describing the true vector $\boldsymbol{a}$ then the *distance* will of course be zero. However, when handling more complex composite materials such as RVEs, the most suitable material symmetry group remains disputed and as a result, this procedure will become a minimisation problem such that the process iterates through symmetry groups in order of complexity and

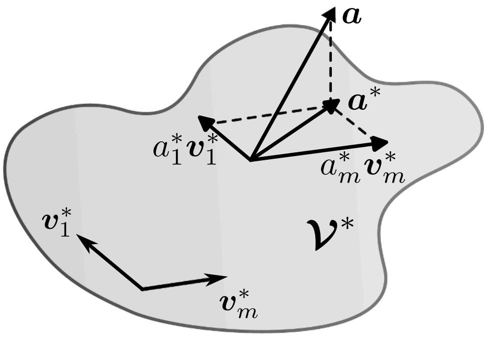

Fig. 4. Displays a reference diagram used to describe the projection process during hierarchical structure discovery.

attempts to identify the most suitable group by minimising for the $distance$ in (39). The procedure for a single selected material symmetry group can be found summarised more clearly in Algorithm 1.

Additionally, one also needs to consider the structural tensors or vectors which are used to characterise specific anisotropic material symmetry groups. For each symmetry group assessed, Algorithm 1 needs to be wrapped in an optimisation problem defined through

$$\{\boldsymbol{\mathcal{M}}^*\} = \arg\min_{\boldsymbol{\mathcal{M}}} distance\big(\boldsymbol{a}, \boldsymbol{a}^*\big), \tag{40}$$

where $\boldsymbol{\mathcal{M}}$ denotes the relevant set of structural tensors or vectors for the selected material symmetry group. To summarise then, for the hierarchical procedure of identifying the most appropriate symmetry group and structural tensors and vectors, one needs to iterate over the optimisation problem in (40) for each symmetry group which is embedded with the process outlined in Algorithm 1 where the $distance$ is the objective function.

Algorithm 1 Pseudo-code for the procedure of material symmetry group discovery.

```
Evaluate the set of appropriate derivatives to form $\boldsymbol{\mathcal{V}}^*$ as in (37) - see Section 2.4
Conduct the projections of $\boldsymbol{a}$ in $\boldsymbol{\mathcal{V}}^*$ - see (38)
Construct $\boldsymbol{a}^*$ from the projected components - see (36)
Evaluate the $distance$ between the true vector $\boldsymbol{a}$ and constructed vector $\boldsymbol{a}^*$ - see (39)
```

3.2. Hierarchal structure discovery examples

To showcase the outlined procedure in action, a range of examples have been selected and provided across this subsection. The first example is used to identify the appropriate material symmetry group and anisotropic direction for data produced via the transversely isotropic material model provided in Appendix E.3. Moreover, this includes a small study assessing the performance of the method when the “severity” of anisotropy (controlled by material parameter μ_3) is varied. Challenging examples utilising RVEs then follow in Sections 3.2.2 and 3.2.3, which truly represent the need for such a method where the underlying material symmetry group and corresponding anisotropic directions are simply unknown. In these cases the dataset is generated by running FEM simulations on the RVE configurations for a selection of deformation gradient tensors $\boldsymbol{F}$ and electric field vectors $\boldsymbol{E}_0$ (the use of a Helmholtz type energy instead of an internal energy will become clear later).

3.2.1. Transverse isotropy

The first example then takes a transversely isotropic model with material parameters corresponding to those in Appendix E.3, but using a random direction $\boldsymbol{N} \in \mathbb{R}^3$ to be revealed shortly. A dataset was generated using the ground truth model consisting of only 27 data points each of which with a corresponding $\boldsymbol{P}$ and $\boldsymbol{E}_0$. The first material class to be assessed via the procedure is that of isotropy which is defined by the five inputs as covered in Section 2.4.1. When the outlined procedure was conducted for isotropy, the $distance$ was 4.97×10^{-1}, which clearly indicates isotropy does not consist of a sufficient basis to describe this material. As a result, the next most complex class, transverse isotropy, is assessed which is characterised using the anisotropic direction $\boldsymbol{N}$. Since $\boldsymbol{N}$ is a parameter, this must be obtained via an optimisation problem, i.e. finding the vector $\boldsymbol{N}$ which yields the smallest error in (39), whilst testing for this material group. Fig. 5(a) showcases the evolution of the boxmin objective function denoted f - which is equal to the $distance$ in (39) - and Fig. 5(b) demonstrates the evolution and convergence of the anisotropic direction to $[0.44263, -0.8847, 0.1474]^T$. Within ten boxmin iterations the $distance$ was 3.22×10^{-6}, substantially lower and thus indicating that this anisotropic class is sufficient.

When verifying the results, the selected material was a transversely isotropic material with direction $\boldsymbol{N} = [0.4423, -0.8847, 0.1474]^T$. The L2 relative error between the actual and optimised directions came to $0.006\,\%$. This discovered class of anisotropy was then used to calibrate a metamodel for which the results can be seen later in Section 6.3.

A further investigation has been conducted to understand the impacts of the “severity” of anisotropy, namely the magnitude of material parameter μ_3, on the ability for the projection procedure to accurately ascertain the material symmetry group and direction

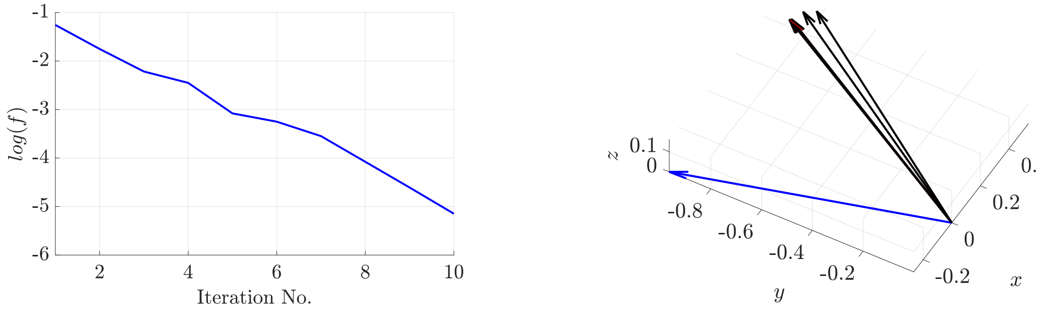

(a) Displays the log of the objective function error f.

(b) Presents the trialled directions from the boxmin optimisation.

Fig. 5. Showcases the evolution of the anisotropic directions as the boxmin algorithm optimises two angles characterising the anisotropic direction to minimise the objective function. In (a) f is the evaluation of the objective function which is equal to the $distance$ in (39). In (b) the blue arrow indicates the initial guess and the black arrows show the boxmin converging to the correct result presented by a red arrow.(For interpretation of the references to color in this figure legend, the reader is referred to the web version of this article.)

Table 1
Presents the results of a study using 27 data points to investigate the impact of changing the μ_3 material parameter on the ability to discover the direction of anisotropy $\boldsymbol{N}$. Information about the transversely isotropic model can be found in Appendix E.3.

μ_3:	*distance* (see (39))		Relative error in predicted $\boldsymbol{N}$:
	Isotropy:	Transverse Isotropy:	
0.0	5.24×10^{-16}	–	–
1.0	2.90×10^{-1}	2.53×10^{-6}	0.0062 %
3.0	4.48×10^{-1}	2.91×10^{-6}	0.0052 %
5.0	4.83×10^{-1}	3.13×10^{-6}	0.0052 %
7.5	4.97×10^{-1}	3.22×10^{-6}	0.0052 %

$\boldsymbol{N}$. In the transversely isotropic model - see Appendix E.3 - the μ_3 parameter scales the contribution from the transversely isotropic invariants. Note, that for the investigation the same 27 data points were utilised with the same direction $\boldsymbol{N} = [0.4423, -0.8847, 0.1474]^T$ but the stresses and electric fields are updated to incorporate the adjusted μ_3 parameter. The results for a variety of selected values for μ_3 can be found in Table 1.

Starting with a μ_3 of zero, the procedure correctly identifies that the data should correspond to a fully isotropic model. Interestingly, the lower values for μ_3 shown in Table 1 which would indicate a "weak anisotropy" can also be well captured. Larger values additionally achieve an excellent level of accuracy as presented previously.

3.2.2. RVE - spherical inclusion

The previous example showcased a transversely isotropic material which is relatively simple to identify and verify. This next example involves a representative volume element (RVE) consisting of a soft matrix with a stiffer (five times stiffer), spherical inclusion - see Fig. 6(a) for a digram and see Appendix E.5 RVE(a) for information on the material parameters. The challenge associated with this example is that the underlying analytical model to fully characterise this material is unknown and the data in which the metamodel will be calibrated on is the result of finite element simulations utilising a multi-scale homogenisation procedure as demonstrated in Section 2.5. During the procedure, it was seen that not all ten of the inputs presented in Section 2.4.3 were required as their derivatives were not necessarily all linearly independent - which presented itself through numerical analysis of the projection matrix which was observed to become rank deficient.

When passed to the hierarchical discovery procedure with a dataset of 27 data points, the isotropy and transverse isotropy classes were tested yielding $distances$ of 7.79×10^{-2} and 3.74×10^{-4} respectively. In order to more accurately capture the RVE, the orthotropic anisotropy class is generally considered which yielded a $distance$ of 4.70×10^{-6}. To provide an initial seed to the boxmin algorithm for the anisotropic directions $\boldsymbol{N}_1$ and $\boldsymbol{N}_2$, SVD was performed on $\boldsymbol{P}$ from a single data point, and the two left vectors associated with the largest singular values taken. This ensures the initial seed vectors are firstly orthogonal and also in a region aligned with the inclusion which intuitively would most influence the anisotropic directions. Note that for transverse isotropy it was possible to assess the correct convergence of material parameter $\boldsymbol{N}$, given that the underlying analytical model was known. The same is not possible with an RVE which highlights the challenges of working with composites.

A cubic RVE with a central spherical inclusion (as demonstrated by RVE(a) in Fig. 6(a)) might give the impression that it should yield an isotropic response due to its symmetry. However, this is not always the case as can be observed in Section 3.2.2. Kalina et al. [36] showcased an isotropic response for two inclusion geometries, specifically with a radius of $0.1L$ and $0.5L$, the latter of which means the diameter spans the full width L of the RVE. In either of these, the matrix or inclusion are likely to dominate thus rendering

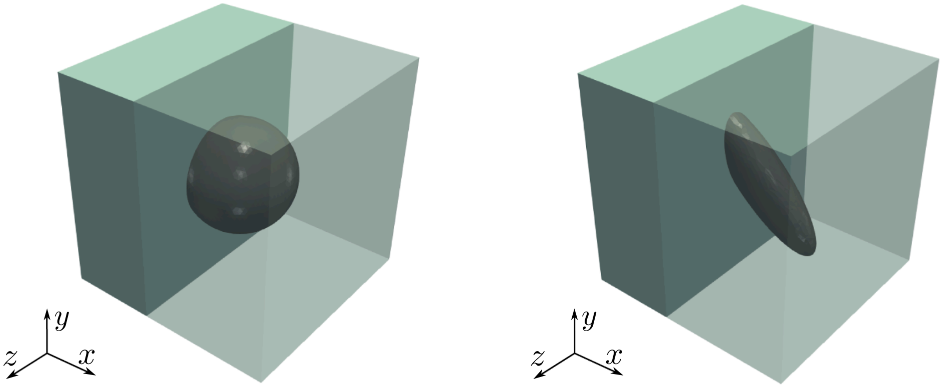

(a) Displays an RVE with a spherical inclusion

(b) Presents an RVE with an ellipsoidal inclusion

Fig. 6. Showcases two $1 \times 1 \times 1$ RVE configurations with a soft matrix and a stiffer embedded particle inclusion.

isotropy, especially since any slice of the RVE should consist of a similar ratio between materials. Furthermore, a mechanical contrast of 1.5 is used for some of the examples which is not significantly large. Thusly, if the correct combination of geometry and property contrast is selected an isotropic response can be observed. Of course this may not be the case, as in Section 3.2.2, where orthotropy is observed due to the use of an inclusion of radius $0.25L$ and mechanical contrast 5. This anisotropy has additionally been observed by Kalina et al. (see Section 5.2.1 of [47]) where a cube shaped RVE with a central spherical inclusion produced a response best captured via cubic symmetry group $\mathcal{G}_7$.

3.2.3. RVE - ellipsoidal inclusion

The final example in this section demonstrates an RVE with an ellipsoidal inclusion - see Fig. 6(b) for a digram and see Appendix E.5 RVE(b) for information on the material parameters - thus increasing the level of expected anisotropy. Once again, when passed through the hierarchical structural discovery procedure with the isotropic and transversely isotropic classes, high $distances$ were obtained of 7.65×10^{-2} and 2.74×10^{-3} respectively. The next stage involved fitting the orthotropic class which achieved a reduced $distance$ of 9.27×10^{-5} deducing it was the most suitable anisotropic class. An example ML metamodel has been calibrated using the results of this procedure and is presented in Section 5.5.

4. Gaussian process prediction

The constitutive relationships outlined in Sections 2.3 and 2.4 are crucial for Finite Element modelling. Alternatives to the conventional method of obtaining these models include generating a metamodel utilising data driven ML approaches, and the authors are particularly advocating for the use of GPR. Gradient Enhanced Kriging, a particular form of GPR capable of employing gradient data to enhance the prediction accuracy, will be the approach considered in this work. The following section will briefly outline the process for developing a Gradient Enhanced Kriging metamodel, however the interested reader is directed to Section 3 of [34] for an in-depth procedure.

4.1. Metamodel formulation

Section 2 outlined the need for a constitutive model which takes inputs relating to the deformation gradient tensor $\boldsymbol{F}$ and the material electric displacement vector $\boldsymbol{D}_0$ and produce an output used to obtain the first Piola-Kirchhoff stress tensor $\boldsymbol{P}$ and material electric field vector $\boldsymbol{E}_0$. As in Section 2.4.1, the input $\mathbf{I}$ will be comprised of principal stretches in conjunction with electromechanical invariants. In the cases using anisotropy, this set of input variables can be extended as shown in Sections 2.4.2 and 2.4.3. The metamodel outputs will be the scalar strain energy density U, and the partial derivatives $\partial_{\mathbf{I}_i} U$, which can be used to reconstruct $\boldsymbol{P}$ and $\boldsymbol{E}_0$, as seen in (11).

The notation used to handle a dataset formed of N data points and N_{inp} input variables (otherwise known as input features) is outlined as follows: superscripts will be used to denote the ith data point (i.e. $\blacksquare^{(i)}$ for $i = [1, \dots, N]$) whilst subscripts will refer to the input feature, namely the kth input variable (i.e. $\blacksquare_k$). Moreover, input and output data is set into two categories, observed data and prediction sites. These unobserved quantities relating to the prediction site are distinguished by having a superscript bullet (i.e. $\blacksquare^{\bullet}$). The foundations of a GPR metamodel are formed of a simple two-part additive expression given by

$$U(\mathbf{I}) = \beta(\mathbf{I}) + Z(\mathbf{I}) \qquad \text{where} \qquad Z(\mathbf{I}) \sim \mathcal{N}\big(\mathbf{0}, \sigma^2(\mathbf{I})\boldsymbol{R}(\mathbf{I})\big). \tag{41}$$

The two components introduced in (41) consist of a mean type term (model parameter $\beta(\mathbf{I})$) alongside a noise term which is characterised using a zero mean normal distribution $Z(\mathbf{I})$ with covariance denoted by $\sigma^2(\mathbf{I})\boldsymbol{R}(\mathbf{I})$. The covariance introduces the second material parameter $\sigma^2(\mathbf{I})$ as well as the fundamental correlation matrix $\boldsymbol{R}(\mathbf{I})$ which is seen to be a function of the observed data (no superscript bullet). To define $\boldsymbol{R}(\mathbf{I})$, a correlation function needs to be selected, of which there are several types available (see [25]). In this work the authors use the Radial Basis Function (RBF) defined as

$$\mathcal{R}\left(\mathbf{I}^{(i)}, \mathbf{I}^{(j)}, \boldsymbol{\theta}\right) = \exp\left[\sum_{k=1}^{N_{inp}} -\theta_k \left(\mathrm{I}_k^{(i)} - \mathrm{I}_k^{(j)}\right)^2\right], \qquad i, j \in [1, \dots, N]. \tag{42}$$

The RBF in (42) introduces a set of hyperparameters $\boldsymbol{\theta}$ which scale the spatial correlation between the ith and jth data points, effectively adjusting the sensitivity. Note that calibrating a model using principal stretches $\boldsymbol{\lambda}$ requires an adjusted correlation function as described by the authors in [34], where the correlation function takes inputs of the isotropic invariants $\{I_1, I_2, I_3\}$ as a function of principal stretches, namely $\mathrm{I}_k^{(i)} = I_k\left(\boldsymbol{\lambda}^{(i)}\right)$ for $k \in [1, 2, 3]$. This is critical to ensure that material symmetry conditions are satisfied. Thus far it may be unclear as to how this method is Gradient Enhanced, however this enhancement comes in the construction of $\boldsymbol{R}$ as introduced by Ollar et al. [29]. The correlation matrix can be broken into the following blocks

$$\boldsymbol{R}(\mathbf{I}, \boldsymbol{\theta}) = \begin{bmatrix} \boldsymbol{Q}_{11} & \boldsymbol{Q}_{12} \\ \boldsymbol{Q}_{12}^T & \boldsymbol{Q}_{22} \end{bmatrix}, \tag{43}$$

where

$$\left[\boldsymbol{Q}_{11}\right]^{(i)(j)} = \mathcal{R}\left(\mathbf{I}^{(i)}, \mathbf{I}^{(j)}, \boldsymbol{\theta}\right), \qquad i, j \in [1, \dots, N], \tag{44a}$$

$$\left[\boldsymbol{Q}_{12}\right]_k^{(i)(j)} = \partial_{\mathrm{I}_k^{(j)}} \mathcal{R}, \qquad i, j \in [1, \dots, N], \quad k \in \left[1, \dots, N_{inp}\right], \tag{44b}$$

$$\left[\boldsymbol{Q}_{22}\right]_{kl}^{(i)(j)} = \partial^2_{\mathrm{I}_l^{(i)} \mathrm{I}_k^{(j)}} \mathcal{R}, \qquad i, j \in [1, \dots, N], \quad k, l \in \left[1, \dots, N_{inp}\right]. \tag{44c}$$

Notice that $\boldsymbol{Q}_{12}$ and $\boldsymbol{Q}_{22}$ in (44b) and (44c) are third and fourth order matrices respectively. For computational convenience these are reshaped to fit into the correlation matrix format shown in (43) such that $\boldsymbol{Q}_{12} \in \mathbb{R}^{N \times (N \cdot N_{inp})}$ and $\boldsymbol{Q}_{22} \in \mathbb{R}^{(N \cdot N_{inp}) \times (N \cdot N_{inp})}$, thus $\boldsymbol{R} \in \mathbb{R}^{N(1+N_{inp}) \times N(1+N_{inp})}$. For full definitions of the partial derivatives used in (44b) and (44c) see Appendix C. With the key definitions in place, recall (41). Given that the noise term $Z(\mathbf{I})$ is characterised by a Gaussian distribution, it is also appropriate to express the output $U(\mathbf{I})$ in terms of a Gaussian as

$$\boldsymbol{U}(\mathbf{I}) \sim \mathcal{N}\left(\mathbf{1}\beta, \sigma^2 \boldsymbol{R}(\mathbf{I}, \boldsymbol{\theta})\right). \tag{45}$$

Note that in (45), $U(\mathbf{I}) \in \mathbb{R}$ has become $\boldsymbol{U}(\mathbf{I}) \in \mathbb{R}^{N(1+N_{inp})}$ to account for N observed data points, and that the functional dependency of $\mathbf{I}$ on the material parameters $\{\beta, \sigma^2\}$ has been dropped for notational convenience. For consistency, this additionally introduces the need for $\mathbf{1} \in \mathbb{R}^{N(1+N_{inp})}$, a vector of ones establishing a mean vector within the Gaussian definition. Defining the metamodel in terms of a Gaussian distribution demonstrates GPR's probabilistic roots and furthermore, (45) has a multi-variate probability density function (referred to as the likelihood). The Maximum Likelihood Estimation (MLE) technique [25], uses the opposite log-likelihood function to obtain the model parameters through the minimisation

$$\{\beta^*, \sigma^{2^*}\} = \arg\min_{\beta, \sigma^2} \mathscr{L}\left(\boldsymbol{U} | \beta, \sigma^2, \boldsymbol{\theta}\right), \tag{46}$$

where the opposite log-likelihood function can be expressed by

$$\mathscr{L}\left(\boldsymbol{U} | \beta, \sigma^2, \boldsymbol{\theta}\right) = \frac{A}{2} \log(2\pi) + \frac{A}{2} \log\left(\sigma^2\right) + \frac{1}{2} \log(|\boldsymbol{R}(\boldsymbol{\theta})|) + \frac{1}{2\sigma^2} (\boldsymbol{U} - \mathbf{1}\beta)^T \boldsymbol{R}^{-1}(\boldsymbol{\theta}) (\boldsymbol{U} - \mathbf{1}\beta), \tag{47}$$

where $A = N\left(1 + N_{inp}\right)$ and the functional dependence of the inputs $\mathbf{I}$ on the correlation matrix $\boldsymbol{R}$ and output $\boldsymbol{U}$ have been dropped for notational convenience. In doing the minimisation outlined in (46), the optimal parameters are given by

$$\begin{aligned} \beta^*(\boldsymbol{\theta}) &= \left(\mathbf{1}^T \boldsymbol{R}^{-1}(\boldsymbol{\theta}) \mathbf{1}\right)^{-1} \mathbf{1}^T \boldsymbol{R}^{-1}(\boldsymbol{\theta}) \boldsymbol{U}, \\ \sigma^{2^*}(\boldsymbol{\theta}) &= \frac{1}{A} \left(\boldsymbol{U} - \mathbf{1}\beta^*(\boldsymbol{\theta})\right)^T \boldsymbol{R}^{-1}(\boldsymbol{\theta}) \left(\boldsymbol{U} - \mathbf{1}\beta^*(\boldsymbol{\theta})\right). \end{aligned} \tag{48}$$

The only remaining unknowns are the set of hyperparameters $\boldsymbol{\theta}$ which are more complex in nature, thus requiring an optimisation algorithm to solve. The authors select the *boxmin* algorithm [48] however alternative algorithms are available (e.g. quasi-Newton methods [49], genetic algorithms [50] or gradient descent type algorithms such as *fmincon*, commonly known to MatLab users [51]). Any of these algorithms will require an objective function to optimise the hyperparameters against which draws upon a reduced opposite log-likelihood found by substituting the optimised parameters $\{\beta^*, \sigma^{2^*}\}$ into (47) and neglecting the constant terms yielding

$$\bar{\mathscr{L}}\left(\boldsymbol{U} | \beta, \sigma^2, \boldsymbol{\theta}\right) = \frac{A}{2} \log\left(\sigma^{2^*}(\boldsymbol{\theta})\right) + \frac{1}{2} \log(|\boldsymbol{R}|(\boldsymbol{\theta})), \tag{49}$$

from which the fully reduced form can be retrieved as

$$\psi(\boldsymbol{\theta}) = \sigma^{2^*}(\boldsymbol{\theta}) |\boldsymbol{R}(\boldsymbol{\theta})|^{\frac{1}{A}}, \tag{50}$$

which is used for the objective function. The full details for obtaining (50) can be found in Appendix F.

4.2. Metamodel evaluation

Having identified the model parameters and hyperparameters in Section 4.1, it is now possible to conduct evaluation of the metamodel. Take now, an unobserved set of input prediction sites $\mathbf{I}^{\bullet} \in \mathbb{R}^{M \times N_{inp}}$ where M is the number of unobserved data points. Since the metamodel is given by a Gaussian distribution its properties allow for the introduction of a joint distribution given by

$$\begin{bmatrix} \boldsymbol{U} \\ \boldsymbol{U}^{\bullet}(\mathbf{I}^{\bullet}) \end{bmatrix} \sim \left(\begin{bmatrix} \mathbf{1} \\ \mathbf{1} \end{bmatrix} \beta^{*}, \sigma^{2^{*}} \begin{bmatrix} \boldsymbol{R} & \boldsymbol{r}^{T}(\mathbf{I}^{\bullet}) \\ \boldsymbol{r}(\mathbf{I}^{\bullet}) & \boldsymbol{I} \end{bmatrix} \right), \tag{51}$$

where it is important to recall that $\boldsymbol{U} = \boldsymbol{U}(\mathbf{I})$, $\boldsymbol{R} = \boldsymbol{R}(\mathbf{I})$, and $\boldsymbol{I}$ is the identity matrix. Note the addition of the cross-correlation matrix $\boldsymbol{r}(\mathbf{I}^{\bullet})$ used to correlate the observed and unobserved data points. Moreover, $\boldsymbol{r}(\mathbf{I}^{\bullet})$ is defined similarly to $\boldsymbol{R}$ as

$$\boldsymbol{r}(\mathbf{I}^{\bullet}) = \begin{bmatrix} \boldsymbol{q}_1 \\ \boldsymbol{q}_2 \end{bmatrix}, \tag{52}$$

where

$$\left[\boldsymbol{q}_1\right]^{(i)(j)} = \mathcal{R}\left(\mathbf{I}^{\bullet(i)}, \mathbf{I}^{(j)}, \boldsymbol{\theta}^{*}\right), \qquad i \in [1, \ldots, M]; \quad j \in [1, \ldots, N], \tag{53}$$

$$\left[\boldsymbol{q}_2\right]_k^{(i)(j)} = \partial_{\mathbf{I}_k^{(j)}} \mathcal{R}, \qquad i \in [1, \ldots, M], \quad j \in [1, \ldots, N], \quad k \in \left[1, \ldots, N_{inp}\right]. \tag{54}$$

Following these definitions, all constituents of (51) have been identified. Finally, to obtain the final predictive distribution the joint distribution in (51) needs to be conditionalised which renders

$$\boldsymbol{U}^{\bullet}(\mathbf{I}^{\bullet}) = \mathbf{1}\beta^{*} + \boldsymbol{r}(\mathbf{I}^{\bullet})\boldsymbol{R}^{-1}\left(\boldsymbol{U} - \mathbf{1}\beta^{*}\right). \tag{55}$$

Note that (55) is the conditional mean and as a result the same outcome will be achieved every evaluation at the same prediction site due to not incorporating any conditional variance. This could of course be simply adjusted if required. In the context of electromechanics, the desired output of the constitutive model is that of the derivatives (i.e. $\boldsymbol{P}$ and $\boldsymbol{E}_0$). These can be obtained from the metamodel by taking derivatives of (55) with respect to $\mathbf{I}^{\bullet}$ via the following

$$\partial_{\mathbf{I}^{\bullet}} \boldsymbol{U}^{\bullet} = \left(\partial_{\mathbf{I}^{\bullet}} \boldsymbol{r}\right) \boldsymbol{R}^{-1} \left(\boldsymbol{U} - \mathbf{1}\beta^{*}\right), \tag{56}$$

where the differential of the cross-correlation matrix is comprised of the following blocks

$$\partial_{\mathbf{I}^{\bullet}} \boldsymbol{r} = \begin{bmatrix} \partial_{\mathbf{I}^{\bullet}} \boldsymbol{q}_1 \\ \partial_{\mathbf{I}^{\bullet}} \boldsymbol{q}_2 \end{bmatrix}, \qquad i \in [1, \ldots, M], \quad j \in [1, \ldots, N], \tag{57}$$

which correspond to

$$\left[\partial_{\mathbf{I}^{\bullet}} \boldsymbol{q}_1\right]_k^{(i)(j)} = \partial_{\mathbf{I}_k^{\bullet(i)}} \mathcal{R}, \qquad i \in [1, \ldots, M], \quad j \in [1, \ldots, N], \quad k \in \left[1, \ldots, N_{inp}\right], \tag{58a}$$

$$\left[\partial_{\mathbf{I}^{\bullet}} \boldsymbol{q}_2\right]_{kl}^{(i)(j)} = \partial^2_{\mathbf{I}_l^{\bullet(i)} \mathbf{I}_k^{(j)}} \mathcal{R}, \qquad i \in [1, \ldots, M], \quad j \in [1, \ldots, N], \quad k, l \in \left[1, \ldots, N_{inp}\right]. \tag{58b}$$

For full definitions of the partial derivatives used in (58a) and (58b), see Appendix C.

5. Numerical examples: metamodel calibration

The following section will provide details around the process of metamodel calibration as well as displaying results of the calibrated metamodels. Section 5.1 will start by outlining the process used to generate experimentally styled synthetic data. Next, the calibration procedure is outlined within Section 5.2 including the definition of the error used to measure the calibration accuracy. The impact of using an infill strategy will then be presented in Section 5.3, followed by the adaptations to enable Kriging to become regression based thus capable of calibrating with noisy data in Section 5.4. Finally, Section 5.5 presents the results of the calibrated metamodels for a variety of electromechanical constitutive models.

5.1. Data generation

A concentric approach to generating the synthetic data for calibration has been utilised for all Kriging metamodels developed for use in this paper. This approach is achieved by defining a set of deviatoric directions and amplitudes which when combined with the basis for traceless symmetric tensors $\boldsymbol{\Psi}$ (see Appendix C of [52]) yields a range of deformation gradient tensors $\boldsymbol{F}$ and electric displacement vectors $\boldsymbol{D}_0$ - for details see Algorithm 3. The procedure is outlined below in Algorithm 2, and follows the methodology used by the authors in [53] and based upon that provided in [52].

Remark 4. Whilst a concentric approach to data generation has been used here, an experimental styled approach consisting of deformation gradient tensors representing uniaxial, biaxial and shear deformations could be used, as carried out in [34]. For the electromechanical case, electric displacements of varying magnitudes would also be sampled.

Algorithm 2 Pseudo-code for process of sampling $\boldsymbol{F}$ and $\boldsymbol{D}_0$.

```
Set the number of amplitudes, directions and determinants: $\{n_t, n_{\boldsymbol{X}}, n_{\boldsymbol{J}}\}$;
Initialise the vector of amplitudes: $t_{\boldsymbol{F}} = [0, \dots, 1.2]_{n_t \times 1}, t_{\boldsymbol{D}_0} = [0, \dots, 1.5]_{n_t \times 1}$;
Initialise the vector of determinants: $\boldsymbol{J} = [0.9, \dots, 1.1]_{n_{\boldsymbol{J}} \times 1}$;
Initialise a vector of Latin Hypercube sampled angles: $\phi_1 = [0, 2\pi]_{n_{\boldsymbol{X}} \times 1}, \varphi_1 = [0, 2\pi]_{n_{\boldsymbol{X}} \times 1}$;
Initialise vectors of Latin Hypercube sampled angles: $\phi_{2,3,4} = [0, \pi]_{n_{\boldsymbol{X}} \times 1}, \varphi_2 = [0, \pi]_{n_{\boldsymbol{X}} \times 1}$;
Construct the directions, $\{\boldsymbol{X}_{\boldsymbol{F}}, \boldsymbol{X}_{\boldsymbol{D}_0}\}$, using the extended spherical parametrisation in $\mathbb{R}^5$ - detailed in Appendix D;
Evaluate the deformation gradient tensors, $\boldsymbol{F}$, and electric displacement vectors, $\boldsymbol{D}_0$, parametrised in terms of deviatoric directions
    $\{\boldsymbol{X}_{\boldsymbol{F}}, \boldsymbol{X}_{\boldsymbol{D}_0}\}$, amplitudes $\{t_{\boldsymbol{F}}, t_{\boldsymbol{D}_0}\}$, and determinants $\boldsymbol{J}$ - detailed in Algorithm 3.
```

Algorithm 3 Pseudo-code for process of constructing the set of $\boldsymbol{F}$ and $\boldsymbol{D}_0$.

```
for $i = 1 : n_{\boldsymbol{X}}$ do
    for $j = 1 : n_{\boldsymbol{J}}$ do
        for $k = 1 : n_t$ do
            $\boldsymbol{F} = J_j^{1/3} \exp\left(t_{\boldsymbol{F}_k}\left[\sum_{l=1}^{5} X^i_{\boldsymbol{F}_l} \boldsymbol{\Psi}_l\right]\right)$;
            $\boldsymbol{D}_0 = t_{\boldsymbol{D}_{0k}} \boldsymbol{X}^i_{\boldsymbol{F}}$;
        end for
    end for
end for
```

Algorithm 4 Pseudo-code for the entire Kriging metamodel calibration process.

```
1:  Sample a set of deformation gradient tensors $\boldsymbol{F}$ and electric displacements $\boldsymbol{D}_0$ - see Algorithm 2
2:  Evaluate the ground truth stress $\boldsymbol{P}$, electric field $\boldsymbol{E}_0$, and energy $U$ - see models in Appendix E
3:  Conduct hierarchical structure discovery to identify a suitable anisotropic class - see Section 3
4:  Evaluate the singular matrices using singular value decomposition: $\hat{\boldsymbol{U}}, \boldsymbol{\Lambda}, \hat{\boldsymbol{V}} = \text{SVD}(\boldsymbol{F})$ - see (14)
5:  Evaluate the anisotropic and multiphysics invariants - see the relevant subsections of Section 2.4
6:  Evaluate the projections of $\boldsymbol{P}$ and $\boldsymbol{E}_0$: $\partial_{\boldsymbol{I}} U$ - see Section 3.1
7:  Conduct the parameter minimisation: $\{\beta^*, \sigma^{2^*}\} = \arg\min_{\beta, \sigma^2} \mathscr{L}\left(\boldsymbol{U} | \beta, \sigma^2, \boldsymbol{\theta}\right)$ - see (48)
8:  Conduct the hyperparameter optimisation: $\boldsymbol{\theta}^* = \arg\min_{\boldsymbol{\theta}} \psi(\boldsymbol{\theta})$ - see (50)
9:  Evaluate a test dataset - see Section 4.2
10: Assess the success of the calibrated metamodel - see (62) and (63)
11: if Using an infill strategy and metamodel error > tolerance then
12:     Update the calibration set with points of highest error - see Section 5.3
13:     goto step 4:
14: end if
```

5.2. Calibration procedure

Following dataset generation, the Kriging metamodel can be calibrated. This procedure has been covered in considerable detail in Section 4 and an overview has been outlined below for convenience in Algorithm 4.

5.3. Infill strategy

As with all ML approaches the quality of the input data for calibration is of the upmost importance on the accuracy of the developed metamodel. In some cases, the approach to improve accuracy is to introduce a bulk of calibration data. However, this can lead to an oversized dataset where unnecessary data exists due to the random selection or generation. Therefore, to ensure that a minimal amount of data is being used and that all of the selected points are useful and necessary, an infill strategy is utilised. This involves starting with a small dataset to calibrate a metamodel, before evaluating against a test dataset. An error is then evaluated for all test data points and the ones with the largest error are selected as infill data points for the new calibration dataset. Several possible error measurements are available, such as error in first derivative - the first Piola-Kirchhoff stress tensor - as in [30,53] or utilising Kriging's probabilistic properties to produce an error based upon uncertainty as in [54]. The authors conducted a comparison of these two strategies previously in [34] demonstrating that it is advantageous to utilise the uncertainty based error. To highlight the benefits to using an infill strategy the reader's attention is directed to Fig. 7.

Two anisotropic constitutive models are presented in Fig. 7, a transversely isotropic material in Fig. 7(a) and a rank-one laminate material in Fig. 7(b) - for constitutive model specifics the reader is referred to Appendix E.3 and ROL(a) in Appendix E.4, respectively. Both materials showcase a very similar pattern when applying an infill strategy which is that utilising an uncertainty based approach (denoted with circle markers) enables a continuous improvement in error for both derivative quantities. This highlights the significance of allowing the uncertainty provided by Kriging directly, to select the most relevant data points as opposed to simply randomly

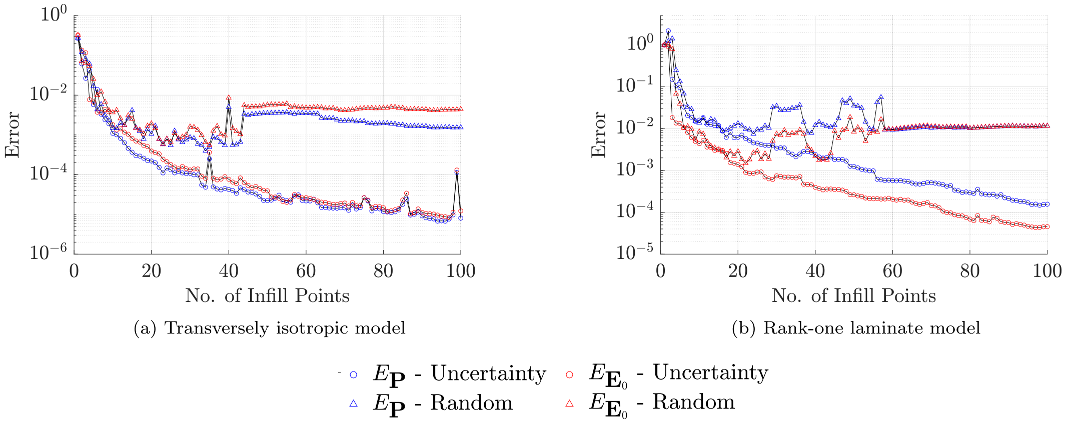

(a) Transversely isotropic model

(b) Rank-one laminate model

Fig. 7. Showcases the benefit of utilising an infill strategy over simply increasing the dataset size for two anisotropic constitutive models. Subfigures (a) and (b) present the evolution of the L2 error in stress, $E_{\boldsymbol{P}}$ (blue), and electric field $E_{\boldsymbol{E}_0}$ (red) for an uncertainty based infill approach (circles), and a randomly increasing dataset size (triangles). For the L2 error equations the reader is directed to (63).(For interpretation of the references to color in this figure legend, the reader is referred to the web version of this article.)

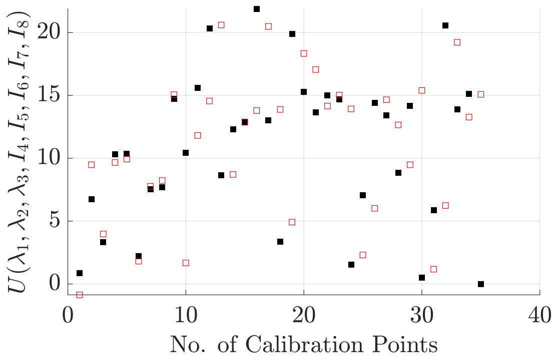

Fig. 8. Showcases the noisy calibration set where the black squares denote the unperturbed dataset and the red squares demonstrate the magnitude of the incorporated noise.(For interpretation of the references to color in this figure legend, the reader is referred to the web version of this article.)

growing the dataset (denoted by the triangular markers). Note that in Fig. 7 the infill strategy is for 100 data points increasing in single point increments. This is used to show the trend but the aim is generally to use far fewer ensuring a simpler calibration process and fast evaluation capability of the Kriging metamodel - heavily dependant on the size of the correlation matrix which itself is related to the number of data points (see Section 4.1).

5.4. Noise regularisation

The Kriging approach detailed thus far is a direct interpolation method which will only be effective for a perfectly sampled dataset which does not contain any noise. It is simple however, to extend Kriging's capability to handle a realistic noisy dataset, which involves introducing two new hyperparameters [55]. By using the definition of $\boldsymbol{R}(\mathbf{I}, \boldsymbol{\theta})$ stated in (43), Kriging will attempt to directly interpolate between all noisy data points resulting in an ill-posed correlation matrix $\boldsymbol{R}(\mathbf{I}, \boldsymbol{\theta})$. To alleviate this, two perturbation terms ϵ_1 and ϵ_2 are introduced to augment $\boldsymbol{R}(\mathbf{I}, \boldsymbol{\theta})$ as follows

$$\boldsymbol{R}(\mathbf{I}, \boldsymbol{\theta}) = \begin{bmatrix} \boldsymbol{Q}_{11} + \epsilon_1 \boldsymbol{I} & \boldsymbol{Q}_{12} \\ \boldsymbol{Q}_{12}^T & \boldsymbol{Q}_{22} + \epsilon_2 \boldsymbol{I} \end{bmatrix}, \tag{59}$$

where $\boldsymbol{I}$ is the identity matrix. Notice that there are two perturbation terms, ϵ_1 for the functional correlation block $\boldsymbol{Q}_{11}$ and ϵ_2 for the derivative correlation block $\boldsymbol{Q}_{22}$ [29]. To calibrate these additional hyperparameters, the optimisation process outlined in Section 4.1 remains the same with an extended set $\boldsymbol{\theta} = \left\{\theta_1, \dots, \theta_{N_{inp}}, \epsilon_1, \epsilon_2\right\}$. To demonstrate Kriging's capability to handle noisy data, an example calibration of a noisy data sample for a transversely isotropic ideal dielectric constitutive model is presented below - see Appendix E.3 for details of the material parameters. Firstly, the noisy calibration dataset can be seen in Fig. 8, where the black square points represent the ground truth data and the red squares indicate the perturbed data as a result of the added random noise.

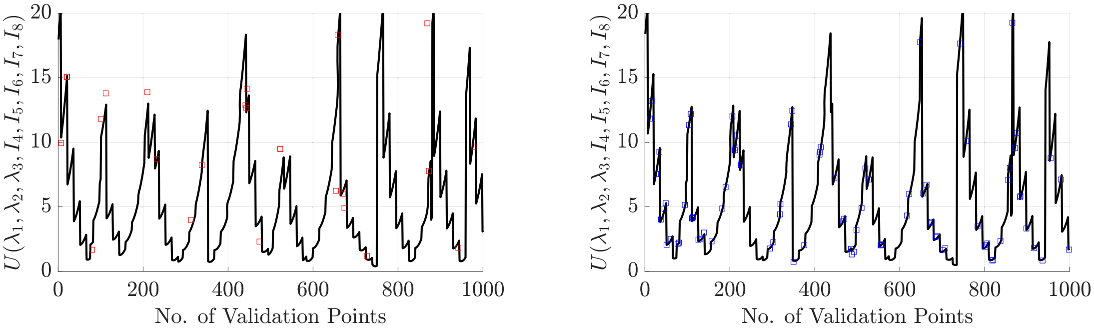

(a) Calibration dataset

(b) Evaluated Kriging metamodel

Fig. 9. Showcases the successful calibration of a regression Kriging metamodel where (a) displays the perturbed calibration dataset denoted by red squares over the ground truth unperturbed black lined curve; (b) portrays now the Kriging metamodel output as the black lined curve with a random selection of 100 ground truth data points denoted by blue squares.(For interpretation of the references to color in this figure legend, the reader is referred to the web version of this article.)

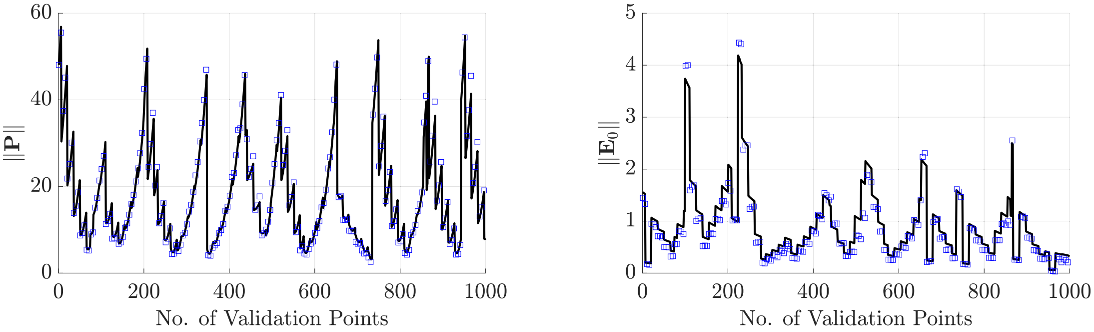

(a) Evaluated $\boldsymbol{P}$ for the Kriging metamodel

(b) Evaluated $\boldsymbol{E}_0$ for the Kriging metamodel

Fig. 10. Showcases the evaluation of the derivative quantities from the calibrated regression Kriging metamodel where (a) displays the ground truth $\|\boldsymbol{P}\|$ denoted by the black solid curve and the evaluated Kriging counterpart for 200 data points in the blue squares; (b) portrays now the ground truth $\|\boldsymbol{E}_0\|$ denoted by the black solid curve and the evaluated Kriging counterpart for 200 data points in the blue squares.(For interpretation of the references to color in this figure legend, the reader is referred to the web version of this article.)

To generate the perturbations of the dataset seen in Fig. 8, a zero mean Gaussian was added to the original dataset. This perturbation via a Gaussian distribution was characterised by

$$\tilde{U} = U + \mathcal{N}(0, \sigma_U), \qquad \widetilde{\partial_{\mathrm{I}} U} = \partial_{\mathrm{I}} U + \mathcal{N}\left(0, \sigma_{\partial_{\mathrm{I}} U}\right), \tag{60}$$

where

$$\sigma_U = 0.2\bar{U}, \qquad \sigma_{\partial_{\mathrm{I}} U} = 0.2\overline{\partial_{\mathrm{I}} U}, \tag{61}$$

moreover, where $\tilde{\blacksquare}$ denotes the perturbed datasets and $\bar{\blacksquare}$ represents the average of a quantity. Upon calibration of the metamodel using the 35 data points presented in Fig. 8, the metamodel was evaluated for the entire validation dataset of 1000 points - where to clarify each data point within the validation dataset consists of a specific $\{\boldsymbol{F}, \boldsymbol{D}_0\}$ and hence corresponding $\{\boldsymbol{P}, \boldsymbol{E}_0\}$. These results of which can be seen by the solid black line in Fig. 9(b) which is overlaid with a scattering of 100 ground truth data points denoted by the blue squares. The agreement that can be seen in Fig. 9 demonstrates a strong construction of a regression metamodel considering the level of noise witnessed in Fig. 9(a).

To further highlight the success, the norm of the derivative quantities - $\boldsymbol{P}$ and $\boldsymbol{E}_0$ - can also been seen in Fig. 10 where the full ground truth validation dataset is plotted with a black continuous line and 200 Kriging evaluations have been overlaid using blue square markers. Note that the 200 were chosen by evaluating and plotting every fifth data point from the validation dataset. The accuracy of the metamodel's prediction of $\boldsymbol{P}$ is very good noting that only the extrema points seem to deviate from the ground truth curve in black. $\boldsymbol{E}_0$ on the other hand, could still be improved but the trend shows a good correlation. It is important to state the success given that this is a challenging model to capture consisting of eight input features all of which are handling a significant magnitude of random noise.

In order to ensure the assessment of the noisy data is sufficient and accurate, a convergence study was carried out. This involved evaluating the calibrated Kriging metamodel on the validation dataset which to start with consisted of the full 1000 validation data points. Then 50 validation data points were randomly selected to be removed and Kriging re-evaluated, a process repeated until

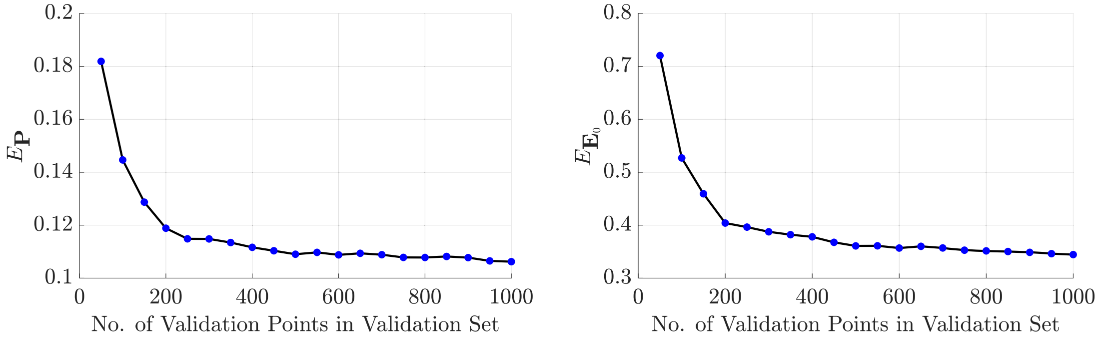

(a) Error in $\boldsymbol{P}$ (b) Error in $\boldsymbol{E}_0$

Fig. 11. Displays the convergence in errors for both (a) first Piola-Kirchhoff stress tensor $\boldsymbol{P}$ and (b) material electric field vector $\boldsymbol{E}_0$ as the size of the validation dataset increases.

Table 2
Presents the calibration results via a selection of metrics for a range of Kriging metamodels which utilise 5 infill data points.

Constitutive Model:	No. Data:	Errors in $\boldsymbol{P}$			Errors in $\boldsymbol{E}_0$		
		R^2	$E_{\boldsymbol{P}}$	$\hat{E}_{\boldsymbol{P}}$	R^2	$E_{\boldsymbol{E}_0}$	$\hat{E}_{\boldsymbol{E}_0}$
OG	19	1.0000	5.22×10^{-3}	1.41×10^{-2}	1.0000	3.72×10^{-3}	2.04×10^{-2}
MR	19	1.0000	2.01×10^{-3}	1.78×10^{-2}	1.0000	2.75×10^{-4}	4.53×10^{-3}
TI	11	1.0000	5.77×10^{-3}	1.03×10^{-1}	0.9998	6.75×10^{-3}	4.05×10^{-2}
ROL(a)	8	0.9868	9.50×10^{-2}	1.01×10^{0}	0.9997	1.33×10^{-2}	6.66×10^{-2}
ROL(b)	8	0.9535	1.70×10^{-1}	1.30×10^{0}	0.9982	2.34×10^{-2}	1.39×10^{-1}
ROL(c)	8	0.9633	1.58×10^{-1}	5.26×10^{-1}	0.9916	7.19×10^{-2}	4.58×10^{-1}

only 50 points remained in the validation dataset. The results for this study can be seen in Fig. 11 and showcase convergence of the error at approximately 800 points which provides confidence that the size of the chosen dataset is sufficient to accurately assess the performance of the calibration.

5.5. Metamodel calibration results

Having discussed the procedure for metamodel calibration, it is necessary to now demonstrate a range of calibration results. But before doing so, it is important to define the metrics used to evaluate the calibrations success. The most common metric being used is that of the L2 error which is denoted for the two derivatives by

$$\hat{E}_{\boldsymbol{P}} = \frac{\|\boldsymbol{P}_{GT} - \boldsymbol{P}_{KR}\|}{\|\boldsymbol{P}_{GT}\|}, \qquad \hat{E}_{\boldsymbol{E}_0} = \frac{\|\boldsymbol{E}_{0GT} - \boldsymbol{E}_{0KR}\|}{\|\boldsymbol{E}_{0GT}\|}, \tag{62}$$

where $\|\blacksquare\|$ represents the L2 norm and $\boldsymbol{P}_{GT}$, $\boldsymbol{P}_{KR}$, $\boldsymbol{E}_{0GT}$, $\boldsymbol{E}_{0KR}$ are the vectorised quantities of the ground truth and Kriging first Piola-Kirchhoff stress tensors and ground truth and Kriging material electric fields, respectively. Whilst $\hat{E}_{\boldsymbol{P}}$ and $\hat{E}_{\boldsymbol{E}_0}$ provide the local error for a single data point, the following give a total error across all data points within a validation set

$$E_{\boldsymbol{P}} = \frac{\sum_{i=1}^{n} \|\boldsymbol{P}_{GT}^{i} - \boldsymbol{P}_{KR}^{i}\|}{\sum_{i=1}^{n} \|\boldsymbol{P}_{GT}^{i}\|}, \qquad E_{\boldsymbol{E}_0} = \frac{\sum_{i=1}^{n} \|\boldsymbol{E}_{0GT}^{i} - \boldsymbol{E}_{0KR}^{i}\|}{\sum_{i=1}^{n} \|\boldsymbol{E}_{0GT}^{i}\|}, \tag{63}$$

where n is the number of data points in the validation dataset. The other common metric for assessing ML calibration is the R^2 value defined generically for some quantity $\boldsymbol{A}$ as

$$R^2 = \frac{\sum_{i=1}^{n} \|\bar{\boldsymbol{A}}_{GT} - \boldsymbol{A}_{KR}^{i}\|}{\sum_{i=1}^{n} \|\boldsymbol{A}_{GT}^{i} - \bar{\boldsymbol{A}}_{GT}\|}. \tag{64}$$

With these metrics defined, a series of example metamodels will be presented. Table 2 presents the results for six calibrated constitutive models consisting of isotropy in the form of Ogden (OG) and Mooney-Rivlin (MR) as well as anisotropic in the form of transverse isotropy (TI) and three different forms of the rank-one laminates (ROL). For detailed information of these constitutive models see Appendixes E.2 to E.5.

Table 2 showcases the calibration results for six constitutive models with each calibration only including five infill data points - selected based upon uncertainty - resulting in a very small overall calibration dataset size as seen in the second column. Having such small dataset sizes is not suitable for calibrating the anisotropic models however, both the Ogden and Mooney-Rivlin models have

Table 3
Presents the calibration results via a selection of metrics for a range of Kriging metamodels which utilise 10 infill data points.

Constitutive Model:	No. Data:	Errors in $\boldsymbol{P}$			Errors in $\boldsymbol{E}_0$		
		R^2	$E_{\boldsymbol{P}}$	$\hat{E}_{\boldsymbol{P}}$	R^2	$E_{\boldsymbol{E}_0}$	$\hat{E}_{\boldsymbol{E}_0}$
OG	24	1.0000	5.24×10^{-3}	1.67×10^{-2}	1.0000	2.71×10^{-3}	1.76×10^{-2}
MR	24	1.0000	3.50×10^{-3}	1.19×10^{-2}	1.0000	1.11×10^{-3}	3.78×10^{-3}
TI	16	1.0000	1.10×10^{-3}	1.93×10^{-2}	1.0000	1.80×10^{-3}	1.88×10^{-2}
ROL(a)	13	0.9993	1.59×10^{-2}	7.92×10^{-2}	1.0000	4.37×10^{-3}	2.60×10^{-2}
ROL(b)	13	0.9978	3.67×10^{-2}	2.79×10^{-1}	0.9997	1.42×10^{-2}	6.28×10^{-2}
ROL(c)	13	0.9928	7.78×10^{-2}	9.81×10^{-1}	0.9994	2.16×10^{-2}	1.24×10^{-1}

Table 4
Presents the calibration results via a selection of metrics for a range of Kriging metamodels which utilise 20 infill data points.

Constitutive Model:	No. Data:	Errors in $\boldsymbol{P}$			Errors in $\boldsymbol{E}_0$		
		R^2	$E_{\boldsymbol{P}}$	$\hat{E}_{\boldsymbol{P}}$	R^2	$E_{\boldsymbol{E}_0}$	$\hat{E}_{\boldsymbol{E}_0}$
OG	34	1.0000	2.26×10^{-3}	7.73×10^{-3}	1.0000	1.49×10^{-3}	1.27×10^{-2}
MR	34	1.0000	2.80×10^{-3}	1.48×10^{-2}	1.0000	1.02×10^{-3}	5.32×10^{-3}
TI	26	1.0000	2.20×10^{-4}	4.34×10^{-3}	1.0000	3.93×10^{-4}	6.84×10^{-3}
ROL(a)	23	0.9999	6.17×10^{-3}	2.88×10^{-2}	1.0000	1.39×10^{-3}	1.82×10^{-2}
ROL(b)	23	0.9999	6.68×10^{-3}	2.43×10^{-2}	1.0000	3.93×10^{-3}	3.52×10^{-2}
ROL(c)	23	0.9998	8.35×10^{-3}	5.74×10^{-2}	1.0000	3.86×10^{-3}	3.44×10^{-2}

great accuracy across both the mechanical and electrostatic error metrics. Notably the error in electric field for the Mooney-Rivlin model calibrated on only 19 data points is a staggering 2.75×10^{-4}.

It was clear that the dataset sizes for the anisotropic models were just too small, so Table 3 presents the results for the calibration using five additional infill data points. Notice, that for the anisotropic models, simply adding five additional infill points seemingly improves the accuracy in $E_{\boldsymbol{P}}$ achieved for mechanics by approximately an order of magnitude - an astounding improvement for so little data added. This improvement enables the transversely isotropic model to now be at a usable accuracy level with errors in stress and electric field at 1.10×10^{-3} and 1.80×10^{-3} respectively.

Moreover, an extra ten infill data points were provided to each constitutive models calibration dataset and the results of which are provided in Table 4. In doing so the focus can now turn to the three rank-one laminate models. Each model (a) to (c) has an increasing level of mechanical and electrical contrast respectively furthering the materials complexity - see Appendix E.4 for full details. Given this, the calibration also becomes more challenging therefore highlighting how impressive calibrating an accurate model is - with R^2 values approaching 1.0000 - with merely 23 data points.

5.5.1. RVE calibration results

Thus far, the laminate composite form has been presented, however, the inclusion form has not been covered. Notably, the inclusion configuration is significantly more challenging given that the underlying constitutive model is unknown. Four calibrated metamodels are discussed through this section with two related to the inclusion geometries demonstrated previously in Fig. 6. As illuded to in Section 3, stress and electric field data for RVEs comes directly from running Finite Element simulations due to no underlying analytical models existing. Instead, a multi-scale homogenisation procedure takes place within a FEM2 approach and the resulting data taken to construct a calibration and validation dataset. Fig. 12 displays the meshes consisting of quadratic tetrahedral elements, used for the four different RVE configurations. For these examples, the simulations take place using the Helmholtz energy, namely $\Psi(\boldsymbol{F}, \boldsymbol{E}_0)$ thus leading to the derivative outputs being $\partial_{\boldsymbol{F}} \Psi(\boldsymbol{F}, \boldsymbol{E}_0)$ and $\partial_{\boldsymbol{E}_0} \Psi(\boldsymbol{F}, \boldsymbol{E}_0)$ yielding $\boldsymbol{P}$ and $-\boldsymbol{D}_0$, respectively. In order to keep continuity between the procedure for RVEs and all other constitutive models, metamodels were calibrated still on invariants of $\boldsymbol{F}$ and $\boldsymbol{D}_0$ - i.e. the internal energy $e(\boldsymbol{F}, \boldsymbol{D}_0)$. The resulting calibrated models were suboptimal and it was deemed that by switching variables there was an induced nonlinearity from an effective Legendre transform being applied. As a result, the metamodel was also calibrated upon the Helmholtz energy - i.e. the input quantities are invariants based on $\boldsymbol{F}$ and $\boldsymbol{E}_0$ - which yielded successful results. Note this has an impact on the definitions for the invariants set out in Section 2.4.3 since now all electrostatic invariants should consist of $\boldsymbol{E}_0$ as opposed to $\boldsymbol{D}_0$. Furthermore, the coupled invariant I_5 of $\boldsymbol{F}\boldsymbol{D}_0 \cdot \boldsymbol{F}\boldsymbol{D}_0$ had to be replaced with $\boldsymbol{H}\boldsymbol{E}_0 \cdot \boldsymbol{H}\boldsymbol{E}_0$ - as it is the natural invariant as a result of the Legendre transform. The results of all four calibrations can be seen in Table 5.

The first quantity of interest is column two of Table 5 which demonstrates that considerably more data points are required with these substantially more challenging datasets to still achieve a reasonable accuracy. In this case, very few data points were introduced in the initial calibration set and then infill points were added in to ensure that the minimal number of data points were being used. The errors associated with the metamodel calibration can be found in the remainder of the columns in Table 5 which indicates reasonable metamodel calibrations. Furthermore the R^2 plots for both error in the Piola-Kirchhoff stress tensor and electric displacement vector can be found for all metamodels in Fig. 13, reiterating the success of the calibration.

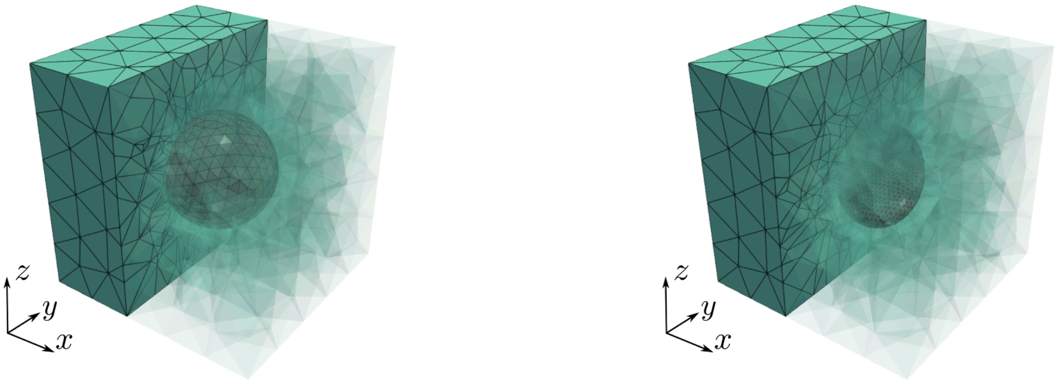

(a) RVE(a) - Spherical Inclusion (b) RVE(b) - Ellipsoidal Inclusion

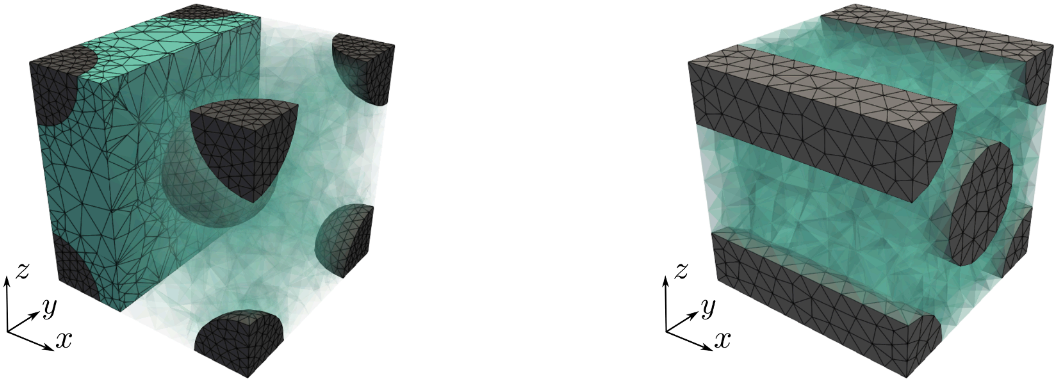

(c) RVE(c) - Body Centred Cubic (d) RVE(d) - Face Centred Fibre

Fig. 12. Presents the meshes used to generate the data for the respective RVE datasets. Further information around the material models for the matrix and inclusion can be found in Appendix E.5.

Table 5
Presents the calibration results via a selection of metrics for four Kriging metamodels based upon RVE data (RVE(a) with a spherical inclusion, RVE(b) with an ellipsoidal inclusion, RVE(c) as a body centred cubic, and RVE(d) as a face centred fibre) which utilise 40, 44, 40, and 20 infill data points, respectively.

Constitutive Model:	No. Data:	Errors in $\boldsymbol{P}$			Errors in $\boldsymbol{D}_0$		
		R^2	$E_{\boldsymbol{P}}$	$\hat{E}_{\boldsymbol{P}}$	R^2	$E_{\boldsymbol{D}_0}$	$\hat{E}_{\boldsymbol{D}_0}$
RVE(a)	48	0.9998	1.28×10^{-2}	5.69×10^{-2}	0.9989	2.05×10^{-2}	1.00×10^{-1}
RVE(b)	59	0.9984	3.06×10^{-2}	1.06×10^{-1}	0.9958	3.02×10^{-2}	1.77×10^{-1}
RVE(c)	54	0.9972	3.78×10^{-2}	1.17×10^{-1}	0.9932	3.87×10^{-2}	2.78×10^{-1}
RVE(d)	26	0.9923	6.05×10^{-2}	2.05×10^{-1}	0.9703	1.06×10^{-1}	2.90×10^{-1}

To further demonstrate the success and accuracy when utilising a metamodel calibrated on RVE data, three RVE models were developed and tested on selected load paths. The first example uses the metamodel calibrated on data from the RVE with a spherical inclusion (refer to RVE(a) in Appendix E.5 for more details) and was evaluated upon a load path which combines a uniaxial and shear response via a deformation gradient tensor and electric field vector defined via

$$\boldsymbol{F} = \begin{bmatrix} \lambda & \gamma & 0 \\ 0 & 1 & 0 \\ 0 & 0 & \frac{1}{\lambda} \end{bmatrix}, \qquad \boldsymbol{E}_0 = \begin{bmatrix} 0.1 \\ 0.1 \\ 0.5 \end{bmatrix}, \tag{65}$$

for

$$\lambda \in [0.5, \dots, 2.5], \qquad \gamma \in [0, \dots, 0.7]. \tag{66}$$

The numerical ground truth response and Kriging evaluation can be found in Fig. 14, where the ground truth data is shown through a solid line and the Kriging metamodel prediction from the circular markers. The Kriging prediction for the stress tensor in Fig. 14(a) appears very accurate with very strong agreement throughout the load path. This is echoed for the electric displacement as seen in Fig. 14(b).

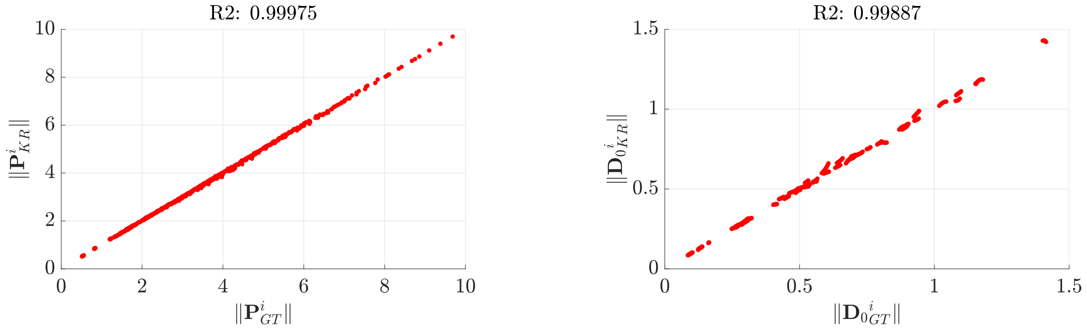

(a) RVE(a): R^2 plot for stress

(b) RVE(a): R^2 plot for electric displacement

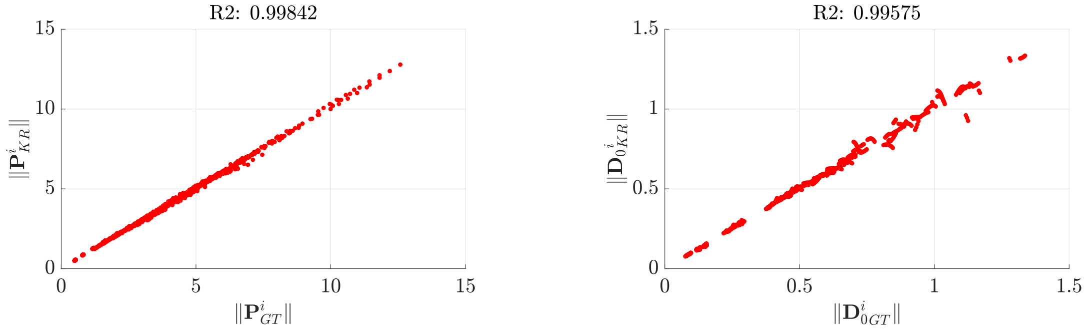

(c) RVE(b): R^2 plot for stress

(d) RVE(b): R^2 plot for electric displacement

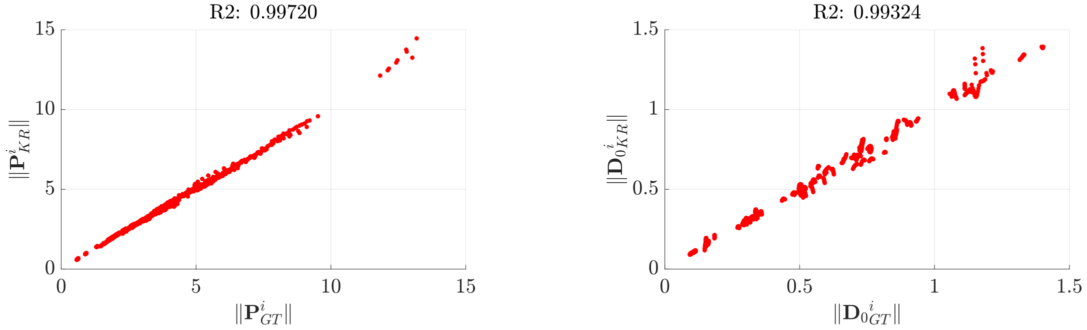

(e) RVE(c): R^2 plot for stress

(f) RVE(c): R^2 plot for electric displacement

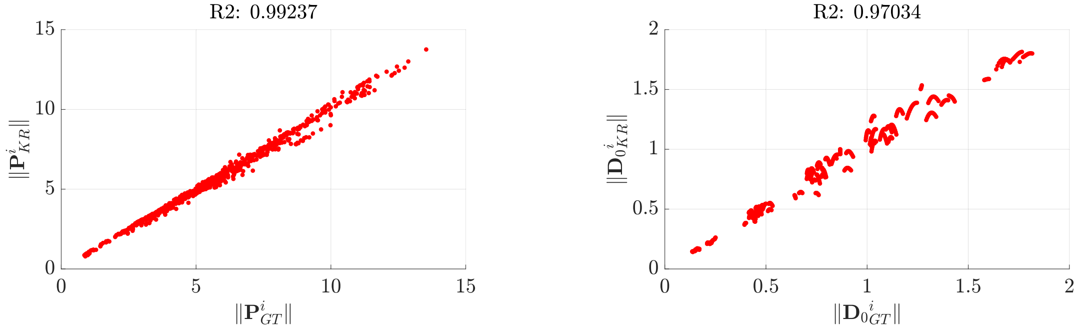

(g) RVE(d): R^2 plot for stress

(h) RVE(d): R^2 plot for electric displacement

Fig. 13. Displays the R^2 plots for both the electric displacement and stress data for all four RVE models.

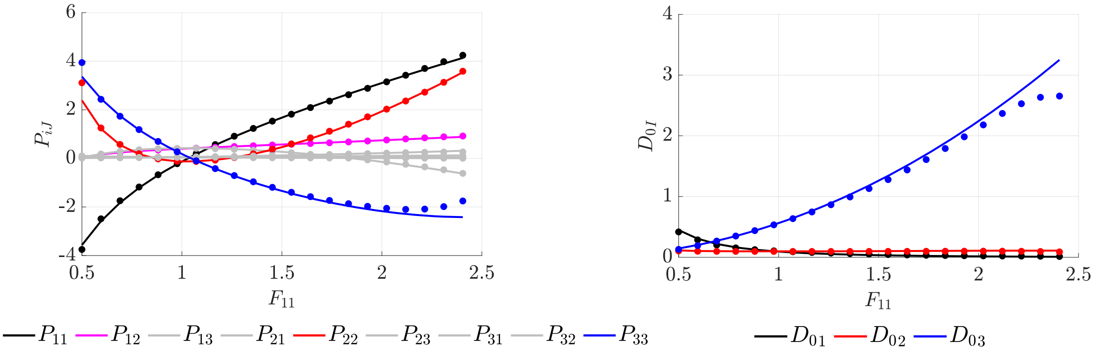

(a) Components of $\boldsymbol{P}$

(b) Components of $\boldsymbol{D}_0$

Fig. 14. Presents the load path validation for the RVE(a) constitutive model with the spherical inclusion. Subfigure (a) shows the components $\boldsymbol{P}$ whilst (b) shows the components of $\boldsymbol{D}_0$ where the solid lines represent the ground truth solution and the circle markers denote the Kriging metamodel evaluation.

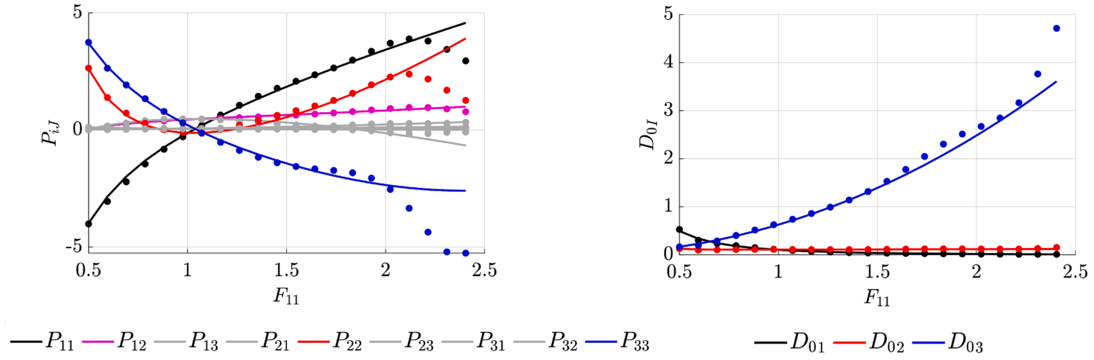

(a) Components of $\boldsymbol{P}$

(b) Components of $\boldsymbol{D}_0$

Fig. 15. Presents the load path validation for the RVE(c) constitutive model with the body centred cubic configuration. Subfigure (a) shows the components $\boldsymbol{P}$ whilst (b) shows the components of $\boldsymbol{D}_0$ where the solid lines represent the ground truth solution and the circle markers denote the Kriging metamodel evaluation.

The next example showcases the metamodel developed on data from RVE(c) - the body centred cubic (see Appendix E.5 for additional details). Note that the load path follows the same uniaxial and shear combination presented in (65) and the results can be seen in Fig. 15. Through the compression phase, the agreement is once again strong between the ground truth data and the Kriging prediction, but this does appear to lose accuracy in Fig. 15(a) beyond an F_{11} value of 2.0. This is likely to be due to Kriging being used for extrapolation at this point, which is not necessarily an objective of the Kriging framework since its performance in extrapolation cannot be guaranteed.

Thirdly, an example presenting the evaluation of the Kriging metamodel developed to predict the response of RVE(d), a face centred fibre configuration (see Appendix E.5 for more information), can be found in Fig. 16. For this example, the load path is evaluated using

$$\boldsymbol{F} = \begin{bmatrix} \lambda & \gamma & 0 \\ 0 & 0.98\lambda & 0 \\ 0 & 0 & \frac{1}{\lambda^2} \end{bmatrix}, \qquad \boldsymbol{E}_0 = \begin{bmatrix} 0.1 \\ -0.1 \\ 0.3 \end{bmatrix}, \tag{67}$$

for

$$\lambda \in [0.7, \dots, 1.5], \qquad \gamma \in [0, \dots, 0.3], \tag{68}$$

which provides a combined biaxial and shear response. Once more, a great likeness can be seen between the ground truth response and the Kriging predicted load path for both the stress response in Fig. 16(a) and electric displacement response in Fig. 16(b).

6. Numerical examples: 3D simulations

This section aims to provide a comprehensive series of numerical examples showcasing the successful implementation of Kriging constitutive metamodels for a range of material models and problems. Section 6.1 will demonstrate the use of an isotropic mate-

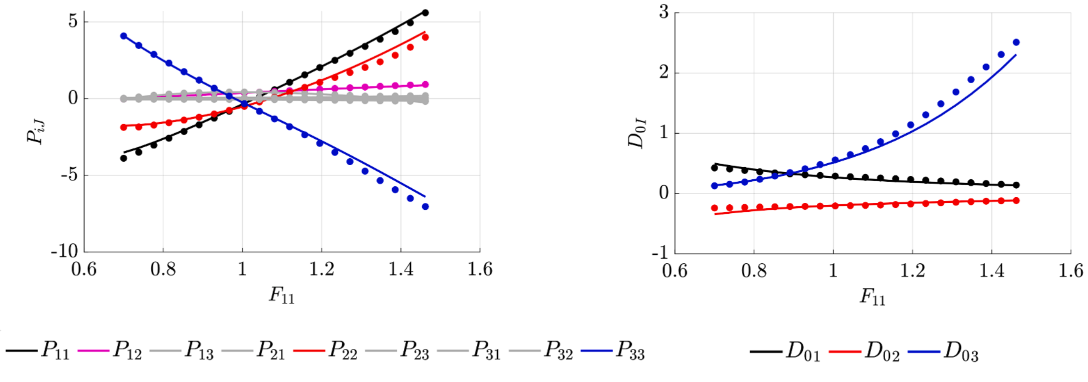

(a) Components of $\boldsymbol{P}$

(b) Components of $\boldsymbol{D}_0$

Fig. 16. Displays the load path validation for the RVE(d) constitutive model with the face centred fibre configuration. Subfigure (a) shows the components $\boldsymbol{P}$ whilst (b) shows the components of $\boldsymbol{D}_0$ where the solid lines represent the ground truth solution and the circle markers denote the Kriging metamodel evaluation.

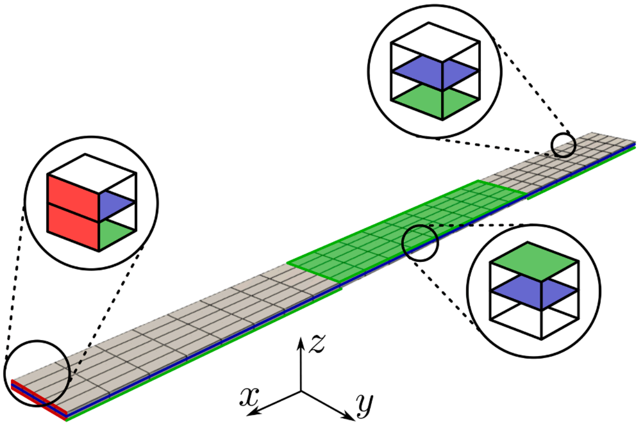

Fig. 17. Depicts the schematic of the $1.5 \times 0.1 \times 0.01(m)$ domain and boundary conditions used for Examples 1, 2, and 3. The red region shows the fixed surface, whilst the blue line indicates the midway surface with an electric potential set to zero. The green regions showcase the surfaces where a non zero electric potential is prescribed. Note that the domain for the simulations is discretised into $\{75, 5, 2\}$ in the $\{x, y, z\}$ directions, respectively.(For interpretation of the references to color in this figure legend, the reader is referred to the web version of this article.)

rial model with a complex bending configuration, whilst Sections 6.2 and 6.3 showcases the change of deformation as a result of the introduction of anisotropy. Section 6.4 displays an isotropic Ogden model in a frilling configuration where a combination of inhomogeneous electric fields induce complex bending. To finish, Section 6.5 will display a set of wrinkling plate examples which utilise a rank-one laminate constitutive model with varying magnitudes of mechanical and electrical contrast influencing the yielded deformations.

To produce the 3D FEM numerical results, a custom in-house framework is used with the same Finite Element discretisation for all simulations. Specifically, quadratic hexahedral elements are employed for the discretisation of both the displacement and electric potential fields. Further information regarding domain dimensions are provided in each example subsection.

6.1. Example 1 - isotropic complex bending

The first example induces a complex bending mode for an isotropic Ideal Dielectric Mooney-Rivlin material model - details of which can be found in Appendix E.2. This is achieved by fixing the surface at $x_{\max}$ (red region in Fig. 17), prescribing an electric potential of 2.6×10^{-3} (V) to specific regions of the upper and lower surface (green regions in Fig. 17), and setting zero electric potential to the middle plane (blue line in Fig. 17). The domain is discretised into $\{75, 5, 2\}$ elements in the $\{x, y, z\}$ directions, respectively, and detailed boundary conditions can be seen in Fig. 17.

The resulting deformations due to the configuration can be seen in Fig. 18. Specifically, Fig. 18(a) displays the progression in increasing electric field of the bending actuator. Though not obvious due to the exceptionally calibrated Kriging metamodel, Fig. 18(a) consists of a side-by-side view of the FEM results with both the ground truth (left) and Kriging (right) implemented constitutive models.

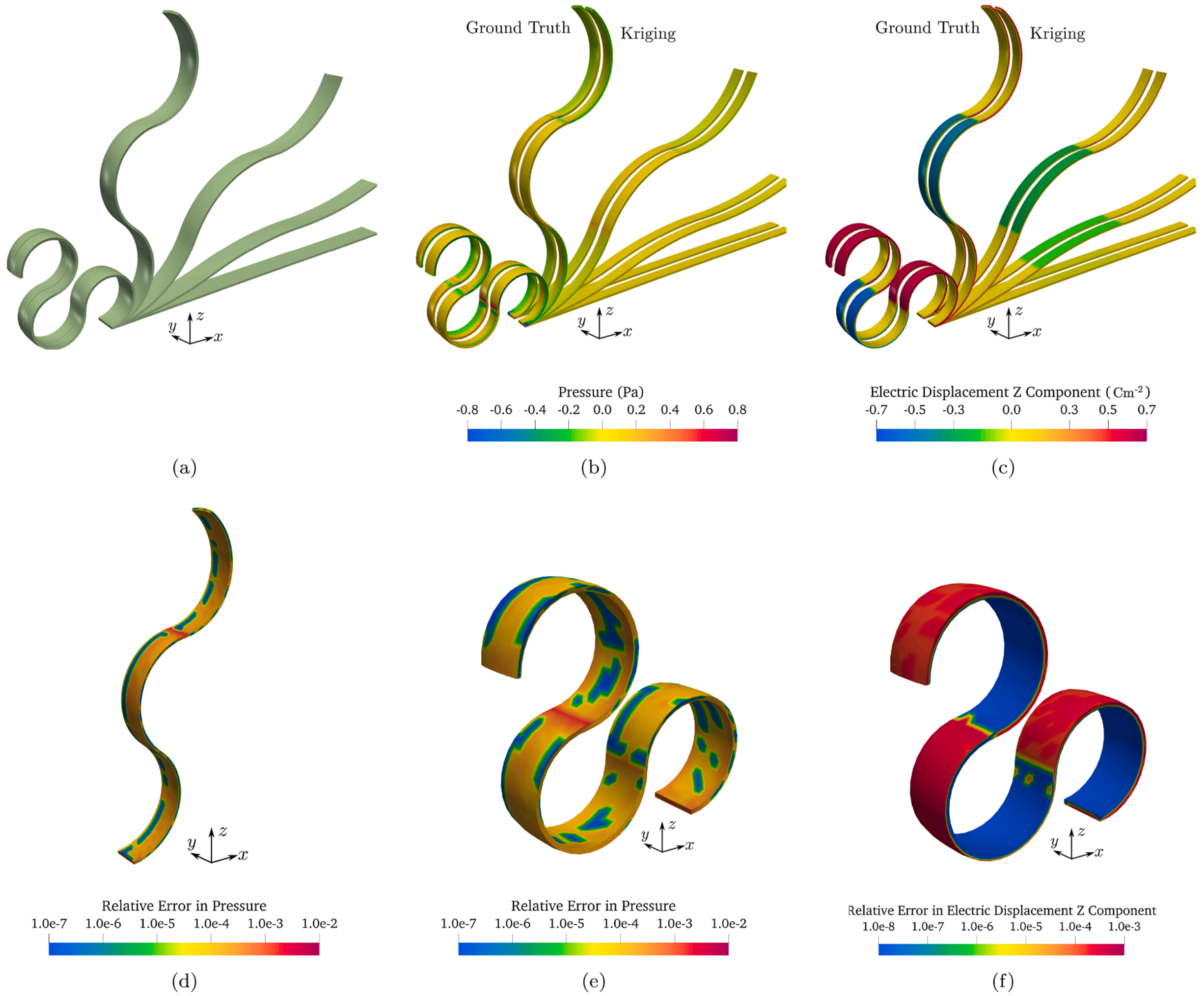

Fig. 18. Displays the progression of a bending actuator where (a) provides a side-by-side view of the ground truth (left) and Kriging (right) based models; (b) and (c) show the pressure and z-component of the electric displacement distributions, respectively; (d) and (e) presents the relative errors in pressure whilst (f) shows the relative error in electric displacement.

The slight deviation noticeable in the final most curled configuration provides an early indication of the extent of success achieved in this work. Fig. 18(b) and (c) compare the pressure and z-component of the electric displacement respectively. To see more clearly the extent of the closeness, Fig. 18(d)–(f) portray the relative errors in the quantities shown above for both the penultimate and final loading increments. The largest relative errors in pressure distribution are remarkably only $0.2\,\%$ in Fig. 18(d) to (e). This is even further improved when considering the relative error in electric displacement as shown in Fig. 18(f) which has a maximum error of only $0.04\,\%$.

6.2. Example 2 - transversely isotropic complex bending

The next example introduces complex bending with curling as a result of the materials anisotropy. The effective electrode placement forms the same configuration as the previous example, just with an applied electric potential of 3.0×10^{-3} (V) - see Fig. 17 - however, the resulting bending mode is vastly different as a result of the transversely isotropic material symmetry, with anisotropic direction $\boldsymbol{N} = [0.5774, 0.5774, 0.5774]^T$. For further details on the Ideal Dielectric Transversely Isotropic material model, the reader is directed to Appendix E.3.

Whilst the domain and electrode configurations are the same as the first example, the altered material renders a completely separate torsional deformation as can be seen in Fig. 19. Each load increment stage presented in Fig. 19(a) consists of the ground truth solution in purple overlaid with a slightly transparent Kriging metamodel solution. The impressive indistinguishability is reiterated across the range of relative error plots for the pressure fields and electric displacement fields in Fig. 19(d)–(f) respectively. Despite the fact the material is significantly more complex, the maximum errors demonstrated are equally small in pressure at $0.21\,\%$ and $0.25\,\%$ for

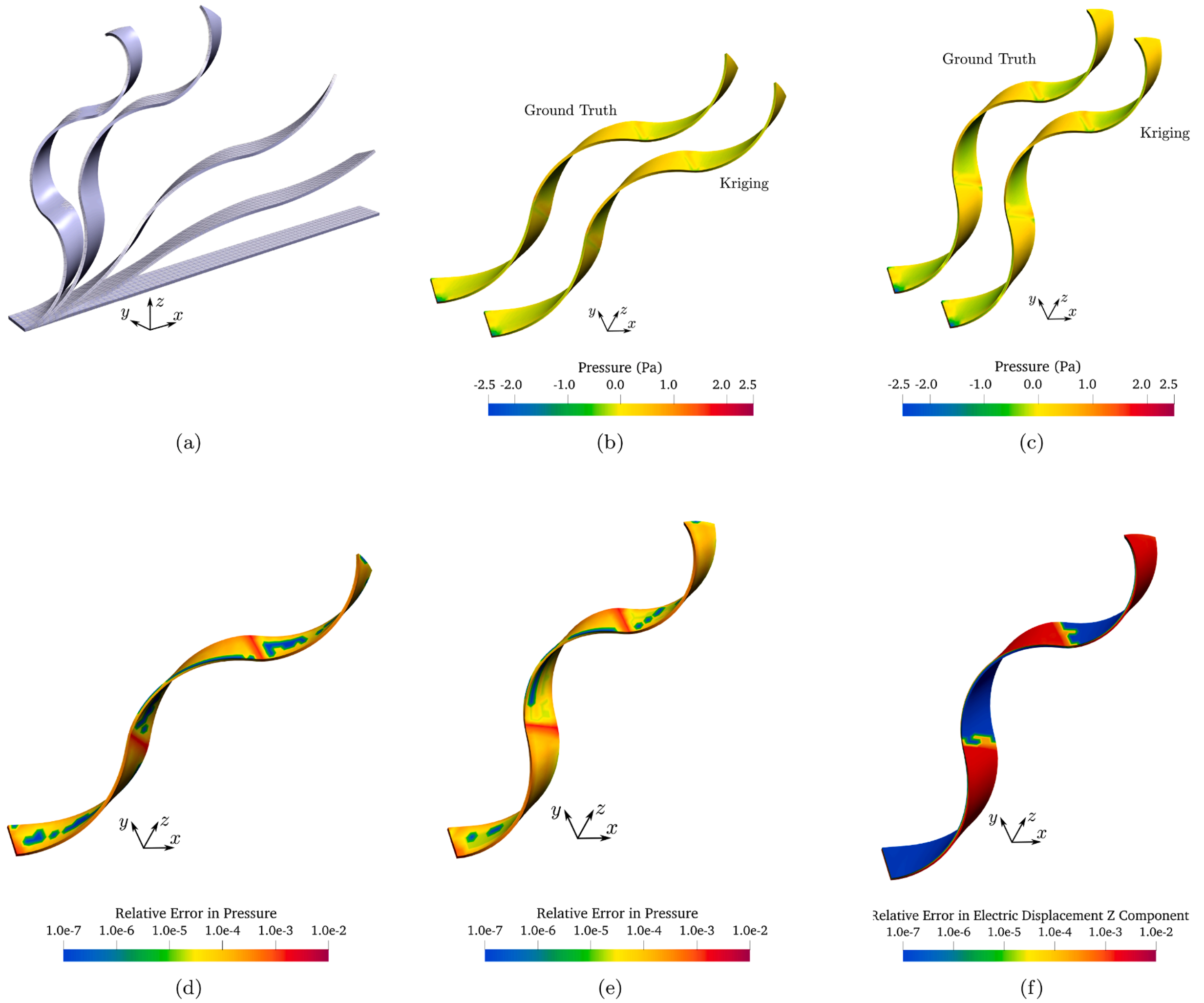

Fig. 19. Portrays the progression of an anisotropic bending actuator where (a) showcases the ground truth solution in purple overlaid with the Kriging solution in a transparent meshed view; (b) and (c) highlight the pressure distributions for two load increments of the twisted deformation whilst (d) and (e) display the corresponding relative errors in pressure; (f) demonstrates the relative error in the final load increment for the z-component of the electric displacement.(For interpretation of the references to color in this figure legend, the reader is referred to the web version of this article.)

Fig. 19(d) and (e) respectively. Fig. 19(f) highlights that modelling the electric displacement field is more challenging, but still has a very small maximum relative error of $0.2\,\%$.

6.3. Example 3 - transversely isotropic direction discovery

The following example is used to demonstrate the success of a Kriging developed constitutive model where the direction of anisotropy for a transversely isotropic material was not provided and has therefore been discovered using the process outlined in Section 3. For clarity, the random anisotropic direction is $\boldsymbol{N} = [0.44263, -0.8847, 0.1474]^T$ and for further details on the Ideal Dielectric Transversely Isotropic material model, the reader is directed to Appendix E.3. The numerical results presented in Fig. 20 were obtained using the configuration detailed previously in Fig. 17.

After identifying the anisotropic direction with an insignificant derivative reconstruction error of 3.22×10^{-6}, the 27 point dataset (22 after filtering and infill) was used to calibrate a metamodel and produce the solution as seen in Fig. 20. To emphasise the impeccable Kriging solution, Fig. 20(a) shows the Kriging solution laid over the ground truth solution with no visible separation between them. Providing quantitative results, Fig. 20(b) and (c) provide the distributions of pressure and the resulting relative errors respectively. The maximum relative error in pressure recorded for the final load increment was a mere $1.3\,\%$.

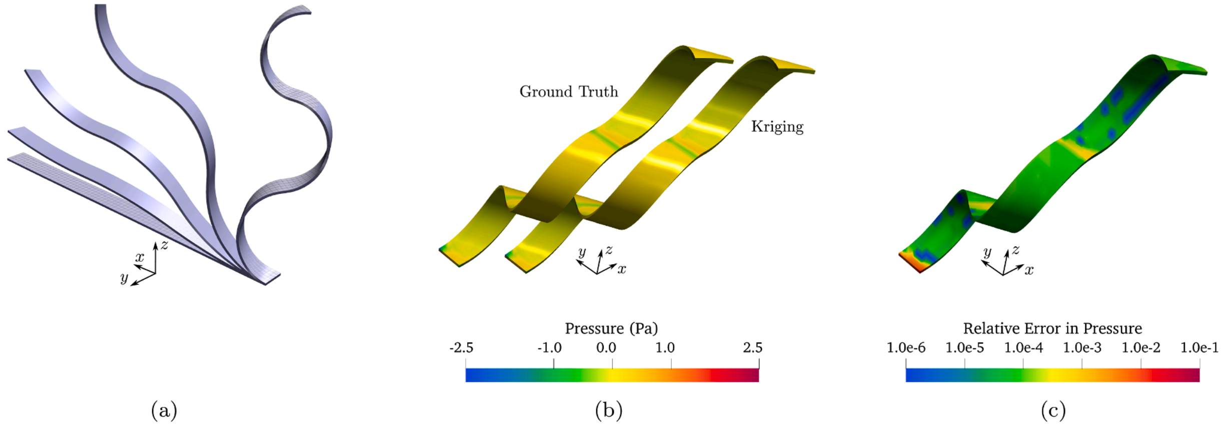

Fig. 20. Presents the progression of an anisotropic bending actuator where (a) displays the ground truth solution in purple overlaid with the Kriging solution in a transparent meshed view; (b) demonstrates the distribution in pressure across the actuator whilst (c) provides the relative error in pressure across the device.(For interpretation of the references to color in this figure legend, the reader is referred to the web version of this article.)

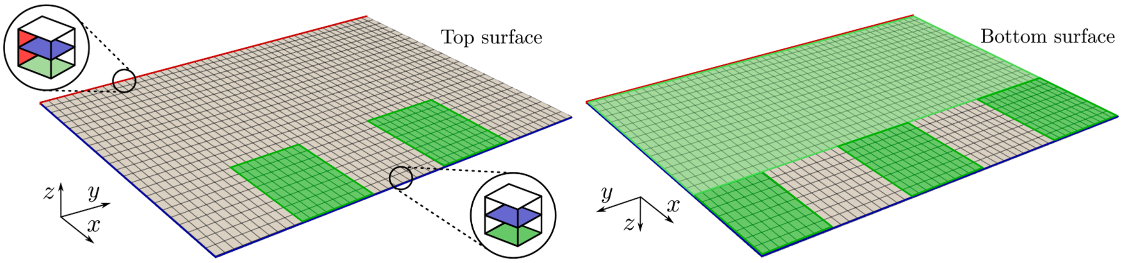

Fig. 21. Depicts the schematic of the $0.15 \times 0.2 \times 0.001(m)$ domain discretised into $\{24, 50, 2\}$ elements in the respective $\{x, y, z\} directions$ as well as the boundary conditions used for Example 4. The red region shows the fixed surface, whilst the blue line indicates the midway surface with an electric potential set to zero. There are two types of shaded green regions which showcase the surface where a non zero electric potential is prescribed. The darker green regions have a higher potential of 3.0×10^{-4} (V) compared to the large lighter shaded region which has an applied electric potential of 5.0×10^{-5} (V).(For interpretation of the references to color in this figure legend, the reader is referred to the web version of this article.)

6.4. *Example 4 - isotropic frilling*

The fourth example aims to showcase an isotropic material model which is principal stretch based by nature - i.e. the Ideal Dielectric Ogden model (see Appendix E.1 for details), with a configuration that enables a sophisticated deformation. Fig. 21 presents the configuration which comprises of a $0.15 \times 0.2 \times 0.001(m)$ domain discretised into $\{24, 50, 2\}$ elements in the respective $\{x, y, z\} directions$. Moreover, the positioning of the electrodes are demonstrated which will produce an inhomogeneous electric field leading to the combination of bending and frilling.

An intriguing solution is displayed in Fig. 22 whereby the configuration facilitates the slight bending from the low potential applied across the bottom layer as well as the frilling across the front of the device due to the upper and lower arrangements of the higher powered electrodes. Though hardly noticeable, Fig. 22(a) is split in two - the left half consisting of the ground truth solution whilst the right uses the Kriging metamodel. The perfect join indicates the success of the calibration and implementation and this is further evidenced by Fig. 22(b) with the overlaying of the two solutions. A comparison of the distributions in Cauchy stress σ_{12} component is provided in Fig. 22(c) alongside the relative error in pressure. Fig. 22(d) shows the low average relative error with maximum peaks lying at 0.75 %. To assess the accuracy in the electric displacement evaluated via Kriging the reader is referred to Fig. 22(e) and (f), which display the comparison in distribution of the z-component for the electric displacement as well as its relative error on the top and bottom side of the device. The maximum relative error yielded for the electric displacement was an insignificant 0.1 %.

6.5. *Example 5 - rank-one laminate wrinkling*

The penultimate example takes a thin - $0.6 \times 0.6 \times 0.01(m)$ - square plate which is fixed all along the boundaries (red region in Fig. 23). The domain is discretised into $\{40, 40, 2\}$ elements in the corresponding $\{x, y, z\}$ directions. An electric potential of zero is prescribed midway through (blue line in Fig. 23) and a potential of 5.0×10^{-3} (V) is applied across the upper surface - green region depicted in Fig. 23).

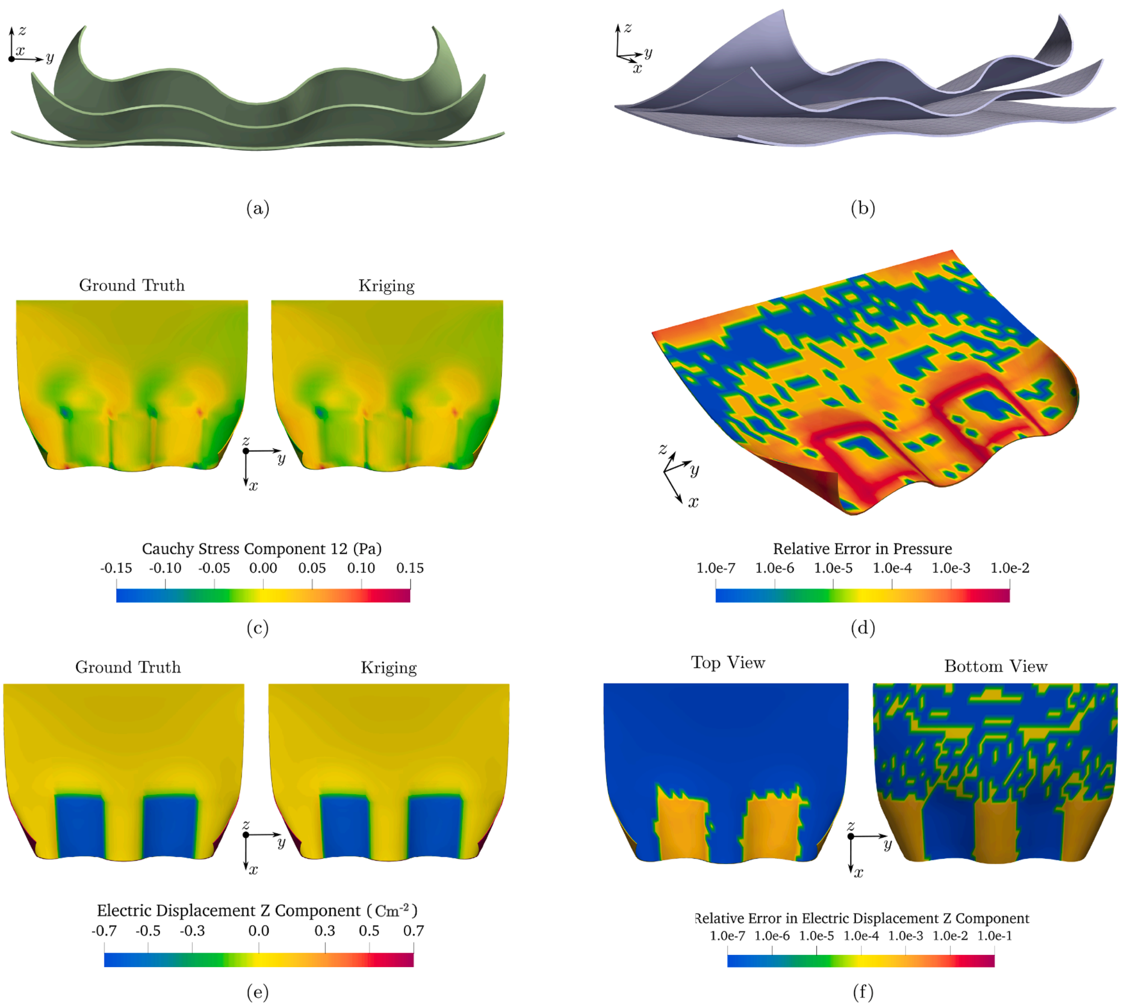

Fig. 22. Portrays the complex progression of a bending and frilling actuator induced due to an inhomogeneous applied electric potential. Subfigure (a) presents a side-by-side view of the ground truth and Kriging metamodel solutions and (b) shows an overlaid set of solutions where the ground truth is purple in appearance and Kriging a slightly transparent mesh; (c) presents the distribution in Cauchy stress - component 12 - and (d) the distribution in relative error of pressure; (e) and (f) show the z- component of the electric displacement and its relative error.

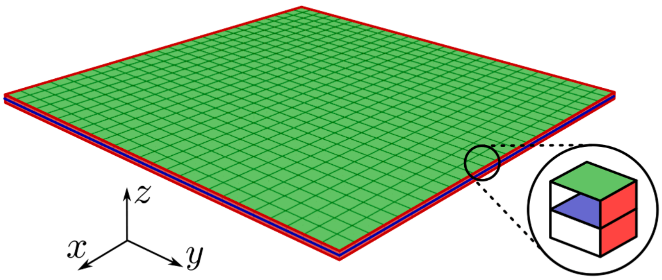

Fig. 23. Presents the schematic of the $0.6 \times 0.6 \times 0.01(m)$ domain as well as the boundary conditions used for Example 5. The red region shows the fixed surface, whilst the blue line indicates the midway surface with an electric potential set to zero. The green region showcases the surface where a potential of 5.0×10^{-3} (V) is prescribed. Note the domain is discretised into $\{40, 40, 2\}$ elements in the corresponding $\{x, y, z\}$ directions.(For interpretation of the references to color in this figure legend, the reader is referred to the web version of this article.)

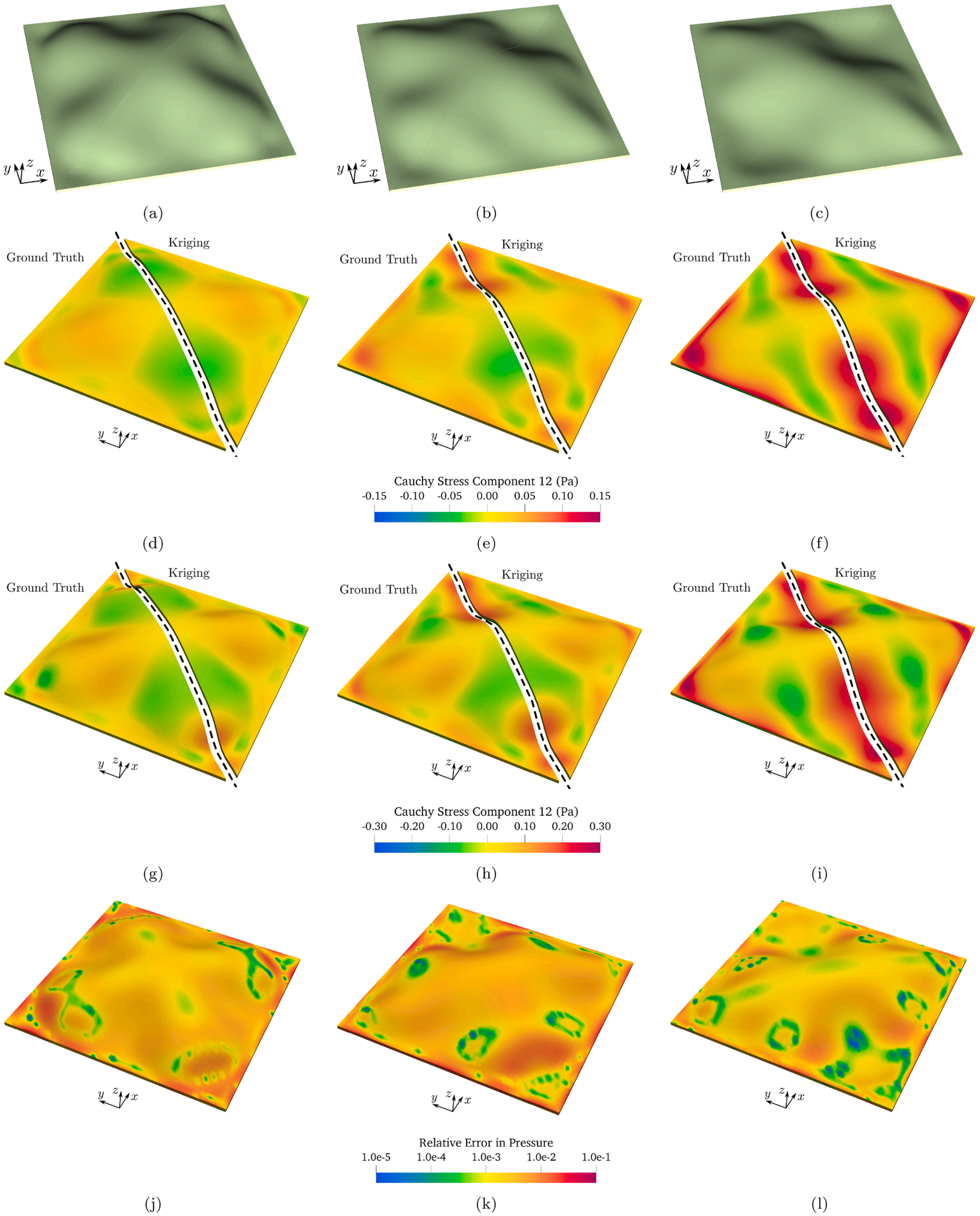

Fig. 24. Displays a range of plate buckling deformations where (a) - (c) demonstrate side-by-side views of the ground truth (left) and Kriging (right) solutions for the three rank-one laminate setups distinguishable by column as $\{f_m = 2, f_e = 2\}$; $\{f_m = 5, f_e = 3\}$; $\{f_m = 10, f_e = 5\}$ respectively; (d) - (f) show the stress distribution for the 0.75 load increment whilst (g) - (i) shows the final 1.00 load increment. The relative errors in pressure are then presented in (j) - (l).

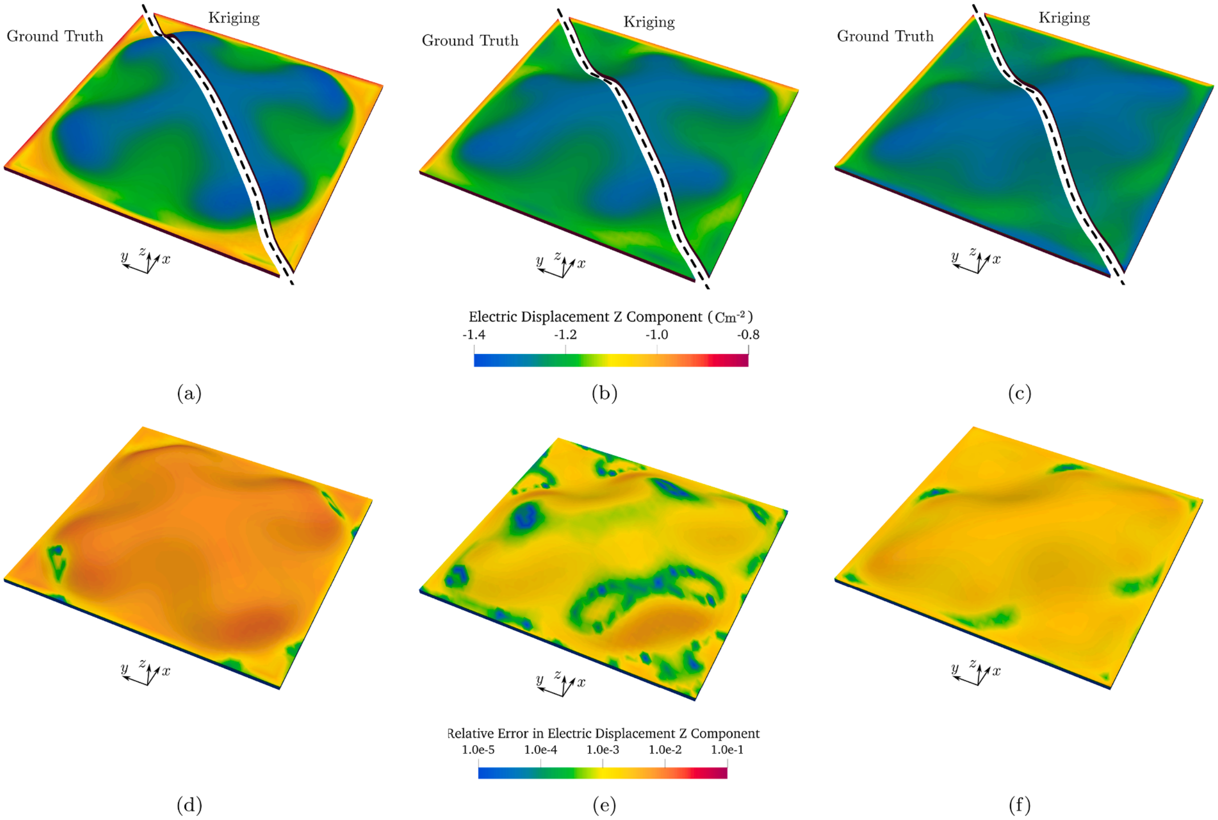

Fig. 25. Depicts the electrostatic quantities associated with the plate buckling configurations where (a) - (c) demonstrate the distribution of the z-component of the electric displacement, whilst (d) - (f) highlights the relative errors in the same electric displacement quantity.

When defining a rank-one laminate material the mechanical contrast f_m and electrical contrast f_e, i.e. the ratio between mechanical and electrical material parameters, play a critical role. The response of the material under the same loading conditions can vary significantly as a result of these simple parameters - as can be witnessed across Fig. 24. The three columns of Fig. 24 distinguish three different rank-one laminates with contrasts as follows: $\{f_m = 2, f_e = 2\}$; $\{f_m = 5, f_e = 3\}$; $\{f_m = 10, f_e = 5\}$, and the full details for the Ideal Dielectric Rank-one Laminate material models can be found in Appendix E.4. The differing responses can be clearly seen in Fig. 24(a)–(c) where the deformation goes from being relatively symmetric in different directions - due to the weaker contrasts - to clearly symmetric in one direction. These figures additionally, provide the side-by-side view, where the ground truth solutions (left) have been stitched with the Kriging solutions (right) for the final load increment.

Fig. 24(d)–(f) show the distribution for the 12-component of the Cauchy stress tensor. The emerging patterns are very similar between the ground truth and Kriging solutions for the $\{f_m = 2, f_e = 2\}$ and $\{f_m = 10, f_e = 5\}$, however a small difference in magnitudes can be seen in the $\{f_m = 5, f_e = 3\}$ setup. Whilst this is the case for the 0.75 load increment case, it can be seen that by the fully applied load case in Fig. 24(h) the discrepancy between the two solutions has resolved. To affirm, Fig. 24(g)–(i) showcase the stress component for the fully applied electric potential - which across the board showcase a very strong replication in distributions from the Kriging solutions. Underneath, Fig. 24(j)–(l) finally show the relative errors in pressure for the three rank-one laminate solutions. The $\{f_m = 5, f_e = 3\}$ setup appeared most challenging yielding maximum relative error of 3.6 %, whilst the others revealed maximum errors of 3 % and 2 % respectively.

To provide information on the electrostatic solutions, Fig. 25 showcases a series of results. Fig. 25(a)–(c) display the z-component of the electric displacement vector which appears to more clearly demonstrate the variations in deformations between the rank-one laminate setups. Note that each column represents the same setup as Fig. 24. Interestingly, a higher value for electric displacement seems to have formed on the buckled regions of the plate which is well captured by the Kriging solutions. The relative errors in Fig. 25(d)–(f) seem to indicate a more challenging result for Kriging, whereby the average relative errors appear larger. However, it is important to note the challenging nature of capturing a buckling pattern which is often associated with tougher numerical problems. The maximum relative error values are still reasonable at 1 % and 0.4 % for each respective setup.

6.6. Example 6 - RVE bending beam

To finish the numerical examples, the RVE metamodels demonstrated in Section 5.5.1 are being employed in a 3D FEM simulation. This example will showcase the capability to utilise multiple metamodels in a single simulation by assigning two different regions of

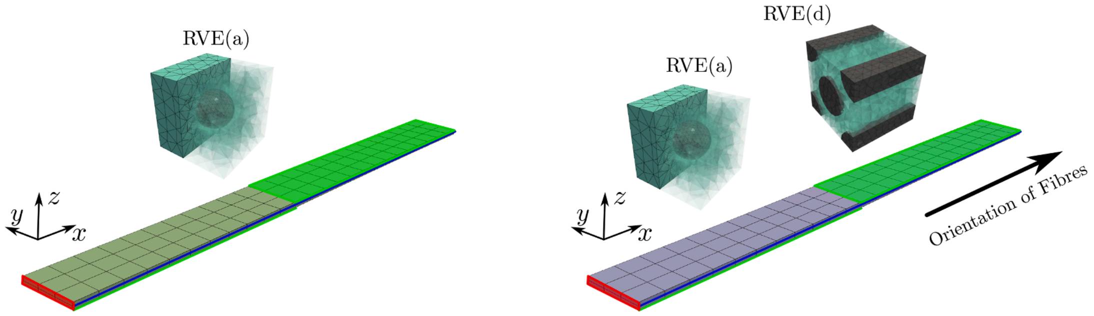

(a) Domain formed of RVE(a) only

(b) Domain split into half RVE(a) and RVE(d)

Fig. 26. Presents the schematics of the $1.0 \times 0.1 \times 0.01 (m)$ domain as well as the boundary conditions used for Example 6. The red region shows the fixed surface, whilst the blue line indicates the midway surface with an electric potential set to zero. The green region showcases the surface where a potential of 2.6×10^{-3} (V) is prescribed. Note the domain is discretised into $\{25, 3, 2\}$ elements in the corresponding $\{x, y, z\}$ directions.(For interpretation of the references to color in this figure legend, the reader is referred to the web version of this article.)

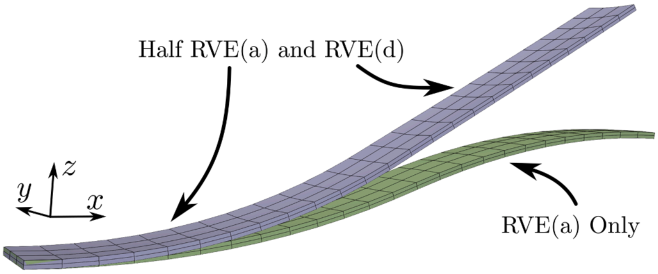

Fig. 27. Displays the deformations achieved for the two examples, the green domain consisting of only RVE(a) and the purple domain consisting of a domain split in half using both RVE(a) and RVE(d) - see Appendix E.5 for RVE details.(For interpretation of the references to color in this figure legend, the reader is referred to the web version of this article.)

the domain their own constitutive metamodel. Once again a bending configuration is being utilised and details for the domain and boundary conditions can be found for both examples in Fig. 26.

An electric potential of $2.6 \times 10^{-3} (V)$ is applied to the electrode configurations and the resulting deformations can be seen in Fig. 27. Firstly, notice the green domain which bends in two directions as expected from the configuration described in Fig. 26. The green domain consists of a single material metamodel calibrated on data from RVE(a) - see Appendix E.5 for more details on the RVE. On the other hand, the purple domain consists of two material models, the first half for RVE(a) and the second for RVE(d). The critical aspect to consider, is that RVE(d) consists of stiff fibres which are aligned parallel to the length of the device. As a result, the bending can be seen to be resisted by the stiffer fibres and cannot be overcome, leading to the second half of the domain remaining straight whilst the first half bends. Furthermore, whilst resisting bending it can also be seen that some curling occurs which again is an artefact associated with simulating a soft matrix with stiff fibres.

7. Concluding remarks

The first element of this work highlighted the process to formulate the electromechanical problem in terms of principal stretches for the isotropic mechanics and invariants for the anisotropic mechanics and the coupling of the physics. This has been further extended to the required adjustments to be able to utilise this method with the outlined ML approach. The second focus outlined a procedure for obtaining derivative contributions for each ML input variable via orthogonal projections. The use of linear algebra enables the contributions to be evaluated which are critical when employing the Gradient Enhanced Kriging approach. Furthermore it enables a hierarchical procedure to be used to discover the anisotropic material symmetry group for the respective dataset. This is vital for the application of a ML approach to constitutive metamodelling since the advantages lie within the capability for ML to be employed on a dataset from an unknown material or material with a complex microstructure resulting in a complex constitutive model formulation. Furthermore, the challenges of handling a dataset without a known underlying model - such as the RVEs - have been highlighted which include needing to see which input sets can sufficiently recover the known quantities. The third objective achieved showcased an extensive set of constitutive models which have been successfully captured through the ML procedure and integrated within the Finite Element framework to model a set of complex numerical examples which highlight that constitutive metamodels can perform as well as their analytical counterparts. The final numerical example also presented the use of multiple constitutive metamodels employed during a single simulation for select regions of a domain.

CRediT authorship contribution statement

Nathan Ellmer: Writing – review & editing, Writing – original draft, Visualization, Validation, Software, Methodology, Investigation, Data curation, Conceptualization; **Rogelio Ortigosa:** Writing – review & editing, Supervision, Software, Methodology, Investigation, Funding acquisition, Formal analysis, Conceptualization; **Jesús Martínez-Frutos:** Writing – review & editing, Visualization, Software, Methodology, Investigation; **Roman Poya:** Writing – review & editing, Resources, Methodology; **Johann Sienz:** Writing – review & editing, Methodology; **Antonio J. Gil:** Writing – review & editing, Supervision, Project administration, Methodology, Funding acquisition, Formal analysis, Conceptualization.

Data availability

Data will be made available on request.

Declaration of competing interest

The authors declare the following financial interests/personal relationships which may be considered as potential competing interests: Antonio J. Gil reports financial support was provided by Defence Science and Technology Laboratory. Antonio J. Gil reports financial support was provided by Leverhulme Trust. Rogelio Ortigosa, Jesus Martinez Frutos reports financial support was provided by Spain Ministry of Science and Innovation. If there are other authors, they declare that they have no known competing financial interests or personal relationships that could have appeared to influence the work reported in this paper.

Acknowledgements

N. Ellmer and A. J. Gil wish to acknowledge the financial support provided by the Defence, science and technology laboratory (Dstl). Additionally, A. J. Gil acknowledges the support of The Luverhulme Trust through a Leverhulme Fellowship. R. Ortigosa and J. Martínez-Frutos acknowledge the support of grant PID2022-141957OA-C22 funded by MICIU/AEI/10.13039/501100011033 and by “RDF A way of making Europe”.

Appendix A. Partial derivatives of internal energy

A.1. Isotropic contribution

The first derivatives are given by

$$\begin{aligned} &\partial_{\boldsymbol{F}}\lambda_1 = \boldsymbol{n}_1^P \otimes \boldsymbol{N}_1^P, &&\partial_{\boldsymbol{F}}\lambda_2 = \boldsymbol{n}_2^P \otimes \boldsymbol{N}_2^P, &&\partial_{\boldsymbol{F}}\lambda_3 = \boldsymbol{n}_3^P \otimes \boldsymbol{N}_3^P, \\ &\partial_{\boldsymbol{D}_0}\lambda_1 = \boldsymbol{0}, &&\partial_{\boldsymbol{D}_0}\lambda_2 = \boldsymbol{0}, &&\partial_{\boldsymbol{D}_0}\lambda_3 = \boldsymbol{0}, \end{aligned} \tag{A.1}$$

where $\boldsymbol{n}_i^P$ corresponds to the columns of $\hat{\boldsymbol{U}}$ and $\boldsymbol{N}_i^P$ corresponds to the columns of $\hat{\boldsymbol{V}}$, where the superscript “P” distinguishes between principal directions ($\boldsymbol{n}^P$, $\boldsymbol{N}^P$) and anisotropic directions ($\boldsymbol{N}$). For the invariants the definitions are given by

$$\begin{aligned} &\partial_{\boldsymbol{F}} I_4 = \boldsymbol{0}, &&\partial_{\boldsymbol{F}} I_5 = 2\boldsymbol{F}\boldsymbol{D}_0 \otimes \boldsymbol{D}_0, \\ &\partial_{\boldsymbol{D}_0} I_4 = 2\boldsymbol{D}_0, &&\partial_{\boldsymbol{D}_0} I_5 = 2\boldsymbol{C}\boldsymbol{D}_0, \end{aligned} \tag{A.2}$$

where $\boldsymbol{C}$ is the right Cauchy-Green strain tensor ($\boldsymbol{F}^T\boldsymbol{F}$). The second derivatives for the principal stretches are more complicated and through ingredients given by Smith et al. [43], Poya et al. [39] states that these second partial derivatives can be expressed as

$$\sum_{i=1}^{3}\left(\partial_{\lambda_i} U\right)\partial^2_{\boldsymbol{F}\boldsymbol{F}}\lambda_i = \sum_{i=1}^{3}\bar{\lambda}_i \boldsymbol{L}_i \otimes \boldsymbol{L}_i + \bar{\lambda}_{i+3}\boldsymbol{T}_i \otimes \boldsymbol{T}_i, \tag{A.3}$$

with

$$\begin{aligned} &\bar{\lambda}_1 = \frac{\partial_{\lambda_2}U - \partial_{\lambda_3}U}{\lambda_2 - \lambda_3}, &&\bar{\lambda}_2 = \frac{\partial_{\lambda_1}U - \partial_{\lambda_3}U}{\lambda_1 - \lambda_3}, &&\bar{\lambda}_3 = \frac{\partial_{\lambda_1}U - \partial_{\lambda_2}U}{\lambda_1 - \lambda_2}, \\ &\bar{\lambda}_4 = \frac{\partial_{\lambda_2}U + \partial_{\lambda_3}U}{\lambda_2 + \lambda_3}, &&\bar{\lambda}_5 = \frac{\partial_{\lambda_1}U + \partial_{\lambda_3}U}{\lambda_1 + \lambda_3}, &&\bar{\lambda}_6 = \frac{\partial_{\lambda_1}U + \partial_{\lambda_2}U}{\lambda_1 + \lambda_2}, \end{aligned} \tag{A.4}$$

and where $\boldsymbol{T}_i$ and $\boldsymbol{L}_i$ refer to the twist and flip tensors respectively, defined as

$$\begin{aligned} &\boldsymbol{L}_1 = \frac{1}{\sqrt{2}}\hat{\boldsymbol{U}}\begin{bmatrix} 0 & 0 & 0 \\ 0 & 0 & 1 \\ 0 & 1 & 0 \end{bmatrix}\boldsymbol{V}^T, &&\boldsymbol{L}_2 = \frac{1}{\sqrt{2}}\hat{\boldsymbol{U}}\begin{bmatrix} 0 & 0 & 1 \\ 0 & 0 & 0 \\ 1 & 0 & 0 \end{bmatrix}\boldsymbol{V}^T, &&\boldsymbol{L}_3 = \frac{1}{\sqrt{2}}\hat{\boldsymbol{U}}\begin{bmatrix} 0 & 1 & 0 \\ 1 & 0 & 0 \\ 0 & 0 & 0 \end{bmatrix}\boldsymbol{V}^T, \\ &\boldsymbol{T}_1 = \frac{1}{\sqrt{2}}\hat{\boldsymbol{U}}\begin{bmatrix} 0 & 0 & 0 \\ 0 & 0 & -1 \\ 0 & 1 & 0 \end{bmatrix}\boldsymbol{V}^T, &&\boldsymbol{T}_2 = \frac{1}{\sqrt{2}}\hat{\boldsymbol{U}}\begin{bmatrix} 0 & 0 & -1 \\ 0 & 0 & 0 \\ 1 & 0 & 0 \end{bmatrix}\boldsymbol{V}^T, &&\boldsymbol{T}_3 = \frac{1}{\sqrt{2}}\hat{\boldsymbol{U}}\begin{bmatrix} 0 & -1 & 0 \\ 1 & 0 & 0 \\ 0 & 0 & 0 \end{bmatrix}\boldsymbol{V}^T. \end{aligned} \tag{A.5}$$

The remaining partial derivatives are given as

A.2. Anisotropic contribution (transverse isotropy)

$$\begin{aligned} &\partial_{\boldsymbol{F}} I_6 = 2\boldsymbol{F}\boldsymbol{N}\otimes\boldsymbol{N}, && \partial_{\boldsymbol{F}} I_7 = 2(\boldsymbol{H}\boldsymbol{N}\otimes\boldsymbol{N})\times\boldsymbol{F}, && \partial_{\boldsymbol{F}} I_8 = \boldsymbol{0},\\ &\partial_{\boldsymbol{D}_0} I_6 = \boldsymbol{0}, && \partial_{\boldsymbol{D}_0} I_7 = \boldsymbol{0}, && \partial_{\boldsymbol{D}_0} I_8 = 2\left(\boldsymbol{D}_0\cdot\boldsymbol{N}\right)\boldsymbol{N}. \end{aligned} \tag{A.6}$$

A.3. Anisotropic contribution (orthotropy)

$$\begin{aligned} &\partial_{\boldsymbol{F}} I_6 = 2\boldsymbol{F}\boldsymbol{N}_1\otimes\boldsymbol{N}_1, && \partial_{\boldsymbol{F}} I_7 = 2\left(\boldsymbol{H}\boldsymbol{N}_1\otimes\boldsymbol{N}_1\right)\times\boldsymbol{F}, && \partial_{\boldsymbol{F}} I_8 = 2\boldsymbol{F}\boldsymbol{N}_2\otimes\boldsymbol{N}_2,\\ &\partial_{\boldsymbol{D}_0} I_6 = \boldsymbol{0}, && \partial_{\boldsymbol{D}_0} I_7 = \boldsymbol{0}, && \partial_{\boldsymbol{D}_0} I_8 = \boldsymbol{0},\\ &\partial_{\boldsymbol{F}} I_9 = \boldsymbol{0}, && \partial_{\boldsymbol{F}} I_{10} = \boldsymbol{0}, && \\ &\partial_{\boldsymbol{D}_0} I_9 = 2\left(\boldsymbol{D}_0\cdot\boldsymbol{N}_1\right)\boldsymbol{N}_1, && \partial_{\boldsymbol{D}_0} I_{10} = 2\left(\boldsymbol{D}_0\cdot\boldsymbol{N}_2\right)\boldsymbol{N}_2, && \end{aligned} \tag{A.7}$$

Appendix B. Rank-one laminate homogenisation details

The projection operator $\mathcal{T}_{\boldsymbol{N}} \in \mathbb{R}^{3\times 2}$ given in Fig. 3 is used to project onto the plane normal to the unit vector $\boldsymbol{N}$ defined by

$$\mathcal{T}_{\boldsymbol{N}} = \boldsymbol{T}_1\otimes\boldsymbol{E}_1 + \boldsymbol{T}_2\otimes\boldsymbol{E}_2, \tag{B.1}$$

where $\boldsymbol{T}_1$ and $\boldsymbol{T}_2$ are two linearly independent vectors contained within the plane of lamination and vectors $\boldsymbol{E}_1$ and $\boldsymbol{E}_2$ are $[1,0]^T$ and $[0,1]^T$ respectively [9].

Appendix C. GPR additional info

The objective of this Appendix is to provide fully the definitions of the derivatives for the correlation matrix $\boldsymbol{R}$ as seen in (44b) and (44c), and the derivatives of the cross-correlation matrix as seen in (58a) and (58b). Whilst this appears trivial, careful consideration must be taken when considering the hybrid principle stretches and invariants approach.

C.1. Correlation matrix

For the correlation matrix $\boldsymbol{R}$, the hybrid approach yields two first derivatives, the first of which is the derivative of the unchanged correlation function $\mathcal{R}\left(\mathbf{I}^{(i)},\mathbf{I}^{(j)},\boldsymbol{\theta}\right)$ in terms of the input invariants given by

$$\partial_{\mathrm{I}_k^{(j)}}\mathcal{R} = 2\theta_k\left(\mathrm{I}_k^{(i)} - \mathrm{I}_k^{(j)}\right)\mathcal{R}\left(\mathbf{I}^{(i)},\mathbf{I}^{(j)},\boldsymbol{\theta}\right). \tag{C.1}$$

For the isotropic invariants $\{I_1, I_2, I_3\}$ which are functions of the principle stretches $\boldsymbol{\lambda}$, an adjusted correlation function denoted by $\tilde{\mathcal{R}}\left(\mathbf{I}\left(\boldsymbol{\lambda}^{(i)}\right),\mathbf{I}\left(\boldsymbol{\lambda}^{(j)}\right),\boldsymbol{\theta}\right)$ which requires the use of the chain rule via

$$\partial_{\lambda_m^{(j)}}\mathcal{R} = \sum_{k=1}^{3}\left(\partial_{\mathrm{I}_k^{(j)}}\tilde{\mathcal{R}}\right)\partial_{\lambda_m^{(j)}}\mathrm{I}_k^{(j)}. \tag{C.2}$$

With regards to the second derivatives required for (44c), there are four possible combinations within this hybrid approach

$$\begin{aligned} \partial^2_{\mathrm{I}_l^{(i)}\mathrm{I}_k^{(j)}}\mathcal{R} &= 2\theta_k\left[\delta_{kl} - 2\theta_l\left(\mathrm{I}_k^{(i)} - \mathrm{I}_k^{(j)}\right)\left(\mathrm{I}_l^{(i)} - \mathrm{I}_l^{(j)}\right)\right]\mathcal{R}\left(\mathbf{I}^{(i)},\mathbf{I}^{(j)},\boldsymbol{\theta}\right),\\ \partial^2_{\lambda_n^{(i)}\lambda_m^{(j)}}\mathcal{R} &= \sum_{k,l=1}^{3}\partial_{\lambda_n^{(i)}}\mathrm{I}_l^{(i)}\left(\partial^2_{\mathrm{I}_l^{(i)}\mathrm{I}_k^{(j)}}\tilde{\mathcal{R}}\right)\partial_{\lambda_m^{(j)}}\mathrm{I}_k^{(j)} + \delta_{ij}\left[\sum_{k=1}^{3}\left(\partial^2_{\lambda_n^{(i)}\lambda_m^{(j)}}\mathrm{I}_k^{(j)}\right)\partial_{\mathrm{I}_k^{(j)}}\tilde{\mathcal{R}}\right],\\ \partial^2_{\lambda_n^{(i)}\mathrm{I}_k^{(j)}}\mathcal{R} &= \sum_{l=1}^{3}\partial_{\lambda_n^{(i)}}\mathrm{I}_l^{(i)}\left(\partial^2_{\mathrm{I}_l^{(i)}\mathrm{I}_k^{(j)}}\tilde{\mathcal{R}}\right),\\ \partial^2_{\mathrm{I}_l^{(i)}\lambda_m^{(j)}}\mathcal{R} &= \sum_{k=1}^{3}\left(\partial^2_{\mathrm{I}_l^{(i)}\mathrm{I}_k^{(j)}}\tilde{\mathcal{R}}\right)\partial_{\lambda_m^{(j)}}\mathrm{I}_k^{(j)}. \end{aligned} \tag{C.3}$$

C.2. Cross-correlation matrix

For the definition of the cross-correlation matrix $\boldsymbol{r}$ in (52), only the correlation function and the first derivatives are required leading to the same expressions given in (C.1) and (C.2). Taking the first derivative of the $\boldsymbol{q}_1$ block of $\boldsymbol{r}$ with respect to the ith evaluation point (needed for (58a)) has two components again given by

$$\begin{aligned} \partial_{\mathrm{I}_k^{\bullet(i)}} \mathcal{R} &= -2\theta_k \left(\mathrm{I}_k^{\bullet(i)} - \mathrm{I}_k^{(j)} \right) \mathcal{R}\left(\mathbf{I}^{\bullet(i)}, \mathbf{I}^{(j)}, \boldsymbol{\theta}^* \right), \\ \partial_{\lambda_m^{\bullet(i)}} \mathcal{R} &= \sum_{k=1}^{3} \left(\partial_{\mathrm{I}_k^{\bullet(i)}} \tilde{\mathcal{R}} \right) \partial_{\lambda_m^{\bullet(i)}} \mathrm{I}_k^{\bullet(i)}. \end{aligned} \tag{C.4}$$

Taking the first derivative of the $\boldsymbol{q}_2$ block of $\boldsymbol{r}$ given in (58b) yields

$$\begin{aligned} \partial^2_{\mathrm{I}_l^{\bullet(i)} \mathrm{I}_k^{(j)}} \mathcal{R} &= 2\theta_k \left[\delta_{kl} - 2\theta_l \left(\mathrm{I}_k^{\bullet(i)} - \mathrm{I}_k^{(j)} \right) \left(\mathrm{I}_l^{\bullet(i)} - \mathrm{I}_l^{(j)} \right) \right] \mathcal{R}\left(\mathbf{I}^{\bullet(i)}, \mathbf{I}^{(j)}, \boldsymbol{\theta} \right), \\ \partial^2_{\lambda_n^{\bullet(i)} \lambda_m^{(j)}} \mathcal{R} &= \sum_{k,l=1}^{3} \partial_{\lambda_n^{\bullet(i)}} \mathrm{I}_l^{\bullet(i)} \left(\partial^2_{\mathrm{I}_l^{\bullet(i)} \mathrm{I}_k^{(j)}} \tilde{\mathcal{R}} \right) \partial_{\lambda_m^{(j)}} \mathrm{I}_k^{(j)}, \\ \partial^2_{\lambda_n^{\bullet(i)} \mathrm{I}_k^{(j)}} \mathcal{R} &= \sum_{l=1}^{3} \partial_{\lambda_n^{\bullet(i)}} \mathrm{I}_l^{\bullet(i)} \left(\partial^2_{\mathrm{I}_l^{\bullet(i)} \mathrm{I}_k^{(j)}} \tilde{\mathcal{R}} \right), \\ \partial^2_{\mathrm{I}_l^{\bullet(i)} \lambda_m^{(j)}} \mathcal{R} &= \sum_{k=1}^{3} \left(\partial^2_{\mathrm{I}_l^{\bullet(i)} \mathrm{I}_k^{(j)}} \tilde{\mathcal{R}} \right) \partial_{\lambda_m^{(j)}} \mathrm{I}_k^{(j)}. \end{aligned} \tag{C.5}$$

Appendix D. Metamodel synthetic data generation

The extended spherical parametrisation in $\mathbb{R}^5$ for use in evaluating the deviatoric directions in Algorithm 2 is given by

$$\boldsymbol{X}_{\boldsymbol{F}}^i = \begin{bmatrix} \cos\phi_1^i \\ \sin\phi_1^i \cos\phi_2^i \\ \sin\phi_1^i \sin\phi_2^i \cos\phi_3^i \\ \sin\phi_1^i \sin\phi_2^i \sin\phi_3^i \cos\phi_4^i \\ \sin\phi_1^i \sin\phi_2^i \sin\phi_3^i \sin\phi_4^i \end{bmatrix}, \qquad i \in \left[1, \ldots, n_{\boldsymbol{X}_{\boldsymbol{F}}}\right]. \tag{D.1}$$

The basis for the symmetric and traceless second order tensors used for the construction of $\boldsymbol{F}$ in Algorithm 3 are given as

$$\boldsymbol{\Psi}_1 = \sqrt{\frac{1}{6}} \begin{bmatrix} 2 & 0 & 0 \\ 0 & -1 & 0 \\ 0 & 0 & -1 \end{bmatrix}, \qquad \boldsymbol{\Psi}_2 = \sqrt{\frac{1}{2}} \begin{bmatrix} 0 & 0 & 0 \\ 0 & 1 & 0 \\ 0 & 0 & -1 \end{bmatrix}, \qquad \boldsymbol{\Psi}_3 = \sqrt{\frac{1}{2}} \begin{bmatrix} 0 & 1 & 0 \\ 1 & 0 & 0 \\ 0 & 0 & 0 \end{bmatrix}, \tag{D.2}$$

$$\boldsymbol{\Psi}_4 = \sqrt{\frac{1}{2}} \begin{bmatrix} 0 & 0 & 1 \\ 0 & 0 & 0 \\ 1 & 0 & 0 \end{bmatrix}, \qquad \boldsymbol{\Psi}_5 = \sqrt{\frac{1}{2}} \begin{bmatrix} 0 & 0 & 0 \\ 0 & 0 & 1 \\ 0 & 1 & 0 \end{bmatrix}. \tag{D.3}$$

Appendix E. Constitutive model details

The extensive range of constitutive models used throughout this work are outlined in the following subsections. Note that often these models are defined in terms of the isotropic mechanical invariants $\{I_1, I_2, I_3\}$ which are defined as

$$I_1 = \boldsymbol{F} : \boldsymbol{F}, \qquad I_2 = \boldsymbol{H} : \boldsymbol{H}, \qquad I_3 = \det \boldsymbol{F}. \tag{E.1}$$

The material parameters for the selected constitutive models are not necessarily representative of electroactive polymer materials. It is important to note that the deformations still reflect the true performance, but the resulting information and applied electric potential is scaled, namely $V_{scaled} = V\sqrt{\epsilon/\mu_1}$. This has been covered comprehensively in previous work, see Remark 6 in Section 5 of [53].

E.1. Ogden ideal dielectric

The definition for the Ogden Ideal Dielectric strain energy density is given by

$$U\left(\lambda_1, \lambda_2, \lambda_3, I_3, I_5\right) = \sum_{p=1}^{N} \frac{\mu_p}{\alpha_p} \left(\lambda_1^{\alpha_p} + \lambda_2^{\alpha_p} + \lambda_3^{\alpha_p} - 3 \right) - \mu_p \ln\left(\lambda_1 \lambda_2 \lambda_3\right) + \frac{\bar{\lambda}_p}{2} \left(\lambda_1 \lambda_2 \lambda_3 - 1\right)^2 + \frac{1}{2\epsilon} \frac{I_5}{I_3}, \tag{E.2}$$

where the material parameters are given in Table E.1.

E.2. Mooney-Rivlin ideal dielectric

The definition for the Mooney-Rivlin Ideal Dielectric strain energy density is given by

$$U\left(I_1, I_2, I_3, I_5\right) = \frac{\mu_1}{2}\left(I_1 - 3\right) + \frac{\mu_2}{2}\left(I_2 - 3\right) - \left(\mu_1 + 2\mu_2\right)\ln\left(I_3\right) + \frac{\lambda}{2}\left(I_3 - 1\right)^2 + \frac{1}{2\epsilon}\frac{I_5}{I_3}, \tag{E.3}$$

where the material parameters are given in Table E.2.

Table E.1
Material parameters used for the Ogden ideal dielectric.

Parameter:	$\{\mu_1, \mu_2, \mu_3\}$	α_1	α_2	α_3	$\{\bar{\lambda}_1, \bar{\lambda}_2, \bar{\lambda}_3\}$	ϵ
Value:	0.5	1	3.5	5	5	1

Table E.2
Material parameters used with the Mooney-Rivlin model.

Parameter:	μ_1	μ_2	λ	ϵ
Value:	0.5	0.5	5	1

E.3. *Transversely isotropic ideal dielectric*

The definition for the Transversely Isotropic Ideal Dielectric strain energy density is given by

$$\begin{aligned} U(I_1, I_2, I_3, I_4, I_5, I_6, I_7) = {} & \frac{\mu_1}{2}(I_1 - 3) + \frac{\mu_2}{2}(I_2 - 3) - (\mu_1 + 2\mu_2 + \mu_3)\ln(I_3) \\ & + \frac{\lambda}{2}(I_3 - 1)^2 + \frac{\mu_3}{2\alpha}(I_6)^\alpha + \frac{\mu_3}{2\beta}(I_7)^\beta + \frac{1}{2}\left(\frac{1}{2\alpha}\mu_3 + \frac{1}{2\beta}\mu_3\right) + \frac{1}{2\epsilon}\frac{I_5}{I_3}, \end{aligned} \tag{E.4}$$

where the material parameters are given in Table E.3.

Table E.3
Material parameters used with the transversely isotropic model.

Parameter:	μ_1	μ_2	μ_3	λ	α	β	$\boldsymbol{N}$	ϵ
Value:	0.5	0.5	7.5	5	2	2	$\left[1/\sqrt{3} \quad 1/\sqrt{3} \quad 1/\sqrt{3}\right]^T$	1

E.4. *Rank-one laminate ideal dielectric*

The definition for the Rank-one Laminate Ideal Dielectric strain energy density is given by

$$\begin{aligned} U^a(I_1^a, I_2^a, I_3^a, I_5^a) = {} & \frac{1}{2}\mu_1^a(I_1^a - 3) + \frac{1}{2}\mu_2^a(I_2^a - 3) - (\mu_1^a + 2\mu_2^a)\ln(I_3^a) \\ & + \frac{1}{2}\lambda^a(I_3^a - 1)^2 + \frac{1}{2\epsilon^a}\frac{I_5^a}{I_3^a}, \end{aligned} \tag{E.5}$$

$$\begin{aligned} U^b(I_1^b, I_2^b, I_3^b, I_5^b) = {} & \frac{1}{2}\mu_1^b(I_1^b - 3) + \frac{1}{2}\mu_2^b(I_2^b - 3) - (\mu_1^b + 2\mu_2^b)\ln(I_3^b) \\ & + \frac{1}{2}\lambda^b(I_3^b - 1)^2 + \frac{1}{2\epsilon^b}\frac{I_5^b}{I_3^b}. \end{aligned} \tag{E.6}$$

where the material parameters for the three variations given in Table E.4.

Table E.4
Material parameters used with the rank one laminate model.

Parameter:	μ_1^a	μ_2^a	λ^a	ϵ^a	α	β	f_m	f_e	c
Value (ROL(a)):	0.5	0.5	5	1	$\pi/4$	$\pi/4$	2	2	0.6
Value (ROL(b)):	0.5	0.5	5	1	$\pi/4$	$\pi/4$	5	3	0.6
Value (ROL(c)):	0.5	0.5	5	1	$\pi/4$	$\pi/4$	10	5	0.6

Note that the mechanical contrast f_m denotes the ratio between μ_1, μ_2 λ, and the electric contrast, the ratio between ϵ

$$f_m = \frac{\mu_1^b}{\mu_1^a} = \frac{\mu_2^b}{\mu_2^a} = \frac{\lambda^b}{\lambda^a}, \qquad f_e = \frac{\epsilon^b}{\epsilon^a}. \tag{E.7}$$

Furthermore, c represents the volume fraction where $c_a = c$ and $c_b = 1 - c$, whilst $\boldsymbol{N}$ denotes the direction of lamination characterised via the two angles α and β such that $\boldsymbol{N} = [\sin\beta\cos\alpha, \sin\beta\sin\alpha, \cos\beta]^T$.

E.5. Relative volume element details

The RVE consists of a unit cell ($1 \times 1 \times 1$) cube design which is divided into two subdomains one associated with the matrix $\boldsymbol{X}_\mu \in \mathcal{B}^m_{0_\mu}$ and the other, associated with the inclusion $\boldsymbol{X}_\mu \in \mathcal{B}^i_{0_\mu}$, such that $\mathcal{B}_{0_\mu} = \mathcal{B}^m_{0_\mu} \cup \mathcal{B}^i_{0_\mu}$, and $\mathcal{B}^m_{0_\mu} \cap \mathcal{B}^i_{0_\mu} = \emptyset$. Within each subdomain, the internal energy density is defined by $U_\mu(\boldsymbol{X}_\mu, I_{1_\mu}, I_{2_\mu}, I_{3_\mu}, I_{5_\mu}) = \Psi_\mu(\boldsymbol{X}_\mu, \boldsymbol{F}_\mu, \boldsymbol{E}_{0\mu})$ according to

$$\Psi_\mu(\boldsymbol{X}_\mu, \boldsymbol{F}_\mu, \boldsymbol{E}_{0\mu}) = U_\mu(\boldsymbol{X}_\mu, I_{1_\mu}, I_{2_\mu}, I_{3_\mu}, I_{5_\mu}) = \begin{cases} U^m_\mu(I_{1_\mu}, I_{2_\mu}, I_{3_\mu}, I_{5_\mu}) & \boldsymbol{X}_\mu \in \mathcal{B}^m_{0_\mu} \\ U^i_\mu(I_{1_\mu}, I_{2_\mu}, I_{3_\mu}, I_{5_\mu}) & \boldsymbol{X}_\mu \in \mathcal{B}^i_{0_\mu} \end{cases} \tag{E.8}$$

Note that in all cases, RVE(a-d), the free energy density functions are of the Mooney-Rivlin type, as described in Appendix E.2 but using the material parameters given in Table E.5.

Table E.5
Material parameters used for the RVE.

Parameter:	μ_1^m	μ_2^m	λ^m	ϵ^m	f_m	f_e	r_x	r_y	r_z	α	β
Value (RVE(a)):	1	1	10	1	5	5	0.25	0.25	0.25	–	–
Value (RVE(b)):	1	1	10	1	5	5	0.1	0.4	0.2	$\pi/3$	$\pi/4$
Value (RVE(c)):	1	1	10	1	5	5	0.25	0.25	0.25	–	–
Value (RVE(d)):	1	1	10	1	5	5	0.25	0.25	–	–	–

The configurations for each case above is as follows: RVE(a) has a spherical inclusion, RVE(b) has an ellipsoidal inclusion, RVE(c) is a body centred cubic, and RVE(d) is a face centred fibre. The corresponding geometries are clearly depicted in Fig. 12. Note that the mechanical contrast f_m denotes the ratio between μ_1, μ_2, λ, and the electric contrast, the ratio between ϵ as

$$f_m = \frac{\mu_1^i}{\mu_1^m} = \frac{\mu_2^i}{\mu_2^m} = \frac{\lambda^i}{\lambda^m}, \qquad f_e = \frac{\epsilon^i}{\epsilon^m}. \tag{E.9}$$

Furthermore, α and β are angles which determine the amount rotation in the xz and xy planes respectively.

Appendix F. Obtaining the reduced log likelihood

Recall the opposite log-likelihood function (47) and the optimal model parameters (48) as found via the Maximum Likelihood Estimation technique

$$\begin{aligned} \mathscr{L}\left(\boldsymbol{U}|\beta, \sigma^2, \boldsymbol{\theta}\right) &= \frac{A}{2}\log(2\pi) + \frac{A}{2}\log\left(\sigma^2\right) + \frac{1}{2}\log(|\boldsymbol{R}(\boldsymbol{\theta})|) + \frac{1}{2\sigma^2}(\boldsymbol{U} - \boldsymbol{1}\beta)^T \boldsymbol{R}^{-1}(\boldsymbol{\theta})(\boldsymbol{U} - \boldsymbol{1}\beta), \\ \beta^*(\boldsymbol{\theta}) &= \left(\boldsymbol{1}^T \boldsymbol{R}^{-1}(\boldsymbol{\theta})\boldsymbol{1}\right)^{-1} \boldsymbol{1}^T \boldsymbol{R}^{-1}(\boldsymbol{\theta})\boldsymbol{U}, \\ \sigma^{2*}(\boldsymbol{\theta}) &= \frac{1}{A}\left(\boldsymbol{U} - \boldsymbol{1}\beta^*(\boldsymbol{\theta})\right)^T \boldsymbol{R}^{-1}(\boldsymbol{\theta})\left(\boldsymbol{U} - \boldsymbol{1}\beta^*(\boldsymbol{\theta})\right). \end{aligned} \tag{F.1}$$

By substituting the optimal parameters (48) into the opposite log-likelihood function (47) one can obtain

$$\begin{aligned} \bar{\mathscr{L}}\left(\boldsymbol{U}|\beta^*, \sigma^{2*}, \boldsymbol{\theta}\right) = &\frac{A}{2}\log(2\pi) + \frac{A}{2}\log\left(\sigma^{2*}\right) + \frac{1}{2}\log(|\boldsymbol{R}(\boldsymbol{\theta})|) \\ &+ \frac{1}{2\sigma^{2*}}\left(\boldsymbol{U} - \boldsymbol{1}\beta^*\right)^T \boldsymbol{R}^{-1}(\boldsymbol{\theta})\left(\boldsymbol{U} - \boldsymbol{1}\beta^*\right). \end{aligned} \tag{F.2}$$

which can be re-expressed as

$$\bar{\mathscr{L}}\left(\boldsymbol{U}|\beta^*, \sigma^{2*}, \boldsymbol{\theta}\right) = \frac{A}{2}\log(2\pi) + \frac{A}{2}\log\left(\sigma^{2*}\right) + \frac{1}{2}\log(|\boldsymbol{R}(\boldsymbol{\theta})|) + \frac{A\sigma^{2*}}{2\sigma^{2*}}, \tag{F.3}$$

which leads to a simple factorisation

$$\bar{\mathscr{L}}\left(\boldsymbol{U}|\beta^*, \sigma^{2*}, \boldsymbol{\theta}\right) = \frac{A}{2}(\log(2\pi) + 1) + \frac{A}{2}\log\left(\sigma^{2*}\right) + \frac{1}{2}\log(|\boldsymbol{R}(\boldsymbol{\theta})|). \tag{F.4}$$

Here the constant term will now be neglected since it will not have an impact on the minimisation, and the term of interest can also be factorised as follows

$$\bar{\mathscr{L}}\left(\boldsymbol{U}|\beta^*, \sigma^{2*}, \boldsymbol{\theta}\right) = \frac{A}{2}\left(\log\left(\sigma^{2*}\right) + \frac{1}{A}\log(|\boldsymbol{R}(\boldsymbol{\theta})|)\right). \tag{F.5}$$

Finally, the rules of logs can be applied to first raise the pre-multiplied fraction to the power of the determinant term and then join the two terms

$$\bar{\mathscr{L}}\left(\boldsymbol{U}|\beta^*, \sigma^{2*}, \boldsymbol{\theta}\right) = \frac{A}{2}(\log(\psi(\boldsymbol{\theta}))), \tag{F.6}$$

where

$$\psi(\boldsymbol{\theta}) = \sigma^{2^*}(\boldsymbol{\theta})|\boldsymbol{R}(\boldsymbol{\theta})|^{\frac{1}{A}}, \tag{F.7}$$

thus retrieving (50).

Appendix G. Finite element implementation in nonlinear electromechanics

This Appendix presents the Finite Element discretisation of the weak forms associated with the coupled differential equations governing the behaviour of EAPs, presented in (2). These weak forms correspond with the stationary conditions of the following variational principle

$$\Pi(\boldsymbol{\phi}, \varphi) = \inf_{\boldsymbol{\phi}} \sup_{\varphi} \left\{ \int_{\mathcal{B}_0} \Psi(\boldsymbol{F}, \boldsymbol{E}_0)\, dV - \Pi^m_{\text{ext}}(\boldsymbol{\phi}) - \Pi^e_{\text{ext}}(\varphi) \right\}, \tag{G.1}$$

where Π^m_{ext} and Π^e_{ext} represent the external energetic contributions, defined as

$$\Pi^m_{\text{ext}}(\boldsymbol{\phi}) = \int_{\mathcal{B}_0} \boldsymbol{f}_0 \cdot \boldsymbol{\phi}\, dV + \int_{\partial_t \mathcal{B}_0} \boldsymbol{t}_0 \cdot \boldsymbol{\phi}\, dA, \qquad \Pi^e_{\text{ext}}(\varphi) = -\int_{\mathcal{B}_0} \rho^e_0 \varphi\, dV - \int_{\partial_\omega \mathcal{B}_0} \omega^e_0 \varphi\, dA. \tag{G.2}$$

As standard in finite elements, the domain $\mathcal{B}_0$ described in Section 2, representing the EAP, undergoes partitioning into a finite collection of distinct and non-overlapping elements, denoted as $e \in \mathbb{E}$. This division is carried out according to

$$\mathcal{B}_0 \approx \mathcal{B}^h_0 = \bigcup_{e \in \mathbb{E}} \mathcal{B}^e_0. \tag{G.3}$$

The unknown fields $\{\boldsymbol{\phi}, \varphi\}$, along with their corresponding test functions $\{\delta\boldsymbol{\phi}, \delta\varphi\}$, are discretised utilising the functional spaces $\mathbb{V}^{\boldsymbol{\phi}^h} \times \mathbb{V}^{\varphi^h}$ and $\mathbb{V}^{\boldsymbol{\phi}^h}_0 \times \mathbb{V}^{\varphi^h}_0$, respectively. These are defined as follows

$$\begin{aligned}
\mathbb{V}^{\boldsymbol{\phi}^h} &= \left\{ \boldsymbol{\phi} \in \mathbb{V}^{\boldsymbol{\phi}}; \quad \boldsymbol{\phi}^h \Big|_{\mathcal{B}^e_0} = \sum_{a=1}^{n^{\boldsymbol{\phi}}_{\text{node}}} N^{\boldsymbol{\phi}}_a \boldsymbol{\phi}_a \right\}, \\
\mathbb{V}^{\varphi^h} &= \left\{ \varphi \in \mathbb{V}^{\varphi}; \quad \varphi^h \Big|_{\mathcal{B}^e_0} = \sum_{a=1}^{n^{\varphi}_{\text{node}}} N^{\varphi}_a \varphi_a \right\}, \\
\mathbb{V}^{\boldsymbol{\phi}^h}_0 &= \left\{ \forall \boldsymbol{\phi} \in \mathbb{V}^{\boldsymbol{\phi}^h}; \quad \boldsymbol{\phi} = \boldsymbol{0} \text{ on } \partial_{\boldsymbol{\phi}} \mathcal{B}_0 \right\}, \\
\mathbb{V}^{\varphi^h}_0 &= \left\{ \forall \varphi \in \mathbb{V}^{\varphi^h}; \quad \varphi = 0 \text{ on } \partial_{\varphi} \mathcal{B}_0 \right\}.
\end{aligned} \tag{G.4}$$

In the context of any given field $\mathcal{Y}$ from the set $\{\boldsymbol{\phi}, \varphi\}$, the quantity $n^{\mathcal{Y}}_{\text{node}}$ signifies the count of nodes within each element of the discretisation pertaining to the field $\mathcal{Y}$. Furthermore, let $N^{\mathcal{Y}}_a : \mathcal{B}^e_0 \to \mathbb{R}$ be representative of the ath shape function employed for the purpose of interpolating the field $\mathcal{Y}$. Additionally, $\mathcal{Y}_a$ denotes the value attributed to the field $\mathcal{Y}$ at the ath node of a specific finite element. By incorporating the functional spaces as defined in Eq. (G.4), it becomes feasible to express the stationary conditions of Eq. (G.1) in relation to their corresponding residual contributions arising at the elemental level, namely

$$D\Pi[\delta\boldsymbol{\phi}] = \sum_{e=1}^{N} \delta\boldsymbol{\phi}_a \cdot \boldsymbol{R}^{\boldsymbol{\phi}}_{a,e} = 0, \qquad D\Pi[\delta\varphi] = \sum_{e=1}^{N} \delta\varphi_a R^{\varphi}_{a,e} = 0, \tag{G.5}$$

where N signifies the count of elements utilised within the foundational discretisation framework. Additionally, each of the distinct residual contributions, denoted as $\boldsymbol{R}^{\boldsymbol{\phi}}_{a,e}$ and $R^{\varphi}_{a,e}$, is amenable to representation in the following manner[2]

$$\boldsymbol{R}^{\boldsymbol{\phi}}_{a,e} = \int_{\mathcal{B}^e_0} \left(\partial_{\boldsymbol{F}} \Psi\right) \boldsymbol{\nabla}_0 N^{\boldsymbol{\phi}}_a\, dV + \int_{\mathcal{B}^e_0} N^{\boldsymbol{\phi}}_a \boldsymbol{f}_0\, dV, \qquad R^{\varphi}_{a,e} = -\int_{\mathcal{B}^e_0} \left(\partial_{\boldsymbol{E}_0} \Psi\right) \cdot \boldsymbol{\nabla}_0 N^{\varphi}_a\, dV + \int_{\mathcal{B}^e_0} N^{\varphi}_a \rho^e\, dV. \tag{G.6}$$

A Newton-Raphson scheme can be used for the solution of the weak forms in (G.5), which implies the following linearisation with respect to incremental fields $\Delta\boldsymbol{\phi} \in \mathbb{V}^{\boldsymbol{\phi}}_0$ and $\Delta\varphi \in \mathbb{V}^{\varphi}_0$

$$0 = D\Pi[\delta\boldsymbol{\phi}] + D\Pi[\delta\varphi] + D^2\Pi[\delta\boldsymbol{\phi}; \Delta\boldsymbol{\phi}] + D^2\Pi[\delta\boldsymbol{\phi}; \Delta\varphi] + D^2\Pi[\delta\varphi; \Delta\boldsymbol{\phi}] + D^2\Pi[\delta\varphi; \Delta\varphi], \tag{G.7}$$

with

$$\begin{aligned}
D^2\Pi[\delta\boldsymbol{\phi}, \Delta\boldsymbol{\phi}] &= \sum_{e=1}^{N} \delta\boldsymbol{\phi}_a \cdot \boldsymbol{K}^{\boldsymbol{\phi}\boldsymbol{\phi}}_{ab,e} \Delta\boldsymbol{\phi}_b, \qquad & D^2\Pi[\delta\boldsymbol{\phi}, \Delta\varphi] &= \sum_{e=1}^{N} \delta\boldsymbol{\phi}_a \cdot \boldsymbol{K}^{\boldsymbol{\phi}\varphi}_{ab,e} \Delta\varphi_b, \\
D^2\Pi[\delta\varphi, \Delta\boldsymbol{\phi}] &= \sum_{e=1}^{N} \delta\varphi_a \cdot \boldsymbol{K}^{\varphi\boldsymbol{\phi}}_{ab,e} \Delta\boldsymbol{\phi}_b, \qquad & D^2\Pi[\delta\varphi, \Delta\varphi] &= \sum_{e=1}^{N} \delta\varphi_a K^{\varphi\varphi}_{ab,e} \Delta\varphi_b,
\end{aligned} \tag{G.8}$$

---

[2] For the sake of simplicity, the external contributions, specifically those pertaining to $\boldsymbol{t}_0$ and ω^e_0 at the boundary, have been omitted from the expression in (G.6).

where each of the stiffness contributions is expressed as

$$\begin{aligned}\left(\boldsymbol{K}^{\boldsymbol{\phi}\boldsymbol{\phi}}_{ab,e}\right)_{ij} &= \int_{\mathcal{B}_0^e} \left(\boldsymbol{\nabla}_0 N_a^{\boldsymbol{\phi}}\right)_I \left(\boldsymbol{\nabla}_0 N_b^{\boldsymbol{\phi}}\right)_J \left(\partial^2_{\boldsymbol{F}\boldsymbol{F}}\Psi\right)_{iIjJ} \, dV,\\ \left(\boldsymbol{K}^{\boldsymbol{\phi}\varphi}_{ab,e}\right)_{i} &= -\int_{\mathcal{B}_0^e} \left(\boldsymbol{\nabla}_0 N_a^{\boldsymbol{\phi}}\right)_I \left(\boldsymbol{\nabla}_0 N_b^{\varphi}\right)_J \left(\partial^2_{\boldsymbol{F}\boldsymbol{E}_0}\Psi\right)_{iIJ} \, dV,\\ K^{\varphi\varphi}_{ab,e} &= \int_{\mathcal{B}_0^e} \left(\boldsymbol{\nabla}_0 N_a^{\varphi}\right)_I \left(\partial^2_{\boldsymbol{E}_0\boldsymbol{E}_0}\Psi\right)_{IJ} \left(\boldsymbol{\nabla}_0 N_b^{\varphi}\right)_J \, dV,\\ \boldsymbol{K}^{\varphi\boldsymbol{\phi}}_{ab,e} &= \left(\boldsymbol{K}^{\varphi\boldsymbol{\phi}}_{ab,e}\right)^T.\end{aligned} \tag{G.9}$$

A Legendre transformation to take one from an internal energy density to a Helmholtz free energy density is given by

$$\Psi(\boldsymbol{F}, \boldsymbol{E}_0) = \inf_{\boldsymbol{D}_0}\{e\left(\boldsymbol{F}, \boldsymbol{D}_0\right) - \boldsymbol{D}_0 \cdot \boldsymbol{E}_0\}, \tag{G.10}$$

from where the Hessian components are related as

$$\begin{aligned}\partial^2_{\boldsymbol{E}_0\boldsymbol{E}_0}\Psi &= \left(\partial^2_{\boldsymbol{D}_0\boldsymbol{D}_0} e\right)^{-1},\\ \left(\partial^2_{\boldsymbol{F}\boldsymbol{E}_0}\Psi\right)_{iIJ} &= -\left(\partial^2_{\boldsymbol{F}\boldsymbol{D}_0} e\right)_{iIM}\left(\partial^2_{\boldsymbol{E}_0\boldsymbol{E}_0}\Psi\right)_{MJ},\\ \left(\partial^2_{\boldsymbol{F}\boldsymbol{F}}\Psi\right)_{iIjJ} &= \left(\partial^2_{\boldsymbol{F}\boldsymbol{F}} e\right)_{iIjJ} - \left(\partial^2_{\boldsymbol{F}\boldsymbol{D}_0} e\right)_{iIM}\left(\partial^2_{\boldsymbol{E}_0\boldsymbol{F}}\Psi\right)_{MjJ}.\end{aligned} \tag{G.11}$$

Finally, standard global assembly of the residual and stiffness contributions in (G.6) and (G.9), respectively, permits to obtain the discrete form of Eq. (G.7) in terms of the nodal incremental vector fields $\{\widetilde{\boldsymbol{\Delta\phi}}, \widetilde{\boldsymbol{\Delta\varphi}}\}$

$$\begin{bmatrix}\boldsymbol{K}^{\boldsymbol{\phi}\boldsymbol{\phi}} & \boldsymbol{K}^{\boldsymbol{\phi}\varphi}\\ \boldsymbol{K}^{\varphi\boldsymbol{\phi}} & \boldsymbol{K}^{\varphi\varphi}\end{bmatrix}\begin{bmatrix}\widetilde{\boldsymbol{\Delta\phi}}\\ \widetilde{\boldsymbol{\Delta\varphi}}\end{bmatrix} = -\begin{bmatrix}\boldsymbol{R}^{\boldsymbol{\phi}}\\ \boldsymbol{R}^{\varphi}\end{bmatrix}. \tag{G.12}$$

Solution of $\{\widetilde{\boldsymbol{\Delta\phi}}, \widetilde{\boldsymbol{\Delta\varphi}}\}$ permits the update of the nodal solution fields $\{\widetilde{\boldsymbol{\Delta\phi}}, \widetilde{\boldsymbol{\Delta\varphi}}\}$ at every node of the underlying Finite Element discretisation at a given Newton-Raphson iteration $k+1$ as

$$\widetilde{\boldsymbol{\phi}}^{k+1} = \widetilde{\boldsymbol{\phi}}^{k} + \widetilde{\boldsymbol{\Delta\phi}}, \qquad \widetilde{\boldsymbol{\varphi}}^{k+1} = \widetilde{\boldsymbol{\varphi}}^{k} + \widetilde{\boldsymbol{\Delta\varphi}}. \tag{G.13}$$

References

[1] Y. Guo, L. Liu, Y. Liu, J. Leng, Review of dielectric elastomer actuators and their applications in soft robots, Adv. Intell. Syst. 3 (2021) 1–18.

[2] K. Jung, K.J. Kim, H.R. Choi, A self-sensing dielectric elastomer actuator, Sens. Actuators A Phys. 143 (2008) 343–351.

[3] E. Hajiesmaili, D.R. Clarke, Dielectric elastomer actuators, J. Appl. Phys. 129 (2021) 151102.

[4] K. Bertoldi, M. Gei, Instabilities in multilayered soft dielectrics, JMPS 59 (2011) 18–42.

[5] M. Gei, R. Springhetti, E. Bortot, Performance of soft dielectric laminated composites, Smart Mater. Struct. 22 (2013) 1–8.

[6] L. Tian, L. Tevet-Deree, G. deBotton, K. Bhattacharya, Dielectric elastomer composites, JMPS 60 (2012) 181–198.

[7] G. deBotton, L. Tevet-Deree, E.A. Socolsky, Electroactive heterogeneous polymers: analysis and applications to laminated composites, Mech. Adv. Mater. Struct. 14 (2007) 13–22.

[8] F. Marín, J. Martínez-Frutos, R. Ortigosa, A.J. Gil, A convex multi-variable based computational framework for multilayered electro-active polymers, CMAME 374 (2021) 1–42.

[9] F. Marín, R. Ortigosa, J. Martínez-Frutos, A.J. Gil, Viscoelastic up-scaling rank-one effects in in-silico modelling of electro-active polymers, CMAME 389 (2022) 1–44.

[10] K. Linka, E. Kuhl, A new family of constitutive artificial neural networks towards automated model discovery, CMAME 403 (2023) 1–27.

[11] K. Linka, M. Hillgärtner, K.P. Abdolazizi, R.C. Aydin, M. Itskov, C.J. Cryon, Constitutive artificial neural networks: a fast and general approach to predictive data-driven constitutive modeling by deep learning, J. Comput. Phys. 429 (2021) 1–17.

[12] R. Ortigosa, A.J. Gil, A new framework for large strain electromechanics based on convex multi-variable strain energies: conservation laws, hyperbolicity and extension to electro-magneto-mechanics, CMAME 309 (2016) 202–242.

[13] R. Ortigosa, A.J. Gil, A new framework for large strain electromechanics based on convex multi-variable strain energies: finite element discretisation and computational implementation, CMAME 302 (2016) 329–360.

[14] A.J. Gil, R. Ortigosa, A new framework for large strain electromechanics based on convex multi-variable strain energies: variational fomulation and material characterisation, CMAME 302 (2016) 293–328.

[15] R. Ortigosa, A.J. Gil, J. Bonet, C. Hesch, A computational framework for polyconvex large strain elasticity for geometrically exact beam theory, Comput. Mech. 57 (2016) 277–303.

[16] D.K. Klein, M. Fernández, R.J. Martin, P. Neff, O. Weeger, Polyconvex anisotropic hyperelasticity with neural networks, JMPS 159 (2022) 1–25.

[17] D.K. Klein, R. Ortigosa, J. Martínez-Frutos, O. Weeger, Finite electro-elasticity with physics-augmented neural networks, CMAME 400 (2022) 115501.

[18] D.K. Klein, R. Ortigosa, J. Martínez-Frutos, O. Weeger, Nonlinear electro-elastic finite element analysis with neural network constitutive models, CMAME 425 (2024) 116910.

[19] R. Ortigosa, J. Martínez-Frutos, A. Pérez-Escolar, I. Castañar, N. Ellmer, A.J. Gil, A generalized theory for physics-augmented neural networks in finite strain thermo-electro-mechanics, CMAME 437 (2025) 117741.

[20] M. Flaschel, S. Kumar, L. De Lorenzis, Automated discovery of generalized standard material models with EUCLID, CMAME 405 (2023) 1–26.

[21] P. Thakolkaran, A. Joshi, Y. Zheng, M. Flaschel, L. De Lorenzis, S. Kumar, NN-EUCLID: deep-learning hyperelasticity without stress data, JMPS 169 (2022) 1–29.

[22] A. Joshi, P. Thakolkaran, Y. Zheng, M. Escande, M. Flaschel, L. De Lorenzis, S. Kumar, Bayesian-EUCLID: discovering hyperelastic material laws with uncertainties, CMAME 398 (2022) 1–37.

[23] M. Flaschel, H. Yu, N. Reiter, J. Hinrichsen, S. Budday, P. Steinmann, S. Kumar, L. De Lorenzis, Automated discovery of interpretable hyperelastic material models for human brain tissue with EUCLID, JMPS 180 (2023) 105404.

[24] H. Xu, M. Flaschel, L. De Lorenzis, Discovering non-associated pressure-senstitive plasticity models with EUCLID, Adv. Model. Simul. Eng. Sci. 12 (2025) 1–41.

[25] C.E. Rasmussen, C.K.I. Williams, Gaussian Processes for Machine Learning, MIT Press, 2006.
[26] C.M. Bishop, Pattern Recognition and Machine Learning, Springer, New York, 2006.
[27] J.I. Marden, Multivariate Statistics: Old School, CreateSpace Independent Publishing, 2015.
[28] E.B. Anderes, Kriging, Encyclopedia of Environmetrics (2013) 1–6. https://doi.org/10.1002/9780470057339.vak003.pub2.
[29] J. Ollar, C. Mortished, R. Jones, J. Sienz, V. Toropov, Gradient based hyper-parameter optimisation for well conditioned kriging metamodels, Struct. Multidiscip. Optim. 55 (2017) 2029–2044.
[30] N. Ellmer, R. Ortigosa, J. Martínez-Frutos, A.J. Gil, Gradient enhanced gaussian process regression for constitutive modelling in finite strain hyperelasticity, CMAME 418 (2024) 116547.
[31] A.L. Frankel, R.E. Jones, L.P. Swiler, Tensor basis Gaussian process models of hyperelastic materials, JMLMC 1 (2020) 1–17.
[32] A.A. B.S. Jensen, S. Pant, C.-H. Lee, Strain energy density as a Gaussian process and its utilization in stochastic finite element analysis: application to planar soft tissues, CMAME 404 (2023) 1–27.
[33] I.B.C.M. Rocha, P. Kerfriden, F.P. van der Meer, On-the-fly construction of surrogate constitutive models for concurrent multiscale mechanical analysis through probabilistic machine learning, J. Comput. Phys. X 9 (2021) 1–27.
[34] N. Ellmer, R. Ortigosa, J. Martínez-Frutos, R. Poya, J. Sienz, A.J. Gil, Stretch-based hyperelastic constitutive metamodels via gradient enhanced Gaussian predictors, CMAME 432 (2024) 117408.
[35] J.N. Fuhg, N. Bouklas, R.E. Jones, Learning hyperelastic anisotropy from data via a tensor basis neural network, JMPS 168 (2022) 105022.
[36] A.A. Jadoon, K.A. Kalina, M. Rausch, R.E. Jones, J.N. Fuhg, Inverse Design of Anisotropic Microstructures Using Physics-Augmented Neural Networks, JMPS 203 (2025) 106161.
[37] J. Bonet, A.J. Gil, R. Ortigosa, On a tensor cross product based formulation of large strain solid mechanics, Int. J. Solids Struct. 84 (2016) 49–63.
[38] M. Horák, A.J. Gil, R. Ortigosa, M. Kružík, A polyconvex transversely-isotropic invariant-based formulation for electro-mechanics: stability, minimisers and computational implementation, CMAME 403 (2023) 115695.
[39] R. Poya, R. Ortigosa, A.J. Gil, Variational schemes and mixed finite elements for large strain isotropic elasticity in principal stretches: Closed-form tangent eigensystems, convexity conditions, and stabilised elasticity, IJNME 124 (2023) 3436–3493.
[40] R. Poya, R. Ortigosa, A.J. Gil, J. Bonet, Generalised tangent stabilised nonlinear elasticity: an automated framework for controlling material and geometric instabilities, CMAME 436 (2025) 117701.
[41] A.J. Gil, R. Ortigosa, A new framework for large strain electromechanics based on convex multi-variable strain energies: variational formulation and material characterisation, CMAME 302 (2016) 293–328.
[42] J. Schroder, Anisotropic Polyconvex Energies, Springer, 2010, pp. 53–105.
[43] B. Smith, F. De Goes, T. Kim, Analytical eigensystems for isotropic distortion energies, ACM Trans. Graphics 38 (2019) 1–15.
[44] Q.S. Zheng, Theory of representations for tensor functions–a unified invariant approach to constitutive equations, ASME 47 (1994) 545–587.
[45] G. deBotton, Transversely isotropic sequentially laminated composites in finite elasticity, JMPS 53 (2005) 1334–1361.
[46] M. Gei, K. Mutasa, Optimisation of hierarchical dielectric elastomer laminated composites, Int. J. Non-Linear Mech. 106 (2018) 266–273.
[47] K.A. Kalina, J. Brummund, W.C. Sun, M. Kästner, Neural networks meet anisotropic hyperelasticity: a framework based on generalized structure tensors and isotropic tensor functions, CMAME 437 (2025) 117725.
[48] M.A. Wolfe, An interval algorithm for bound constrained global optimization, Optim. Methods Softw. 6 (1995) 145–159.
[49] J. Nocedal, S.J. Wright, Numerical Optimization, Springer, New York, 1999.
[50] D.E. Goldberg, Genetic Algoirthms in Search, Optimisation & Machine Learning, Addison-Wesley Professional, 1989.
[51] MathWorks MATLAB Optimization Toolbox 2024, (https://uk.mathworks.com/help/optim/ug/fmincon.html). Accessed: 24/06/2024.
[52] O. Kunc, F. Fritzen, Finite strain homogenization using a reduced basis and efficient sampling, Math. Comput. Appl. 24 (2019) 1–28.
[53] A. Pérez-Escolar, J. Martínez-Frutos, R. Ortigosa, N. Ellmer, A.J. Gil, Learning nonlinear constitutive models in finite strain electromechanics with Gaussian process predictors, Comput. Mech. 74 (2024) 1–23.
[54] J. Martínez-Frutos, D. Herrero-Pérez, Kriging-based infill sampling criterion for constraint handling in multi-objective optimization, J. Global Optim. 64 (2016) 97–115.
[55] A. Forrester, A. Sóbester, A. Keane, Engineering Design via Surrogate Modelling: A Practical Guide, Wiley, Chichester, 2008.